Copyright © 2004, by the author(s).
All rights reserved.

Permission to make digital or hard copies of all or part of this work for personal or classroom use is granted without fee provided that copies are not made or distributed for profit or commercial advantage and that copies bear this notice and the full citation on the first page. To copy otherwise, to republish, to post on servers or to redistribute to lists, requires prior specific permission.

CHARACTERIZATION OF THE CRITICAL DIMENSION ERROR BUDGET FOR EXTREME ULTRAVIOLET LITHOGRAPHY

by

Jason Phillip Cain

Memorandum No. UCB/ERL M04/50

20 December 2004

cover

CHARACTERIZATION OF THE CRITICAL DIMENSION ERROR BUDGET FOR EXTREME ULTRAVIOLET LITHOGRAPHY

by

Jason Phillip Cain

Memorandum No. UCB/ERL M04/50

20 December 2004

ELECTRONICS RESEARCH LABORATORY

College of Engineering
University of California, Berkeley
94720

Characterization of the Critical Dimension Error Budget for Extreme Ultraviolet Lithography

by

Jason Phillip Cain

B.S. (Texas A&M University) 1999
M.S. (University of California, Berkeley) 2002

A dissertation submitted in partial satisfaction of the
requirements for the degree of
Doctor of Philosophy

in

Engineering – Electrical Engineering and Computer Sciences

in the

GRADUATE DIVISION
of the
UNIVERSITY OF CALIFORNIA, BERKELEY

Committee in charge:
Professor Costas J. Spanos, Chair
Professor Andrew R. Neureuther
Professsor David T. Attwood
Professor Kameshwar Poolla

Fall 2004

The dissertation of Jason Phillip Cain is approved:

Chair Date

Date

Date

Date

University of California, Berkeley

Fall 2004

Characterization of the Critical Dimension Error Budget for Extreme Ultraviolet Lithography

Copyright 2004

by

Jason Phillip Cain

Abstract

Characterization of the Critical Dimension Error Budget for Extreme Ultraviolet Lithography

by

Jason Phillip Cain

Doctor of Philosophy in Engineering – Electrical Engineering and Computer Sciences

University of California, Berkeley

Professor Costas J. Spanos, Chair

With conventional optical lithography nearing its physical limits, the search is underway to find a suitable successor. One such candidate is lithography at extreme ultraviolet (EUV) wavelengths. This dissertation explores some of the key issues related to critical dimension (CD) control in the context of EUV lithography. A framework for photoresist-based characterization of the projection optics in an EUV lithography tool, including aberrations and flare, is described. An adaptation of the well-known Kirk method for measuring flare is applied to EUV lithography, and flare is found to be slightly larger (values on the order of 8-13%) than predicted from optical surface roughness measurements. Reasons for this discrepancy are explored. Through the use of simple test patterns, scanning electron microscopy for analysis, and lithography modeling software, astigmatism is

measured and found to be on the order of 0.5 nm RMS in magnitude. The contrast transfer function (CTF) is used as a measure of overall optical performance, and is measured using a variety of resists and for both darkfield and brightfield cases.

There are many challenges in developing an EUV resist which meets the requirements for resolution, line edge roughness, and sensitivity. Here a procedure for characterizing the sensitivity of photoresists to post-exposure bake temperature (both steady-state and transient) is outlined. In addition, the fundamental resolution of EUV photoresists is studied using a resist point-spread function model. Good agreement is found with results for resists studied previously, and new resists are found to offer significantly better resolution.

Accurate and precise metrology capability is essential for achieving good process control. In this work the use of various forms of optical scatterometry for critical dimension metrology is investigated through a simulation sensitivity study. Spectroscopic ellipsometry shows the potential to meet the CD metrology needs down to the 22 nm node, and reflectometry-based methods may find applications down to the 32 nm node.

Finally, the results of these experiments are brought together in an error budget analysis for this particular EUV lithography process. The challenges of such an analysis are addressed, and key areas for future improvement are discussed.

Professor Costas J. Spanos
Dissertation Committee Chair

For Melissa,

who has tolerated many late nights and lost weekends,

and still loves me anyway.

I could not have done this without her.

Contents

List of Figures v

List of Tables viii

1 Introduction 1
1.1 Motivation . . . 1
1.2 Thesis Layout . . . 3

2 Background 5
2.1 Introduction to Photolithography . . . 5
2.1.1 Principles . . . 5
2.1.2 Process Flow . . . 6
2.1.3 Resolution and Critical Dimension Control . . . 6
2.1.4 Lithography Equipment . . . 10
2.2 Extreme Ultraviolet Lithography . . . 12
2.2.1 Motivation for EUV Lithography . . . 12
2.2.2 EUV Lithography Technology . . . 13
2.3 Experimental Setup . . . 18
2.3.1 The Micro-Exposure Tool (MET) . . . 19
2.3.2 Photoresist Processing Equipment . . . 21
2.4 CD Error Budget Analysis . . . 21
2.4.1 International Technology Roadmap for Semiconductors . . . 21
2.4.2 Error Budget Methodology . . . 22

3 Characterization of Projection Optics in EUV Lithography Tools 24
3.1 Aberrations and Flare . . . 24
3.1.1 Aberrations . . . 25
3.1.2 Flare . . . 31
3.1.3 Interferometric Measurements of the MET Wavefront . . . 34
3.2 Resist-Based Measurement of Flare . . . 34
3.3 Measurement of Aerial Image Contrast . . . 43
3.3.1 Simulation of Contrast Transfer Function for the MET Optic . . . 45

3.3.2 Darkfield Contrast Transfer Function . . . 46
3.3.3 Brightfield Contrast Transfer Function . . . 49
3.3.4 Orientation Dependence of Contrast Transfer Function . . . 54
3.4 Resist-Based Measurement of Optical Aberrations . . . 56
3.4.1 Focal Plane Tilt . . . 56
3.4.2 Astigmatism . . . 58
3.4.3 Spherical Aberration . . . 64
3.4.4 Coma . . . 65
3.5 Interferometric Method of Aberrometry for Obscurated Optical Systems . . 65
3.5.1 Method . . . 66
3.5.2 Practical Implementation Considerations . . . 68

4 Characterization of EUV Photoresists **71**
4.1 Resist Overview . . . 71
4.1.1 Types of Photoresists . . . 72
4.1.2 Photoresist Process Flow . . . 72
4.2 CD Sensitivity to Post Exposure Bake Temperature Variations . . . 73
4.2.1 Steady-State Temperature Variation . . . 74
4.2.2 Transient Temperature Variation . . . 79
4.3 CD Sensitivity to PEB Time Variation . . . 82
4.4 Resist Modeling with Resist Point Spread Function . . . 83
4.4.1 Extraction of Resist Point Spread Function . . . 84
4.4.2 Gaussian Resist Point Spread Function . . . 86
4.4.3 Interpretation of DC Offset Term . . . 87

5 Optical Metrology for Future Technology Nodes **89**
5.1 Background . . . 90
5.1.1 Scatterometry Equipment . . . 90
5.1.2 Solving the Inverse Problem . . . 92
5.2 Scatterometry Sensitivity Study for Future Technology Nodes . . . 99
5.2.1 The 65 nm Node . . . 100
5.2.2 The 45 nm Node . . . 107
5.2.3 The 32 nm Node . . . 114
5.2.4 The 22 nm Node . . . 121
5.3 Conclusions . . . 131

6 CD Error Budget Analysis for EUV Lithography **132**
6.1 CD Sensitivity of Key Error Budget Components . . . 132
6.2 Interaction Effects on Process Window . . . 134
6.3 Critical Issues for the Future of EUV Lithography . . . 139

7 Conclusions **142**
7.1 Summary . . . 142
7.2 Future Work . . . 143

References 146

A Tcl Source Code for Grating Simulation with *gtk* 159

B List of Symbols 165

List of Figures

2.1 Photolithography process flow 7
2.2 Schematic diagram of a projection lithography system. 10
2.3 Operation of a multilayer interference coating. 15
2.4 Reflectivity of a Si/Mo multilayer. 16
2.5 Schematic of multilayer reflective mask. 17
2.6 Schematic diagram of Micro-Exposure Tool (MET) 20

3.1 Some important Zernike circle polynomials. 28
3.2 Some important Zernike annular polynomials ($\epsilon = 0.3$). 32
3.3 MET wavefront measured using PS/PDI 35
3.4 Field layout used for flare measurement. 36
3.5 Cross patterns used for flare measurement. 36
3.6 SEM image of cross patterns just before cross-linking 37
3.7 SEM image of cross patterns just after cross-linking 38
3.8 Behavior of resist through dose in flare experiments 39
3.9 Contour map of flare for 500 nm features 40
3.10 Contour map of flare for 1 μm features 41
3.11 Contour map of flare for 2 μm features 42
3.12 Illustration of aerial image contrast 44
3.13 Principle of contrast measurement in resist 45
3.14 Resist images showing contrast measurement technique 46
3.15 Simulated contrast transfer function for the MET 47
3.16 Mask pattern for darkfield contrast transfer function measurements. 48
3.17 Cell view of mask pattern for darkfield contrast transfer function measurements. 48
3.18 Measured darkfield CTF for the MET 49
3.19 Behavior of D_{max} and D_{min} for EUV-2D 50
3.20 Behavior of D_{max} and D_{min} for MET-1K 51
3.21 Behavior of D_{max} and D_{min} for KRS 52
3.22 Comparison of brightfield and darkfield CTF. 53
3.23 Behavior of D_{max} and D_{min} for MET-1K (brightfield) 54
3.24 Orientation dependence of CTF. 55
3.25 Line edge roughness through focus across the field 57

3.26 Contour map of best focus across the field 58
3.27 50 nm elbow patterns used for measuring astigmatism 59
3.28 Extraction of astigmatism for the MET 60
3.29 Contour map of 0° astigmatism in the MET optic 61
3.30 Extraction of 45° astigmatism for the MET 62
3.31 Contour map of 45° astigmatism in the MET optic 63
3.32 Contour map of total astigmatism in the MET optic 63
3.33 Two-wave interference with OPD 66
3.34 Illustration of frequency doubling with central obscuration 67

4.1 Sample PEB temperature trajectory 75
4.2 PEB temperature uniformity for 130° wafer 76
4.3 PEB temperature uniformity for 128° wafer 76
4.4 PEB temperature uniformity for 132° wafer 77
4.5 PEB temperature trajectories for steady-state experiment 78
4.6 PEB steady-state CD sensitivity for 100 nm features 79
4.7 PEB steady-state CD sensitivity for 60 nm features 80
4.8 Temperature trajectories with and without Kapton film 81
4.9 CD sensitivity to PEB temperature ramp time 82
4.10 Resist point spread function with DC offset for EUV-2D 86
4.11 Resist point spread function with DC offset for MET-1K 87
4.12 Resist point spread function with DC offset for KRS 88

5.1 Scatterometry tool configurations 91
5.2 Layers within a grating structure 94
5.3 Horizontal layers approximating arbitrary grating profile 94
5.4 Grating profile examples 96
5.5 Optical properties of Rohm and Haas MET-1K resist 98
5.6 Reflectometer response for 65 nm node dense features 101
5.7 Polarization-sensitive reflectometer response for 65 nm node dense features 102
5.8 Spectroscopic ellipsometry response for 65 nm node dense features 103
5.9 Reflectometer response for 65 nm node isolated features 104
5.10 Polarization-sensitive reflectometer response for 65 nm node isolated features 105
5.11 Spectroscopic ellipsometry response for 65 nm node isolated features 106
5.12 Reflectometer response for 45 nm node dense features 108
5.13 Polarization-sensitive reflectometer response for 45 nm node dense features 109
5.14 Spectroscopic ellipsometry response for 45 nm node dense features 110
5.15 Reflectometer response for 45 nm node isolated features 111
5.16 Polarization-sensitive reflectometer response for 45 nm node isolated features 112
5.17 Spectroscopic ellipsometry response for 45 nm node isolated features 113
5.18 Reflectometer response for 32 nm node dense features 115
5.19 Polarization-sensitive reflectometer response for 32 nm node dense features 116
5.20 Spectroscopic ellipsometry response for 32 nm node dense features 117
5.21 Reflectometer response for 32 nm node isolated features 118
5.22 Polarization-sensitive reflectometer response for 32 nm node isolated features 119

5.23 Spectroscopic ellipsometry response for 32 nm node isolated features 120
5.24 Reflectometer response for 22 nm node dense features 122
5.25 Polarization-sensitive reflectometer response for 22 nm node dense features 123
5.26 Spectroscopic ellipsometry response for 22 nm node dense features 124
5.27 Reflectometer response for 22 nm node isolated features 125
5.28 Polarization-sensitive reflectometer response for 22 nm node isolated features 126
5.29 Spectroscopic ellipsometry response for 22 nm node isolated features 127
5.30 Change in tan(Ψ) for 0.2 nm change in CD 129
5.31 Change in cos(Δ) for 0.2 nm change in CD 130

6.1 Scaled wavefront data used for aerial image simulations. 136
6.2 Effect of aberrations on process window. 137
6.3 Process window restricted to variation from lithography only. 138
6.4 Process window restricted to variation from exposure only. 139

List of Tables

2.1 ITRS predictions for the 32-nm technology node 22

3.1 The first 37 Zernike circle polynomials. 29
3.2 Darkfield contrast data for EUV-2D resist. 50
3.3 Darkfield contrast data for MET-1K resist. 51
3.4 Darkfield contrast data for KRS resist. 52
3.5 Brightfield contrast data for MET-1K resist. 53
3.6 Extracted 0° astigmatism by field location. 61
3.7 Extracted 45° astigmatism by field location. 61
3.8 Extracted total astigmatism by field location. 61
3.9 Expected pattern shifts for the base MET wavefront. 68

4.1 Effect of PEB temperature ramp time on CD. 81
4.2 Effect of PEB time on CD. 83

5.1 Grating parameters and metrology requirements for the 65 nm node 100
5.2 Grating parameters and metrology requirements for the 45 nm node 107
5.3 Grating parameters and metrology requirements for the 32 nm node 114
5.4 Grating parameters and metrology requirements for the 22 nm node 121

6.1 Random CD error budget components for the MET system 134
6.2 Random CD error budget components for production-level EUV tool 134

Acknowledgments

First and foremost, I would like to thank my advisor, Professor Costas Spanos. His expertise, guidance, friendship, and encouragement were greatly appreciated, and his financial support made my studies at Berkeley possible. I will always be grateful for the knowledge of the semiconductor industry which he shared with me and for the academic and career development opportunities he created for me. Also, I would like to thank Professor Andrew Neureuther for imparting a small fraction of his tremendous knowledge of the science of lithography, and for serving as the chair of my qualifying exam committee. His enthusiasm and creativity are inspiring. Professor David Attwood was instrumental in getting me involved in EUV lithography research at Lawrence Berkeley National Lab, first though his excellent class on soft X-rays and EUV radiation and later through personal assistance in connecting me with the EUVL team. Thanks also to Professor Kameshwar Poolla for serving as a member of both my qualifying exam and dissertation committees.

I owe a huge debt of gratitude to Patrick Naulleau of the Center for X-Ray Optics at LBNL. His mentorship during the course of my experiments there (not to mention his willingness to work late on Friday nights!) greatly improved the quality of my work, and I certainly could not have done it without his assistance. I would also like to thank many of the other members of the excellent technical staff at CXRO, including Ken Goldberg, Paul Denham, Brian Hoef, Erik Anderson, Eric Gullikson, Alex Liddle, Farhad Salmassi, and Keith Jackson. Thanks are also due to Kim Dean of International Sematech for her support of my research on the MET system and Robert Brainard of Rohm and Haas for his help with EUV photoresists.

I would like to thank all of the past and present members of the Berkeley Computer-Aided Manufacturing (BCAM) group: Junwei Bao, Runzi (Tiger) Chang, Anna Ison, Michiel Krüger, Nickhil Jakatdar, Payman Jula, Jae-Wook Lee, Weng-Loong (Ralph) Foong, Mason Freed, Paul Friedberg, Jing Xue, Jiangxin Wang, Haolin Zhang, Qiaolin (Charlie) Zhang, and Dongwu Zhao. Not only did they provide great friendships, but I learned a lot from each of them, and it was a pleasure to work together. Thanks also to my other friends in Cory Hall: Kostas Adam, Frank Gennari, Scott Hafeman, Michael Lam, Greg McIntyre, Wojtek Poppe, Garth Robins, Yashesh Shroff, Michael Shumway, Michael Williamson, and Lei Yuan. They made grad school much more fun.

I was very lucky to have the support of an excellent administrative staff, including Ruth Gjerde in the EE Graduate Office and Charlotte Jones and Diane Chang in the Electronics Research Laboratory. They handled virtually all of the details of the UC bureaucracy, leaving me free to focus on my research, and they always did so with a smile.

Thanks to the staff of the UC Berkeley Microfabrication Laboratory, including Katalin Voros, Bob Hamilton, and Evan Stateler. Thanks also to T.K. Chen for his support in all manner of computing issues.

I offer my deepest thanks to all of the Cain and Mendoza families back in Texas. Their love and support has meant the world to me. Also thanks to the Mendoza family in Vallejo, CA for treating me like a member of the family, and providing many free meals!

I have no words to express my gratitude to my wife, Melissa, for everything she has done for me during my grad school career. Not only did she agree to move half way across the country to allow me to pursue my interests, but she has supported me in every

way possible. Without her love and encouragement, I would not have made it. I very much look forward to spending more time with her now that this is done.

This work was funded by Advanced Micro Devices, Applied Materials, Atmel, Cadence, Canon, Cymer, DuPont, Ebara, Intel, KLA-Tencor, Mentor Graphics, Nikon Research, Novellus Systems, Panoramic Technologies, Photronics, Synopsis, Tokyo Electron, and the UC Discovery Grant.

Chapter 1

Introduction

1.1 Motivation

The microelectronics industry has seen remarkable growth and progress over the past few decades. As Gordon Moore famously observed in 1965 [1], the density of transistors in a circuit tends to double every 18-24 months, a trend now known as Moore's Law. Incredibly, the semiconductor industry has maintained this pace for nearly 40 years [2]. Much of this progress in scaling transistor sizes and packing them closer together has been the result of advances in optical lithography, the method used for defining the circuit patterns on the surface of silicon wafers [3].

However, as feature sizes have reached the sub-100 nm regime, fundamental physical limits have begun to restrict the evolutionary development of optical lithography tools. It appears that a revolutionary technology is required if the industry is to continue the trend of Moore's Law. Several possible techniques, known collectively as next-generation lithography (NGL) technologies, have emerged as potential solutions. One such candidate

is extreme ultraviolet (EUV) lithography. While the basic principles of this technology are similar to conventional optical lithography, the implementation is radically different. At EUV wavelengths near 13.5 nm, material properties are quite different from those at deep ultraviolet (DUV) wavelengths where current lithography tools operate. The primary difference in material properties is that most materials are highly absorbent in the EUV portion of the electromagnetic spectrum, meaning that the use of transmission masks and optics is no longer practical. Therefore, extreme ultraviolet lithography will require the development of an entirely new infrastructure. This includes advances in optics (composed entirely of reflective elements based on multilayer reflective coatings), EUV sources, mask handling, inspection, and repair, photoresists, and a host of other areas. However, this has been an area of active research in recent years, and significant progress has been made.

Although EUV lithography technology is far from mature, it is reaching a transition point from basic science research to research and development of actual production tools. Production lithography processes require not only the resolution to print small features, but the process control to minimize variation in the feature sizes. Due to the clocked nature of most digital integrated circuits, a chip is in a sense only as fast as its slowest component. Therefore, minimizing process variation allows the clock speed to be increased while still maintaining correct circuit functionality.

The goal of this dissertation is to examine several of the key contributors to critical dimension (CD) variation in EUV lithography. The combined contributions of each of these sources of variation is known as the CD error budget. The idea is that performing error budget analysis at this relatively early stage of development will have two benefits. First,

it will aid in prioritizing areas for further development (namely, the largest contributors to the error budget). Second, the techniques employed here may serve as a framework for future error budget analyses of later tools as development progresses.

1.2 Thesis Layout

Chapter 2 provides a basic introduction to lithography. This includes a brief description of principles and process flow, as well as a discussion of resolution and critical dimension control. The current state-of-the-art in lithography tools is reviewed, followed by an overview of EUV lithography technology, emphasizing the differences from current DUV lithography. This also includes a description of the Micro-Exposure Tool (MET), an EUV lithography tool used for all experimental work presented in this dissertation. Finally, the requirements for future manufacturing needs related to lithography and CD metrology are discussed, and a brief introduction to error budget analysis is presented.

Chapter 3 is devoted to methods for characterizing different forms of imperfections in the projection optics of EUV lithography systems. This includes an introduction to both lens aberrations (figure errors) and flare (finish errors), as well as techniques for specifying each. Resist-based methods for measuring flare and aberrations suitable for use in a production EUV lithography tool are described, and experimental results of applying these techniques to the MET system are presented.

In Chapter 4, the characterization of extreme ultraviolet photoresists is studied. This includes a set of experiments designed to measure the sensitivity of critical dimension in EUV resists to variations in the post-exposure bake (PEB) process. This process is

critical for chemically-amplified resists, the dominant method for achieving high sensitivity (and therefore high throughput) in modern resists. The CD sensitivity to both transient and steady-state PEB temperature is studied. In addition, the fundamental resolution of EUV photoresists is determined using a resist point-spread function model.

Metrology techniques of extremely high precision and accuracy are required to meet the process control goals for technology generations where EUV lithography will be relevant. To this end, optical metrology based on scatterometry is studied as a CD metrology option in Chapter 5. A detailed simulation study of the sensitivity of several forms of scatterometry to critical dimension variation is undertaken to determine the feasibility of this metrology technique for very small features.

The results from these chapters are brought together in Chapter 6, in which an error budget analysis for the EUV lithography process used for these experiments is conducted. Difficulties and uncertainties present in such an analysis are discussed, and the interaction between error budget components is addressed.

Finally, a summary of the work is presented in Chapter 7. This includes consideration of the individual experiments performed and how they fit into the overall error budget. Finally, possible directions for future work are discussed.

Chapter 2

Background

This chapter presents a brief introduction to the field of photolithography, with emphasis on extreme ultraviolet (EUV) lithography. These sections are not intended to be exhaustive; for more a more complete description interested readers should consult one of the many external references on the subject [4, 5, 6]. Readers familiar with the field of lithography can comfortably skip these sections. In addition, the experimental setup used in all experiments discussed later in this dissertation is described. Finally, a discussion of the critical dimension error budget is presented.

2.1 Introduction to Photolithography

2.1.1 Principles

Photolithography is the process by which a pattern from a template, or mask, is transferred into a stack of thin films on the surface of a silicon wafer in order to create integrated circuits. These patterns may be transistor gates, metal interconnect lines to

connect devices, contacts or vias to connect between layers, or a variety of other features. The photolithographic patterning process is one of the most complex and difficult in the semiconductor process flow, and has therefore been the subject of intense research and development throughout the history of the semiconductor industry. However, the remarkable amount of progress made in this field has been one of the key drivers in the continuation of "Moore's Law" [3]. This section provides a basic introduction to photolithography in general.

2.1.2 Process Flow

The photolithography process is accomplished by illuminating the mask from behind and forming a demagnified image of it on the surface of the wafer. The wafer is coated with a material called photoresist that undergoes a chemical reaction when exposed to light. This chemical reaction changes the solubility of the photoresist, making the exposed areas either more soluble (positive resist) or less soluble (negative resist) than the surrounding unexposed areas. A chemical known as a developer is then used to remove the less soluble areas of the photoresist, leaving the desired pattern behind. This pattern may then be etched into the underlying film stack. After etching, the remaining photoresist may be removed, leaving the desired pattern in the film stack. This process is shown schematically in Figure 2.1.

2.1.3 Resolution and Critical Dimension Control

Many definitions of resolution in optical systems have been employed throughout history [7]. The most commonly used definition in optical lithography is based upon the

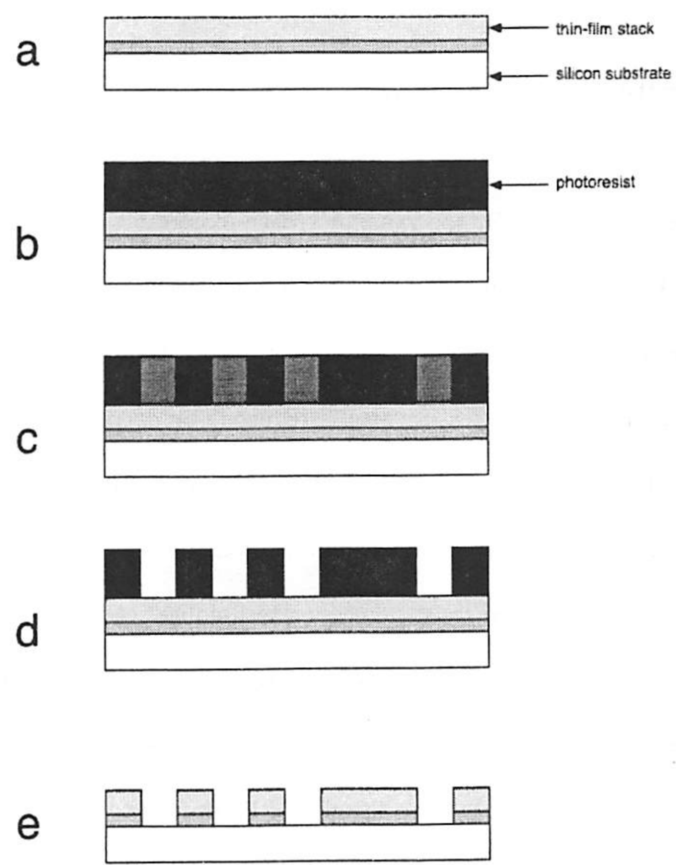

Figure 2.1: Photolithography process flow. (a) Thin film preparation, (b) photoresist coating, (c) exposure and post-exposure bake, (d) development, (e) etching and photoresist removal.

Rayleigh criterion. The minimum half-pitch L_{min} for a lithography process follows the following relationship [8]:

$$L_{min} = k_1 \frac{\lambda}{NA}, \tag{2.1}$$

where λ is the wavelength of the light source of the lithography system, NA is the numerical aperture of the projection optics, and k_1 is a procss parameter describing the "difficulty" of the process (the smaller the value of k_1, the more difficult the process).

The relationship in Eq. 2.1 has formed the basis for most strategies for increasing the resolution of optical lithography systems. That is, resolution may be increased (*i.e.*, minimum printable feature size is reduced) by decreasing the exposure wavelength, increasing the numerical aperture, or decreasing k_1 through resolution enhancement techniques (RETs) [9] such as modified illumination, phase-shifting masks, optical proximity corrections, and advanced resist-processing techniques. In 2004, the minimum feature sizes for densely-packed features are expected to reach 90 nm, with lithography systems using a source wavelength of 193 nm and having a numerical aperture of 0.85, which leads to a k_1 value of about 0.4. Although the theoretical limit of k_1 for partially coherent illumination is 0.25 [10], practical considerations make lithography with a k_1 value below about 0.35 prohibitively difficult.

Although Eq. 2.1 describes the minimum half-pitch which can be resolved in a lithography system, this is not necessarily the same as the minimum feature size (often referred to as the "critical dimension," or CD). Printed feature sizes can be reduced below half of the minimum pitch through a variety of techniques, primarily related to resist pro-

cessing (*e.g.*, resist "trimming," the process of briefly exposing developed resist lines to a plasma which attacks the resist, shrinking the linewidths before etch). The minimum feature size is determined primarily by the ability to maintain strict control over CD variation. Low variation is essential for achieving high chip speeds while keeping the manufacturing yield high. There are many sources of CD variation, the most common being variations in exposure energy (or "dose") and focus.

The depth of focus (DOF) for a lithography system is given by [6]

$$DOF = k_2 \frac{\lambda}{NA^2}, \tag{2.2}$$

where k_2 is another process parameter. Therefore, increasing the numerical aperture in an attempt to gain resolution has a dramatic effect on the depth of focus, making it much harder to obtain a stable process. In addition, recent lenses operate at such a high NA that some of the most oblique waves will be near Brewster's angle [11], which can lead to unintended polarization effects [10].

In addition to focus and exposure variations, there are a variety of other sources of CD variation, including mask errors, lens aberrations, film thickness non-uniformities, post-exposure bake temperature variation, and many others. In addition, CD variation may have complex spatial and temporal structure [12]. A great deal of effort is currently investigated in reducing these sources of CD variation or minimizing the sensitivity of the process to them.

2.1.4 Lithography Equipment

A schematic diagram showing the main components of a projection lithography tool is shown in Figure 2.2. These components include an illumination source, condenser optics, a mask, projection optics, and a wafer stage.

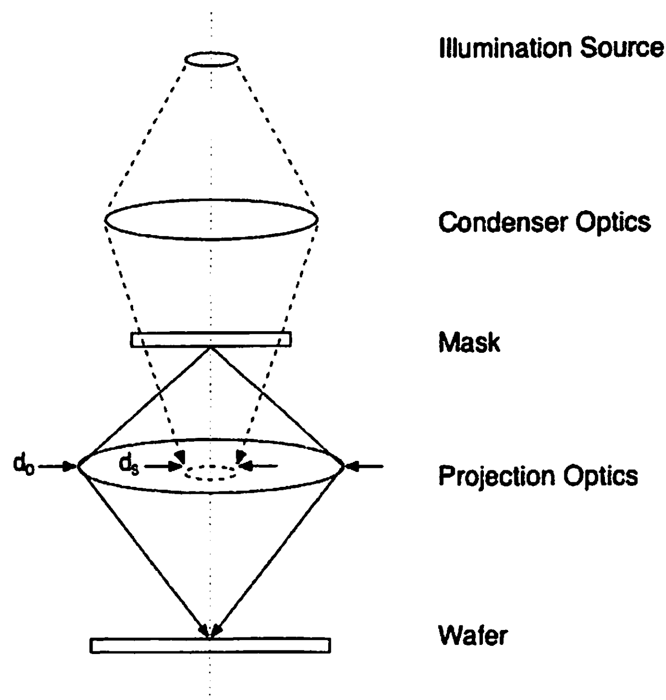

Figure 2.2: Schematic diagram of a projection lithography system.

For current deep ultraviolet (DUV) lithography tools the illumination source is most often an excimer laser operating at a wavelength of either 248 nm (KrF excimer) or 193 nm (ArF excimer). Future tools such as extreme ultraviolet lithography systems may require alternative source types. The light from the source is collected by the condenser optics and directed toward the mask. Typically the condenser optics are designed to form an

image of the source in the entrance pupil of the projection optics, an arrangement known as Köhler illumination. A key advantage of Köhler illumination is that a pupil at the condenser may be used to control the numerical aperture of the illumination system and, therefore, the size of the source image in the pupil (d_s in Fig. 2.2) [8]. This allows for control of the degree of partial coherence σ of the illumination according to the following relationship:

$$\sigma = \frac{d_s}{d_o} = \frac{NA_c}{NA_o}, \tag{2.3}$$

where d_o is the diameter of the objective lens entrance pupil, NA_c is the numerical aperture of the condenser lens, and NA_o is the numerical aperture of the objective lens. Tuning the partial coherence is critical to achieving best imaging performance.

The photomask for DUV lithography systems is typically made of quartz with an opaque chrome layer which is patterned to define the image to be transferred to the wafer (typically one or more individual chips). The mask is illuminated from above and an image is formed by the projection optics at the wafer surface. Note that although the condenser and projection optics are shown schematically in Fig. 2.2 as single lenses, in reality these are extremely complex optical systems with many elements, both reflective and refractive.

Two strategies are employed for wafer exposure using lithography tools. Because the mask image is typically a small fraction of the total wafer area (current state-of-the-art facilities use wafers with a diameter of 300 mm, while exposure tools typically image a field-of-view on the order of 20 mm × 30 mm), some form of systematic repetition is necessary. Step-and-repeat systems form the entire mask image at once, then move the wafer slightly and repeat the imaging process. Step-and-scan systems image only a narrow portion of the

mask at once, and move both the mask and the wafer simultaneously in order to image the entire mask. This process relaxes some of the constraints of optical design for a large field-of-view, allowing for improved image performance. At present, the current state-of-the-art systems employ a step-and-scan strategy, and have a theoretical throughput on the order of 120 300-mm wafers per hour.

2.2 Extreme Ultraviolet Lithography

As the physical limitations of conventional optical lithography become increasingly difficult to overcome, the search for a next-generation lithography (NGL) technology has intensified. Many NGL candidates have been investigated to varying degrees, including electron beam lithography (both projection and direct-write), immersion lithography, imprint lithography, and extreme ultraviolet (EUV) lithography. The work presented here is done in the context of EUV lithography, so this section provides a brief introduction to EUV lithography technology, differences from DUV optical lithography, and the details of the experimental setup used throughout for the experiments described in subsequent chapters.

2.2.1 Motivation for EUV Lithography

As discussed in Section 2.1.3, three basic strategies have been employed in the past in an effort to improve the resolution of lithography tools. However, at present these strategies are all meeting physcal limitations that make continued incremental scaling difficult at best. The k_1 value for modern lithography processes is near practical limits, and the numerical aperture of modern tools is approaching unity, the maximum possible value in air

(this value could be extended to perhaps 1.4 through the use of an immersion fluid between the last optical element and the wafer, an approach which now seems almost certain to find use in manufacturing).

The primary method for increasing resolution has been to decrease the illumination wavelength, from 436 nm (mercury G-line) to 365 nm (mercury I-line) to 248 nm (KrF excimer) and finally to 193 nm (ArF excimer). However, continued reduction of the wavelength is limited by material properties. Most materials become absorptive at wavelengths below about 190 nm. Although much research has been done on lithography at a wavelength of 157 nm (F_2 excimer), this technology requires a new lens material (CaF_2) because current lens materials (primarily quartz) are too absorptive at that wavelength. In addition, the ambient atmosphere of the tool must be purged and replaced with nitrogen, as oxygen is also too absorptive. Such costly and difficult changes may outweigh the potential benefits for this technology, which may only be useful for one technology node past 193 nm lithography. However, the possibility for lithography at a wavelength near 13.5 nm exists because of the development of multilayer coatings which are reflective at this wavelength. Although this technology has many challenges, it also offers a large benefit in terms of resolution.

2.2.2 EUV Lithography Technology

Although EUV lithography is similar in principle to deep-UV lithography, the fact that virtually all materials are highly absorptive in the extreme UV portion of the electromagnetic spectrum (photon energies of about 30 eV to about 250 eV, with corresponding wavelengths in vacuum from about 5 nm to about 40 nm) requires significant changes to the

equipment design [13]. First, the imaging process must be carried out in a near-vacuum to avoid absorption by gases in the ambient atmosphere. Also, refractive optics can no longer be used, since the EUV radiation would be absorbed by the lenses. Therefore, reflective optics consisting of multilayer mirrors are used instead. Unfortunately, an all-reflective imaging system is more difficult to design than a refractive system because mirrors have fewer degrees of freedom to vary than do lenses [13]. Consequently, many of the mirrors in an EUV lithography system will have aspheric surfaces [14]. Photomasks must also be reflective, which leads to several difficulties not encountered with normal transmissive masks. In order to achieve the high throughput required for high-volume manufacturing, high-power sources of EUV radiation will be required. At present, there is no source which meets this requirement, but potential options are discussed below.

Multilayer Mirrors

As mentioned previously, virtually all materials are strongly absorptive at EUV wavelengths, making the use of refractive optical elements impractical. Therefore, EUV lithography systems must be catoptric (composed entirely of reflective elements). Since there are no single materials with a high enough reflectivity to be useful as mirrors, multilayer interference coatings, also known as multilayer mirrors, are used instead.

Multilayer mirrors are formed by depositing alternating layers of two materials with different refractive indices. The materials must be chosen such that they form a long-term stable interface, and normally one material has a low atomic number (Z) while the other has a high atomic number in order to maximize the difference in electron density [15]. The multilayer materials are also generally amorphous or polycrystalline. The periodicity

of the layer pairs is designed to be $\lambda/2$ for normally-incident radiation of wavelength λ, so that the reflections from each layer interface interfere constructively. This arrangement is shown schematically in Figure 2.3.

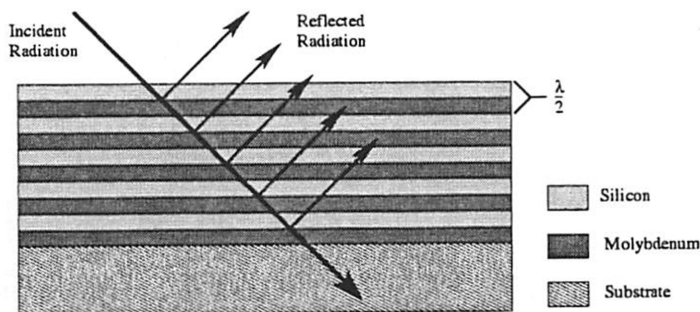

Figure 2.3: Operation of a multilayer interference coating.

The leading multilayer mirror candidate for use in EUV lithography uses alternating layers of silicon and molybdenum, first demonstrated by Barbee et al [16]. The calculated normal-incidence reflectivity [17] for a silicon-molybdenum multilayer with a period of 6.9 nm and 40 layer pairs is shown in Figure 2.4. In practice, peak reflectivities on the order of 65–70% are typical.

While this reflectivity is far from ideal since a large amount (about 25%) of incident radiation is lost at each mirror, it is sufficient to make a usable optical system at EUV wavelengths. For this reason, development of EUV lithography systems has centered around silicon/molybdenum multilayers and a source wavelength of 13.4–13.5 nm. It should also be noted that film stress in the multilayers and thermal loads on the mirrors can affect imaging performance with these optic types. Film stress can typically be compensated for during alignment of the optical elements, while thermal loads may introduce a focal shift which must be accounted for [18].

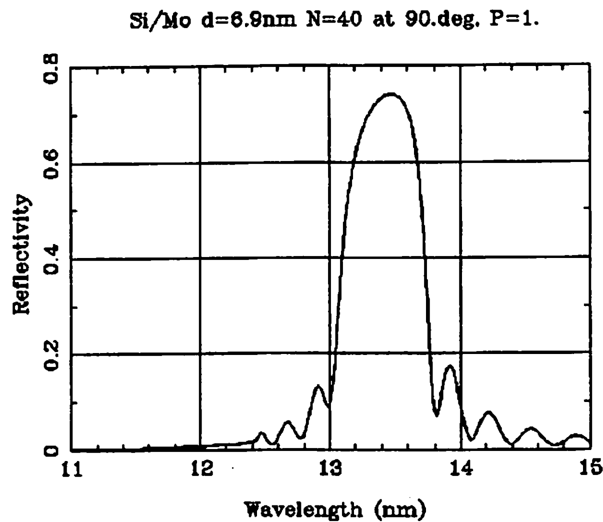

Figure 2.4: Normal-incidence reflectivity of a silicon/molybdenum multilayer with a period of 6.9 nm and 40 layer pairs, showing a peak of about 75% at a wavelength of about 13.5 nm. From [17].

EUV Photomasks

Photomasks for EUV lithography are reflective, unlike the transmissive masks used in deep-UV lithography. EUV masks consist of a multilayer mirror (matched to the projection optics to provide peak reflectivity at the desired wavelength) with a patterned [19] absorbing material on the surface. A schematic of this mask type is shown in Figure 2.5. There are several possible absorbing materials, such as chromium [20], aluminum [21], aluminum-copper, titanium, titanium nitride, tantalum, and tantalum nitride.

Several issues still remain with EUV masks. Perhaps the most serious issue is the repair of mask defects [22]. Defects in the patterned absorber layer can be repaired using focused ion beam [23] or electron beam [24] methods. In order to avoid damage to the underlying multilayer coating from the ion beam, a buffer layer such as silicon dioxide

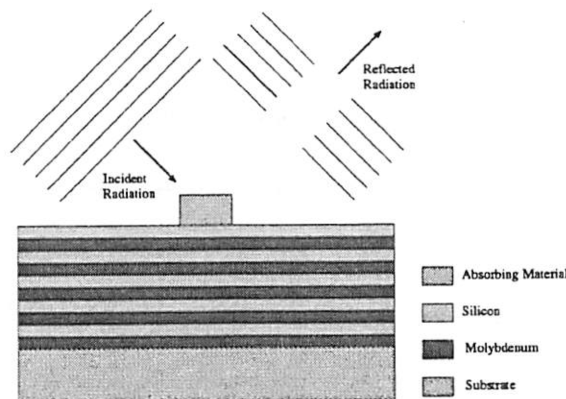

Figure 2.5: Schematic of a reflective mask fabricated using multilayer coating.

may be used. Once the mask pattern defects have been repaired, this buffer layer may be removed. However, no solution exists for repairing defects in the multilayer coating.

These defects may take one of two forms: phase defects and amplitude defects [13, 25]. Phase defects occur when a localized thickness defect occurs in a layer within the coating, causing reflections at that point to be out of phases with other reflections, inhibiting constructive interference [26]. Amplitude defects occur when some material on the surface of the multilayer coating causes unwanted absorption.

In addition, mask feature properties such as side wall angle, corner radius, and absorber thickness have been shown to have important effects on the resulting aerial image [27]. Mask inspection for locating defects is also challenging. One method for dealing with this issue is to use an extra thin layer on top of the multilayer stack to facilitate rapid inspection at wavelengths in the DUV range. Finally, the use of pellicles (thin membranes used to protect the mask surface from contamination) will not be possible for EUV masks due to undesirable absorption [13]. Therefore, another solution must be found.

EUV Sources

There are two primary options for sources of EUV radiation for lithography applications: laser-produced plasmas and electric discharge sources. The source must achieve a minimum of 60 W of in-band EUV power to meet throughput requirements [28].

The primary laser produced plasma being developed for EUV lithography applications uses a cooled supersonic nozzle to produce a dense beam of xenon clusters as the plasma source target. This cluster beam is then irradiated with a pulsed laser to produce a high-temperature plasma radiating efficiently in the EUV spectral region [29,30,31].

An electric discharge source is also under development. This source works by pumping xenon gas through a capillary, where an electrical discharge creates a plasma which radiates in the EUV spectrum. This EUV source type is smaller and more cost effective than the laser produced plasma source, but there are challenges in obtaining sufficient power and controlling debris to overcome [32,33,34].

At this point, it seems that either laser-produced plasmas or discharge sources could be optimized to meet the physical requirements. The final identification of the source for EUV lithography has not been made, and it will likely be dominated by issues surrounding cost of ownership, component lifetime (including electrode erosion and debris), and compatibility with an effective condenser design [34,35].

2.3 Experimental Setup

Although not practical for production use with EUV lithography tools, synchrotrons can also serve as a source of EUV radiation, and have been quite useful in optical metrology

and early development of EUV systems. The Advanced Light Source (ALS), a synchrotron facility at Lawrence Berkeley National Laboratory (LBNL), has been used for this purpose [36, 37]. Using an undulator as a source of EUV radiation [38], a variety of optical systems have been characterized and used for lithographic printing.

2.3.1 The Micro-Exposure Tool (MET)

The current setup is based upon the Micro-Exposure Tool (MET) optic. This optical system is composed of two aspheric elements coated with reflective multilayers. It has a numerical aperture of 0.3, a $5\times$ demagnification factor, and a static field size of 600 μm $\times$ 200 μm. In addition, the MET optic has a central obscuration with a numerical aperture of 0.1 (*i.e.*, a radius of approximately 1/3 of the full pupil). This is a very significant difference from most lithography systems (which typically have no obscuration), and must be accounted for in all modeling. The MET system is operated at a wavelength of 13.5 nm, using an undulator with a period of 8 cm as the source. A schematic diagram of the MET system is shown in Figure 2.6. Here EUV radiation from the undulator is incident upon two scanning mirrors which allow for programmable illumination shapes (pupil fills) [39]. The illumination is then directed onto the mask by a toroidal mirror. The resulting aerial image of the mask pattern is then formed at the wafer surface by the MET optic itself.

The MET system includes both wafer and reticle vacuum load-locks, and accepts standard 6"-size reticles. Metrology capabilities built into the tool include wafer-height sensors for proper focus determination, *in-situ* dose monitor, and illumination pupil-fill monitor.

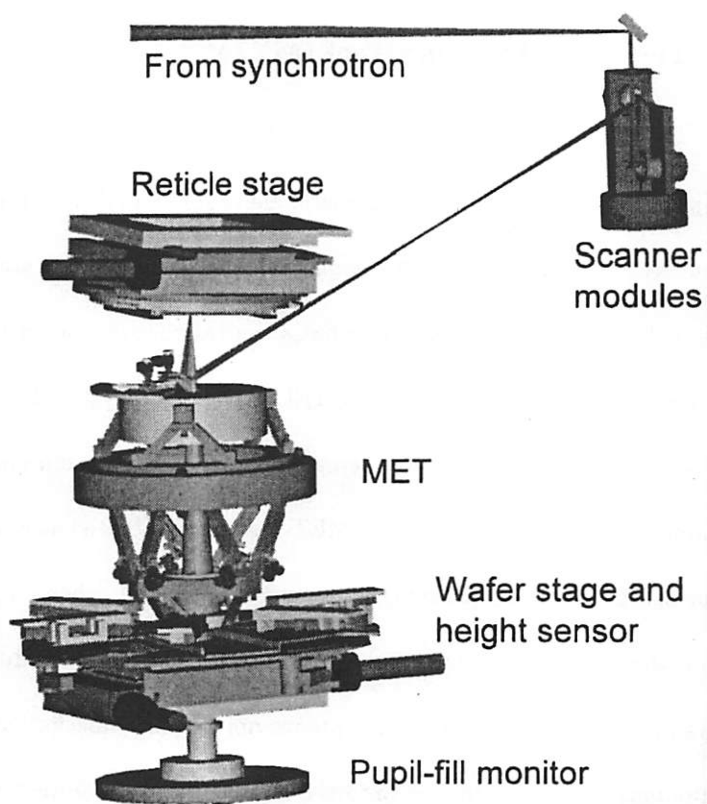

Figure 2.6: Schematic diagram of the Micro-Exposure Tool (MET) system. Courtesy Patrick Naulleau, Lawrence Berkeley National Laboratory.

2.3.2 Photoresist Processing Equipment

A cleanroom adjacent to the MET system provides resist-processing capabilities. Resist coating and post-application bake is performed on a Brewer Science dual-module spin and bake unit with a single temperature zone hotplate (10"×10"). Post-exposure bake is performed on a second Brewer Science bake plate (7"×7") located immediately adjacent to the wafer load-lock in order to minimize the delay between exposure and PEB. Development is performed on a Brewer Science automated developer.

2.4 CD Error Budget Analysis

Control of CD variation is extremely important for cost-effective semiconductor manufacturing. As mentioned previously, there are many sources of CD variation, and understanding the contributions of each of these sources to the total amount of variation is critical to specifying process tolerances and targeting areas for improvement. The process of decomposing the total CD variation into its component sources is known as error budget analysis. The overall theme of this dissertation is the characterization of error budget components for EUV lithography, and therefore this section provides an introduction to error budget analysis.

2.4.1 International Technology Roadmap for Semiconductors

The International Technology Roadmap for Semiconductors (ITRS) [40] is a document prepared yearly by a panel of experts from industry and academia which attempts to forecast the future trends of virtually all aspects of semiconductor processing, including

Table 2.1: ITRS predictions for the 32-nm technology node [40].

	2004	2013
DRAM half-pitch	90 nm	32 nm
Dense-line CD control (3σ)	11.0 nm	3.9 nm
MPU gate length in resist	53 nm	18 nm
MPU gate length after etch	37 nm	13 nm
MPU gate CD control (3σ)	3.3 nm	1.2 nm
Contact in resist	122 nm	42 nm
Line width roughness (3σ)	3.0 nm	1.0 nm
CD metrology tool precision (3σ)	0.7 nm	0.2 nm
Overlay control	32 nm	12.8 nm
Wafer diameter	300 mm	450 mm

lithography technology. Among the predictions are requirements for total CD control and certain components of the CD error budget, such as metrology precision.

Currently EUV lithography is predicted to enter production use at the 32-nm technology node, which is listed on the most recent ITRS update (2004) to begin in the year 2013 (note that the ITRS predicts a three-year interval between technology nodes, while some semiconductor manufacturers predict a two-year interval). Some relevant specifications from the ITRS for this node are shown in Table 2.1, along with current (2004) values from the ITRS for comparison.

2.4.2 Error Budget Methodology

Characterization of the critical dimension error budget requires determination of the CD sensitivity to various process effects and variations. For example, the amount of CD change expected for a unit change in exposure dose. The total amount of CD variation measured in the process may then be decomposed into its constituent components based on the sensitivities and direct measurement of the process parameter variations or statistical

inference from process data. There are very many sources of critical dimension variations, and as such the scope of a complete error budget analysis is very broad. In this work, only the sources of variation related to the lithography process are studied. These components may be generally grouped into categories related to optics (Chapter 3), resists (Chapter 4), and metrology (Chapter 5).

Once the error budget is constructed, the most appropriate path towards process improvement can be selected. This may take the form of tightening process parameter specifications (*e.g.*, reducing across-wafer PEB temperature variation) or taking steps to reduce the CD sensitivity to a particular process parameter (*e.g.*, adjusting the exposure process to operate near the isofocal point to minimize CD sensitivity to focus errors). Knowledge of the CD error budget is therefore critical to achieving and maintaining a stable, high-yield manufacturing process.

Chapter 3

Characterization of Projection Optics in EUV Lithography Tools

As lithography systems have evolved toward greater resolution, the quality of the projection optics has become an increasing concern. This chapter discusses different aspects of optical quality and lithographic means for measuring them.

3.1 Aberrations and Flare

Imperfections in the surface of an optical element may in general be grouped into three classifications based on their spatial frequency. Low-spatial frequency lens imperfections are referred to as aberrations, and can cause distortions, pattern displacements, and focus shifts in the aerial image (the projected image of the mask at the wafer). Mid-spatial frequency imperfections cause an effect known as stray light or flare, in which light from bright regions of the image is scattered into dark regions. This is often modeled as an

increased background intensity, leading to a reduction of aerial image contrast. The high spatial frequency components (surface roughness) scatter light out of the optical system. This translates to a decrease in intensity at the wafer (and therefore a loss of throughput), but does not otherwise affect the quality of the aerial image. As such, high-frequency roughness is not considered here.

3.1.1 Aberrations

In an ideal diffraction limited optical system, a point source in the object (mask) plane will produce a perfect spherical wave in the exit pupil which converges toward the geometrical image point in the image plane [41]. Lens aberrations (also known as lens figure errors) cause deviations in the exit-pupil wavefront from the ideal spherical wave. Aberrations may be the result of misalignment of individual optical elements, or they may simply be inherent in the optical design. The deviations from the ideal wavefront (also called optical path-length errors) are captured in the aberration function $W(x, y)$ in rectangular coordinates or, more commonly, $W(\rho, \theta)$ in polar coordinates. The aberration function $W(\rho, \theta)$ may be split into terms of a polynomial expansion using Zernike polynomials. This allows for separation of wavefront into different aberration types, each with a different physical effect.

Zernike Polynomials

Aberrations in optical systems are often characterized by Zernike polynomials [42]. An arbitrary wavefront $W(\rho, \theta)$, where (ρ, θ) are polar coordinates within the pupil, can be expanded in terms of a complete set of Zernike polynomials which are orthogonal over

a unit circle. For a circular pupil, the wavefront function may be expressed as a sum of Zernike circle polynomials [43]:

$$W(\rho,\theta) = \sum_{j=1}^{\infty} a_j Z_j(\rho,\theta), \tag{3.1}$$

where j is a polynomial-ordering index, a_j is the jth aberration coefficient, and Z_j is the jth Zernike polynomial given by

$$Z_{\text{even}j}(\rho,\theta) = \sqrt{2(n+1)}R_n^m(\rho)cos(m\theta), \quad m \neq 0 \tag{3.2}$$

$$Z_{\text{odd}j}(\rho,\theta) = \sqrt{2(n+1)}R_n^m(\rho)sin(m\theta), \quad m \neq 0 \tag{3.3}$$

$$Z_j(\rho,\theta) = \sqrt{n+1}R_n^0(\rho), \quad m = 0, \tag{3.4}$$

where m is the azimuthal order, n is the radial order, and $R_n^m(\rho)$ is the radial polynomial. The radial polynomials are a special case of Jacobi polynomials [44] and satisfy the orthogonality and normalization condition

$$\int_0^1 R_n^m(\rho)R_{n'}^m(\rho)\rho d\rho = \frac{1}{2(n+1)}\delta_{nn'} \tag{3.5}$$

where $\delta_{nn'}$ is a Kronecker delta function and

$$R_n^m(1) = 1. \tag{3.6}$$

The radial polynomial $R_n^m(\rho)$ may be factored [44] according to

$$R_{2n-m}^{m}(\rho) = Q_n^m(\rho)\rho^m, \tag{3.7}$$

where $Q_n^m(\rho)$ is a polynomial of order $2(n-m)$ and can be expressed as

$$Q_n^m(\rho) = \sum_{s=0}^{n-m} (-1)^s \frac{(2n-m-s)!}{s!(n-s)!(n-m-s)!} \rho^{2(n-m-s)}. \tag{3.8}$$

The Zernike polynomials have the advantage that the aberration coefficients (except for a_1) correspond to the standard deviation of each individual term. A few important Zernike circle polynomials are shown in Figure 3.1. Unfortunately, the ordering of the Zernike terms is not universally agreed to. However, a table of the first 37 Zernike terms following the "fringe" order of Wyant and Creath [44] is given in Table 3.1. This ordering method seems to be in common use in photolithography applications, and the Zernike expansion is often truncated at 36 or 37 terms when describing a wavefront.

Although the Zernike circle polynomials are of great use for optical systems with circular pupils, they are inappropriate for other pupil shapes. For systems with annular pupils (such as the MET optic–see Section 2.3.1), the Zernike annular polynomials may be used instead [45, 46, 47]. In this case Eq. 3.1 becomes

$$W(\rho, \theta; \epsilon) = \sum_{j=1}^{\infty} a_j Z_j(\rho, \theta; \epsilon), \tag{3.9}$$

where ϵ is the radius of the central obscuration,

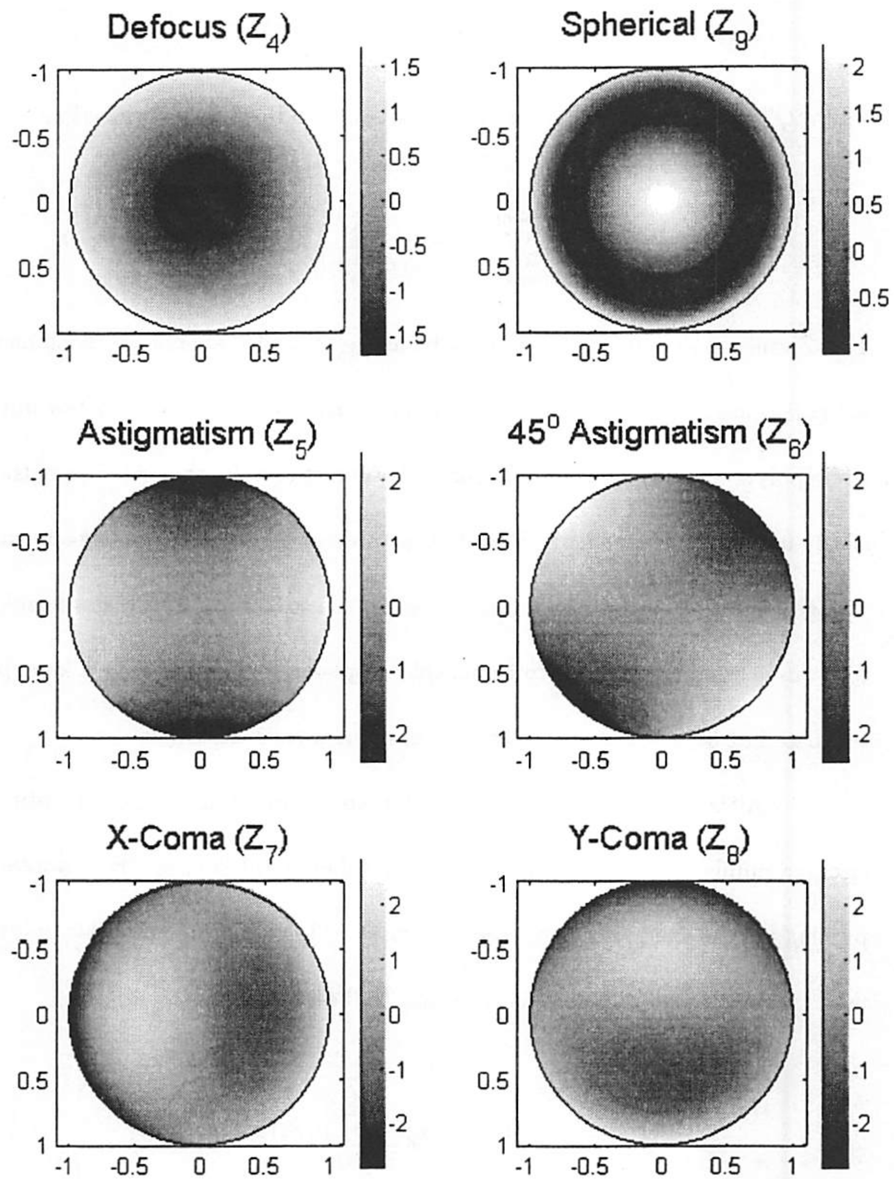

Figure 3.1: Some important Zernike circle polynomials.

Table 3.1: The first 37 Zernike circle polynomials, following the "fringe" ordering method of Wyant and Creath [44].

n	m	j	Z_j	Name
0	0	1	1	Piston
1	1	2	$\rho\cos\theta$	x-Tilt
1	1	3	$\rho\sin\theta$	y-Tilt
1	0	4	$2\rho^2-1$	Defocus
2	2	5	$\rho^2\cos 2\theta$	Primary Astigmatism
2	2	6	$\rho^2\sin 2\theta$	Primary 45°-Astigmatism
2	1	7	$(3\rho^2-2)\rho\cos\theta$	Primary x-Coma
2	1	8	$(3\rho^2-2)\rho\sin\theta$	Primary y-Coma
2	0	9	$6\rho^4-6\rho^2+1$	Spherical
3	3	10	$\rho^3\cos 3\theta$	Primary x-Trifoil
3	3	11	$\rho^3\sin 3\theta$	Primary y-Trifoil
3	2	12	$(4\rho^2-3)\rho^2\cos 2\theta$	Secondary Astigmatism
3	2	13	$(4\rho^2-3)\rho^2\sin 2\theta$	Secondary 45°-Astigmatism
3	1	14	$(10\rho^4-12\rho^2+3)\rho\cos\theta$	Secondary x-Coma
3	1	15	$(10\rho^4-12\rho^2+3)\rho\sin\theta$	Secondary y-Coma
3	0	16	$20\rho^6-30\rho^4+12\rho^2-1$	Secondary Spherical
4	4	17	$\rho^4\cos 4\theta$	Primary x-Tetrafoil
4	4	18	$\rho^4\sin 4\theta$	Primary y-Tetrafoil
4	3	19	$(5\rho^2-4)\rho^3\cos 3\theta$	Secondary x-Trifoil
4	3	20	$(5\rho^2-4)\rho^3\sin 3\theta$	Secondary y-Trifoil
4	2	21	$(15\rho^4-20\rho^2+6)\rho^2\cos 2\theta$	Tertiary Astigmatism
4	2	22	$(15\rho^4-20\rho^2+6)\rho^2\sin 2\theta$	Tertiary 45° Astigmatism
4	1	23	$(35\rho^6-60\rho^4+30\rho^2-4)\rho\cos\theta$	Tertiary x-Coma
4	1	24	$(35\rho^6-60\rho^4+30\rho^2-4)\rho\sin\theta$	Tertiary y-Coma
4	0	25	$70\rho^8-140\rho^6+90\rho^4-20\rho^2+1$	Tertiary Spherical
5	5	26	$\rho^5\cos 5\theta$	Primary x-Pentafoil
5	5	27	$\rho^5\sin 5\theta$	Primary y-Pentafoil
5	4	28	$(6\rho^2-5)\rho^4\cos 4\theta$	Secondary x-Tetrafoil
5	4	29	$(6\rho^2-5)\rho^4\sin 4\theta$	Secondary y-Tetrafoil
5	3	30	$(21\rho^4-30\rho^2+10)\rho^3\cos 3\theta$	Tertiary x-Trifoil
5	3	31	$(21\rho^4-30\rho^2+10)\rho^3\sin 3\theta$	Tertiary y-Trifoil
5	2	32	$(56\rho^6-105\rho^4+60\rho^2-10)\rho^2\cos 2\theta$	Quaternary x-Astigmatism
5	2	33	$(56\rho^6-105\rho^4+60\rho^2-10)\rho^2\sin 2\theta$	Quaternary y-Astigmatism
5	1	34	$(126\rho^8-280\rho^6+210\rho^4-60\rho^2+5)\rho\cos\theta$	Quaternary x-Coma
5	1	35	$(126\rho^8-280\rho^6+210\rho^4-60\rho^2+5)\rho\sin\theta$	Quaternary y-Coma
5	0	36	$252\rho^{10}-630\rho^8+560\rho^6-210\rho^4+30\rho^2-1$	Quaternary Spherical
6	0	37	$924\rho^{12}-2772\rho^{10}+3150\rho^8-1680\rho^6+$ $420\rho^4-42\rho^2+1$	Quinary Spherical

$$Z_{\text{even}j}(\rho,\theta;\epsilon) = \sqrt{2(n+1)}R_n^m(\rho;\epsilon)cos(m\theta), \quad m \neq 0 \tag{3.10}$$

$$Z_{\text{odd}j}(\rho,\theta;\epsilon) = \sqrt{2(n+1)}R_n^m(\rho;\epsilon)sin(m\theta), \quad m \neq 0 \tag{3.11}$$

$$Z_j(\rho,\theta;\epsilon) = \sqrt{n+1}R_n^0(\rho;\epsilon), \quad m = 0, \tag{3.12}$$

and $R_n^m(\rho;\epsilon)$ is a radial annular polynomial. These polynomials are orthogonal over an annular pupil, *i.e.*,

$$\int_\epsilon^1 R_n^m(\rho;\epsilon)R_{n'}^m(\rho;\epsilon)\rho d\rho = \frac{1-\epsilon^2}{2(n+1)}\delta_{nn'}. \tag{3.13}$$

The radial polynomials $R_n^m(\rho;\epsilon)$ are given by [47]

$$R_n^m(\rho;\epsilon) = N_n^m \left[R_n^m(\rho) - \sum_{i\geq 1}^{(n-m)/2} (n-2i+1)\langle R_n^m(\rho)R_{n-2i}^m(\rho;\epsilon)\rangle R_{n-2i}^m(\rho;\epsilon) \right], \tag{3.14}$$

where N_n^m is a normalization constant, $R_n^m(\rho)$ is the radial polynomial for circular pupils, and

$$\langle R_n^m(\rho)R_{n'}^m(\rho;\epsilon)\rangle = \frac{2}{1-\epsilon^2}\int_\epsilon^1 R_n^m(\rho)R_{n'}^m(\rho;\epsilon)\rho d\rho, \tag{3.15}$$

$$R_{2n}^0(\rho;\epsilon) = R_{2n}^0 \left[\left(\frac{\rho^2-\epsilon^2}{1-\epsilon^2} \right)^{1/2} \right], \tag{3.16}$$

$$R_n^n(\rho;\epsilon) = \rho^n \left[(1-\epsilon^2)/(1-\epsilon^{2(n+1)})\right]^{1/2}, \tag{3.17}$$

$$R_n^{n-2}(\rho;\epsilon) = \frac{n\rho^n - (n-1)\left[(1-\epsilon^{2n})/(1-\epsilon^{2(n-1)})\right]\rho^{n-2}}{\left\{(1-\epsilon^2)^{-1}\left[n^2(1-\epsilon^{2(n+1)}) - (n^2-1)(1-\epsilon^{2n})^2/(1-\epsilon^{2(n-1)})\right]\right\}^{1/2}}. \tag{3.18}$$

A few important Zernike annular polynomials (corresponding to the Zernike circular polynomials in Figure 3.1) are shown in Figure 3.2.

3.1.2 Flare

Roughness (also known as finish errors) in the optical surfaces of higher spatial frequency than aberrations leads to non-specular scattering of light. The high-spatial frequency roughness will scatter light out of the image, reducing the throughput, while the mid-spatial frequency roughness (spatial frequencies in the 1/mm to 1/μm range [48]) will scatter light within the field of view. This phenomenon is known as flare (also called stray light), and in general it leads to a reduced aerial image contrast and therefore a reduced process window. The amount of flare present in an optical system is most often expressed as a percentage of the light in the clear field which appears in the dark areas. While the flare for DUV lithography tools has been reported to be about 2-6% [49, 50], the flare in early EUV lithography tools has been shown to be as high as 20-40% [51]. Production EUV lithography tools will need to achieve a flare level of less than 10% in order to meet CD control requirements [52].

The total integrated scatter (TIS) is defined as the ratio of the non-specular scat-

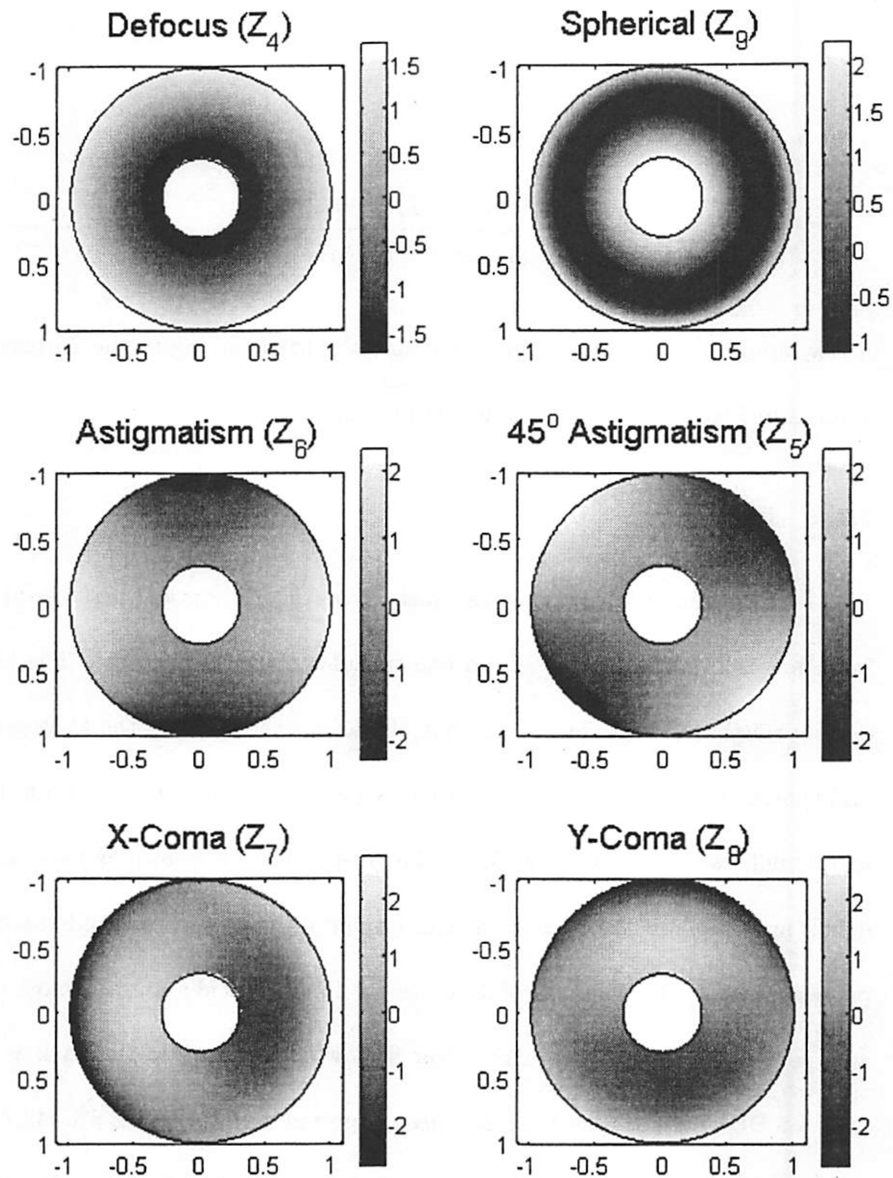

Figure 3.2: Some important Zernike annular polynomials ($\epsilon = 0.3$).

tered power to the reflected specular power when light is incident on a surface. The TIS is given by [53]

$$TIS = \frac{P_s}{RP_i} = \frac{P_s}{P_0} \simeq \left(\frac{4\pi\sigma_s \cos\theta_i}{\lambda}\right)^2, \tag{3.19}$$

where P_s is scattered power, R is the reflection coefficient, P_i is incident power, P_0 is specular reflected power, σ_s is the standard deviation of the surface roughness, θ_i is the angle of incidence, and λ is the wavelength of light illuminating the surface. As Eq. 3.19 shows, TIS is proportional to $1/\lambda^2$. Therefore, as the wavelength of illumination is decreased in an effort to increase resolution, the flare will increase dramatically for the same amount of optical surface roughness [54]. This places strict requirements on the optical finish quality.

The amount of flare at a given point in the field is also dependent on lens traffic which is set by the local pattern density surrounding that point (points with more absorbing layer surrounding them have lower flare and vice versa) and the proximity to the field edge [48, 52]. Therefore, the flare may vary significantly across the field, and this variation can lead to unwanted critical dimension variation. Therefore, some form of mask compensation may be required, possibly in the form of field-dependent CD resizing [55] or the use of dummy patterns to make the pattern density more uniform [52].

Several techniques have been developed for measuring and predicting flare in normal-incidence multilayer optics at EUV wavelengths, including angular scattering measurements [56, 57], knife-edge measurements [58], predictions from surface roughness measurements [57, 59, 58], interferometric methods [60, 61], and resist-based lithographic methods [51, 62].

3.1.3 Interferometric Measurements of the MET Wavefront

Lens aberrations in the projection optics are customarily measured using interferometry techniques before the optical system is installed in the tool. Although such measurements are typically not possible once the optics are installed in the tool and configured for production use, they still provide very valuable information about the optical quality of the system.

The Micro-Exposure Tool (MET) optic was measured using a variety of interferometry techniques, including phase shifting diffraction interferometry (PSDI) at visible wavelengths [63] and lateral shearing interferometry (LSI) and phase-shifting point diffraction interferometry (PS/PDI) [64] at EUV wavelengths [65, 66, 67, 68]. An example of the PS/PDI wavefront measurement is shown in Figure 3.3 for the center of the field. Under optimum optical alignment conditions, the wavefront variance in the first 37 Zernike terms was measured to be $\sigma_{37} = 0.55$ nm, or $\lambda/24.5$. Astigmatism, coma, and spherical aberration were removed through alignment, and the largest remaining aberrations were 0.14 nm trifoil and a relatively large 0.37 nm of higher-order spherical aberration [68].

3.2 Resist-Based Measurement of Flare

The flare in the MET optic was measured using a lithographic technique derived from Kirks method [69]. This method has been used previously to characterize other EUV optics [51], and uses simple cross patterns of varying size placed in an otherwise bright field. The full field layout for the flare experiment is shown in Figure 3.4, while a closer view of the cross patterns is shown in Figure 3.5. Wafers were coated with a 125 nm thick layer

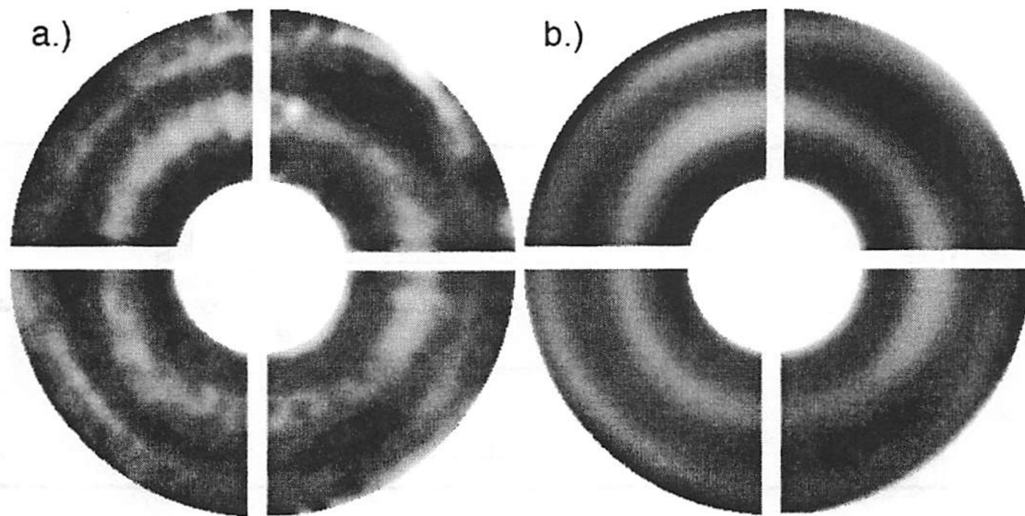

Figure 3.3: MET wavefront measured using phase-shifting point-diffraction interferometry (PS/PDI) at the center of the field. a.) Raw data, b.) fit to first 37 Zernike polynomials. Higher-order spherical aberration is clearly visible. Courtesy Ken Goldberg, Lawrence Berkeley National Laboratory.

of Rohm and Haas EUV-2D photoresist, and both post-application bake (PAB) and post-exposure bake (PEB) were performed at 130°C. The wafers were then exposed using the mask pattern shown in Figure 3.4 and annular illumination with $\sigma_{inner} = 0.3$, $\sigma_{outer} = 0.7$, and $\lambda = 13.5$ nm.

Flare for a given feature size is then defined as the exposure dose required to clear the resist in the bright region (E_0) divided by the dose to clear in the dark regions (E_{dark}):

$$\% \text{ Flare} = \frac{E_0}{E_{dark}} \times 100. \tag{3.20}$$

Flare measurements were initially performed using a scanning electron microscope (SEM). However, this led to unexpected results. As the exposure dose level was increased in an attempt to clear the resist in the cross patterns, the resist began to cross-link before

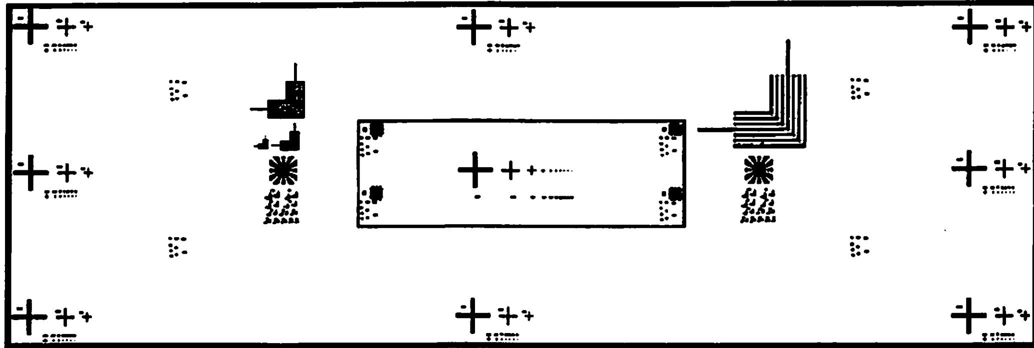

Figure 3.4: Field layout used for flare measurement.

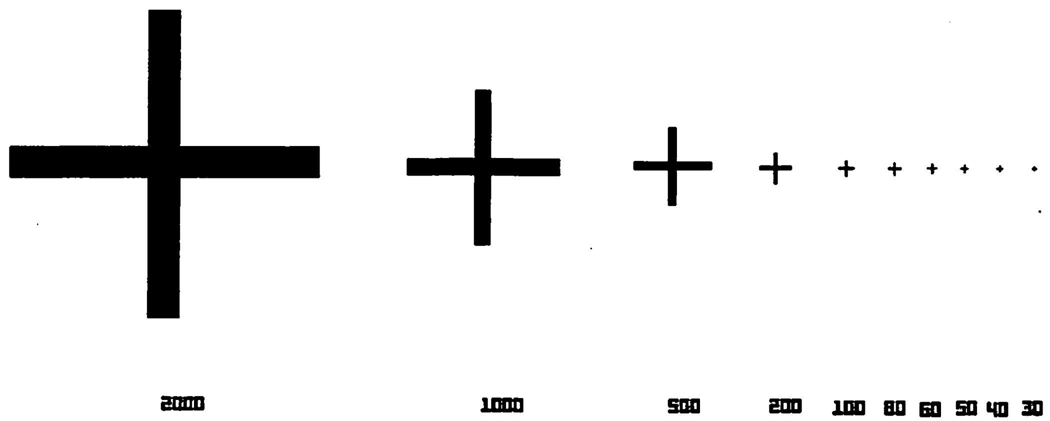

Figure 3.5: Cross patterns used for flare measurement.

the cross patterns disappeared. In a positive resist, cross-linking occurs when the exposed areas receive a very high dose which causes the resist molecules to link together. This cross-linking decreases the solubility of the resist relative to the unexposed areas, leading to a reversal of tone (*i.e.*, a positive resist will behave like a negative resist when cross-linking occurs). This is illustrated in Figure 3.6, showing the resist image of the cross patterns at a dose just below the cross-linking threshold, and Figure 3.7, showing the resist image at a dose just above the cross-linking threshold.

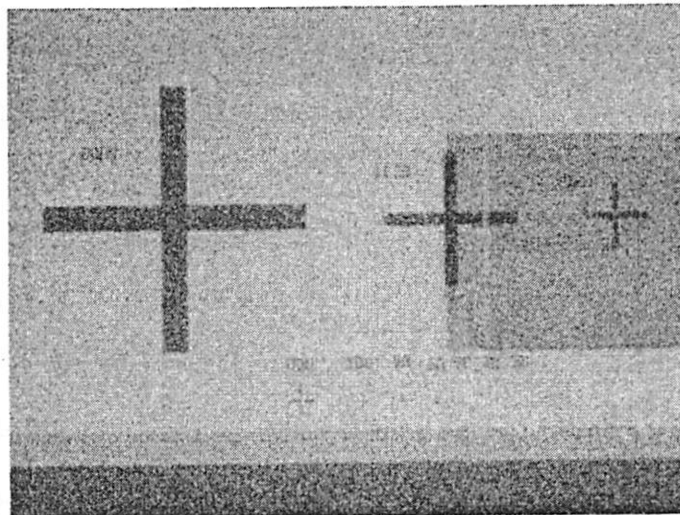

Figure 3.6: SEM image of cross patterns in Rohm and Haas EUV-2D resist at an exposure dose just below the cross-linking dose.

These observations from the SEM initially led to the conclusion that the dynamic range of the resist used (EUV-2D) was insufficient to measure the flare in the MET optic, and that the maximum measurable level of flare was less than 2%. However, this did not agree with the predicted intrinsic flare value of approximately 6.5% made from atomic-force microscopy (AFM) and optical scattering measurements of the surface roughness in the

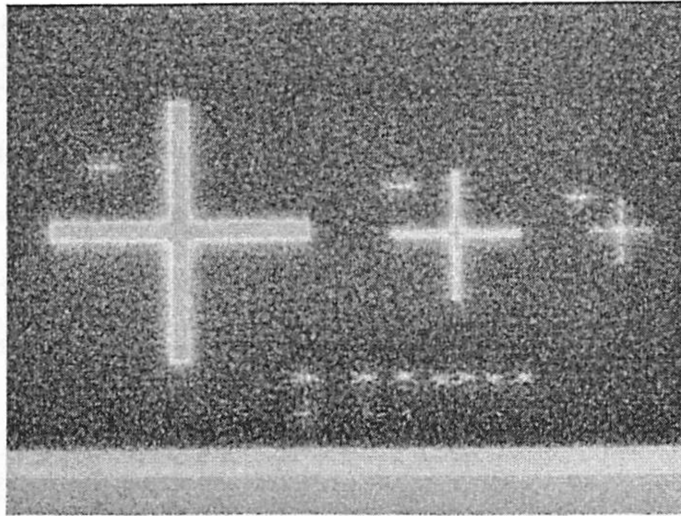

Figure 3.7: SEM image of cross patterns in Rohm and Haas EUV-2D resist at an exposure dose just above the cross-linking dose.

optic [70]

The flare measurements were then repeated using an optical microscope (100× objective with differential interference contrast). This analysis yielded very different results, as the cross patterns disappeared in the optical microscope well before the onset of resist cross-linking. In order to investigate this discrepancy, an AFM measurement was performed to determine the resist thickness in the cross patterns at a dose level at which the cross was visible in the SEM but not visible in the optical microscope. The measured resist thickness was approximately 1 nm. This suggests that significant top-surface loss is occurring in the resist such that only a very thin "scum" layer is remaining on the wafer surface. However, this "scum" layer seems to persist even at very high doses (past the resist cross-linking threshold). This process is illustrated in Figure 3.8.

Across-field contour maps of the flare measurements made using the optical micro-

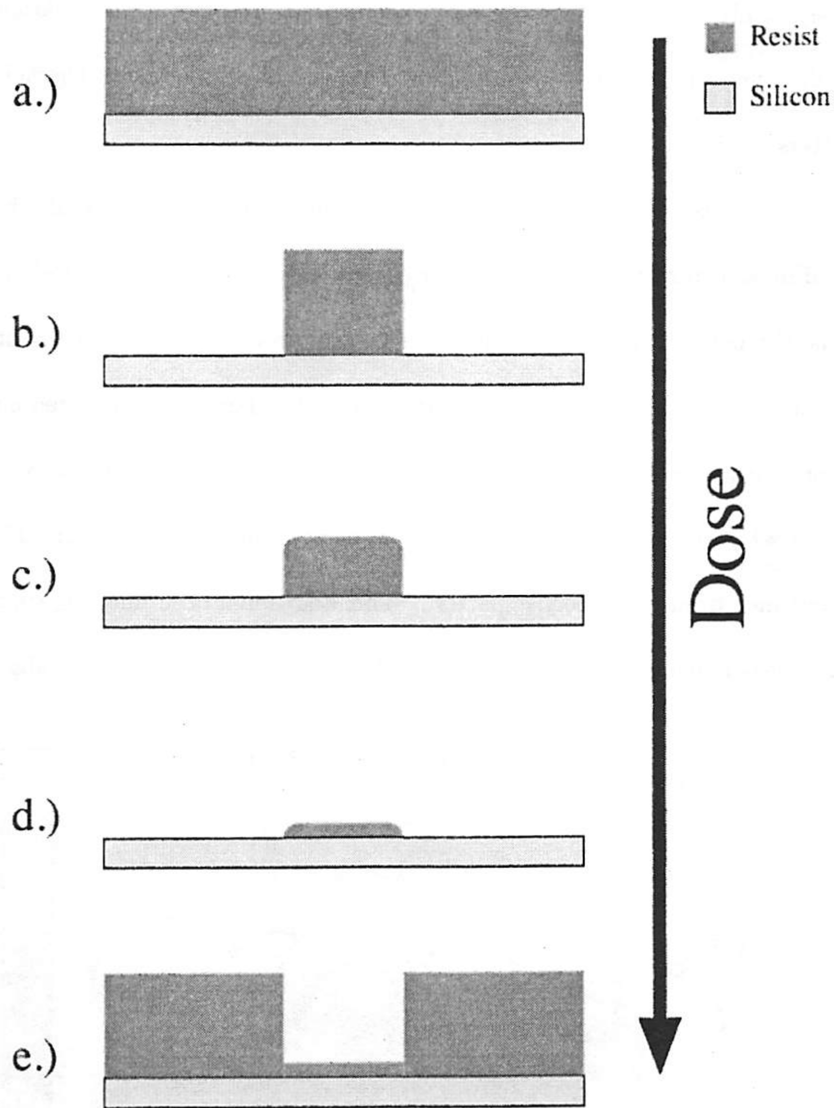

Figure 3.8: Schematic of resist behavior through dose in flare experiments. a.) Blanket resist at dose less than dose-to-clear (E_0), b.) resist pattern just above dose-to-clear (E_0), c.) resist shows top-loss as dose increases further, d.) at high doses only a very thin resist "scum" remains on the wafer that is visible in the SEM but invisible in an optical microscope, e.) at very high doses the resist cross-links and reverses tone.

scopes are shown for 500 nm, 1 μm, and 2 μm features in Figures 3.9, 3.10, and 3.11, respectively. Only the left side of the field is shown, as across-field illumination non-uniformity made interpretation of the results impossible at the right edge of the field where the test patters are located.

It should be noted that part of the apparent flare may be attributed to the non-ideal mask contrast (*i.e.*, the absorber pattern has non-zero reflectance). In order to determine the contribution of this effect, the *in-situ* dose sensor was used to measure the dose at the wafer plane with the illumination on both a large absorber area and a large multilayer reflective coated area. The ratio of the two dose measurements was 1%. Therefore, the cross patterns used in the flare experiments will receive an extra 1% dose just from reflectance from the absorber pattern. This additional dose must be subtracted from the flare measurements in order to separate the contributions of flare and absorber reflectance.

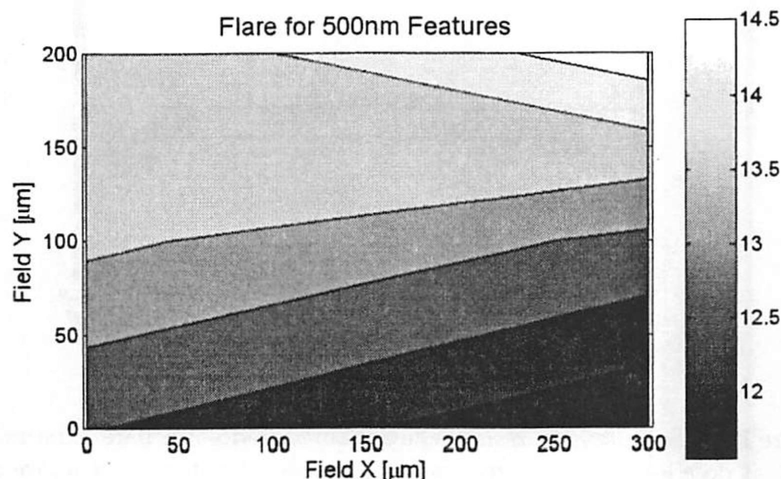

Figure 3.9: Contour map of flare in percent across the field for 500 nm features in the MET optic. Only the left side of the field is shown, as across-field illumination non-uniformity distorted the measurements for the right side of the field.

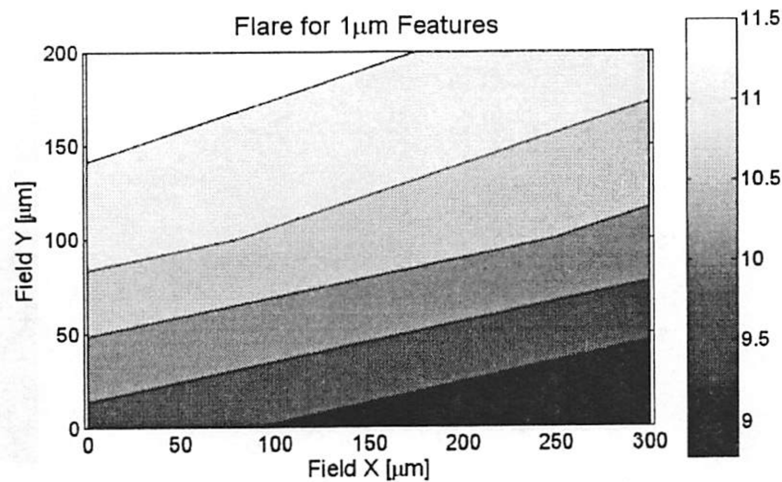

Figure 3.10: Contour map of flare in percent across the field for 1 μm features in the MET optic. Only the left side of the field is shown, as across-field illumination non-uniformity distorted the measurements for the right side of the field.

The likely reason that the measured flare is higher than the predicted value is that the predicted value assumes a field size of 600 $\times$ 200 μm. While this is the field size of the MET optic, the flare extends well beyond this range (up to mm-scale). Therefore, the flare seen in a given field is the sum of the flare for that field and the longer-range flare from all surrounding fields in the FEM. As the fields are only separated by 100 μm, the flare from surrounding fields is significant.

A second experiment was performed to determine if the density of exposures within the FEM did in fact affect the measured flare. The resist type, thickness, and processing parameters were all identical to the first flare experiment. However, in this case, the spacing of exposures within the FEM was changed from 100 μm in both the x- and y- directions to 800 μm in the x-direction and 400 μm in the y-direction. The limited area accessible

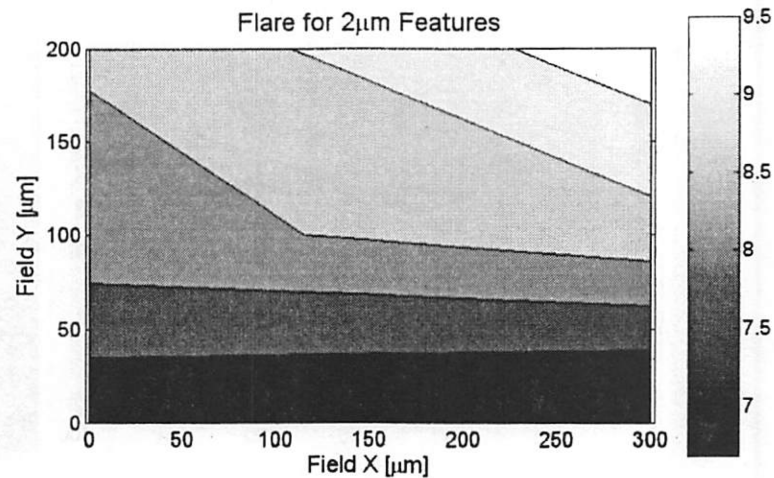

Figure 3.11: Contour map of flare in percent across the field for 2 μm features in the MET optic. Only the left side of the field is shown, as across-field illumination non-uniformity distorted the measurements for the right side of the field.

on the wafer (due to stage movement range limitations) and the need to print at a few different focus steps in order to ensure good focus made it necessary to restrict the range of dose values in order to fit the exposures into the allowable area of the wafer. The result of this restricted dose range was to limit the flare measurement to a single point within the field (variation in the relevant dose levels due to across-field illumination intensity non-uniformity caused the other points in the field to fall outside the restricted range). The center point of the field was chosen, and the dose targeted accordingly.

The result of this measurement showed flare values in the center of the field of 9.8% for 500 nm features, 7.8% for 1 μm features, and 5.8% for 2 μm features, a difference of approximately 3% from the more densely-spaced FEM at each feature size in the same location within the field. This evidence supports the conclusion that the initial flare

measurements are being influenced by surrounding fields. Therefore, it is very difficult to accurately measure the flare in this system lithographically. An accurate measurement requires that the fields in the FEM be placed relatively far apart in order to isolate them from each other. However, flare measurements by nature require a large dose range, and the accuracy also depends upon the step size within the dose range. This requirement, combined with the need to repeat each dose step at several focus settings in order to ensure best focus, implies the need for a large number of exposures. These two requirements (large spacing between exposures and large number of exposures) may be mutually exclusive given the limited area accessible on the wafer.

3.3 Measurement of Aerial Image Contrast

One important factor in determining the printing performance of a lithography tool is the aerial image contast, defined as

$$\text{contrast} = \frac{I_{max} - I_{min}}{I_{max} + I_{min}}, \tag{3.21}$$

where I_{max} and I_{min} are the maximum and minimum aerial image intensity, respectively (Figure 3.12). Typically a contrast of at least 50% is required for reliable printing performance [71]. Aerial image contrast is a function of feature size or, equivalently, of spatial frequency. For large features, the image contrast should ideally be unity, whereas for small features beyond the resolution limit of the optical system the contrast will be zero. The details of the transition between these two extremes depends on the parameters of the optical system, including numerical aperture, wavefront quality, and illumination wavelength and

partial coherence. This dependence on feature size brings about the concept of the contrast transfer function (CTF), a mapping of feature size or spatial frequency to the corresponding image contrast.

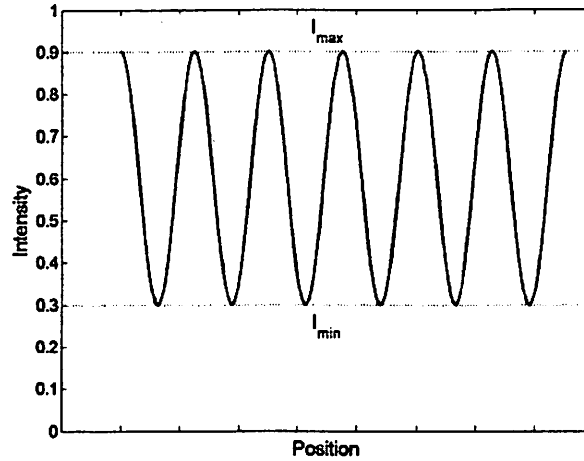

Figure 3.12: Illustration of aerial image contrast (see Equation 3.21).

Direct measurement of aerial image contrast is challenging. In this work a photoresist threshold technique [72, 73] is applied to measure I_{max} and I_{min}, from which the contrast can be calculated. This process is illustrated in Figure 3.13. As the exposure dose is increased from Fig. 3.13a.)-c.), the developed linewidth shrinks (here a simple resist threshold model of development is assumed). Therefore, I_{max} occurs at the exposure dose (D_{max}) at which individual lines first become evident in the resist while I_{min} occurs at the dose (D_{min}) at which the lines vanish completely and the resist clears. Therefore, the measured contrast becomes

$$\text{contrast} = \frac{D_{max} - D_{min}}{D_{max} + D_{min}}. \tag{3.22}$$

Resist images at dose levels D_{max} and D_{min} are shown in Figure 3.14. Measurement of the contrast for a range of feature sizes allows for reconstruction of the contrast transfer function.

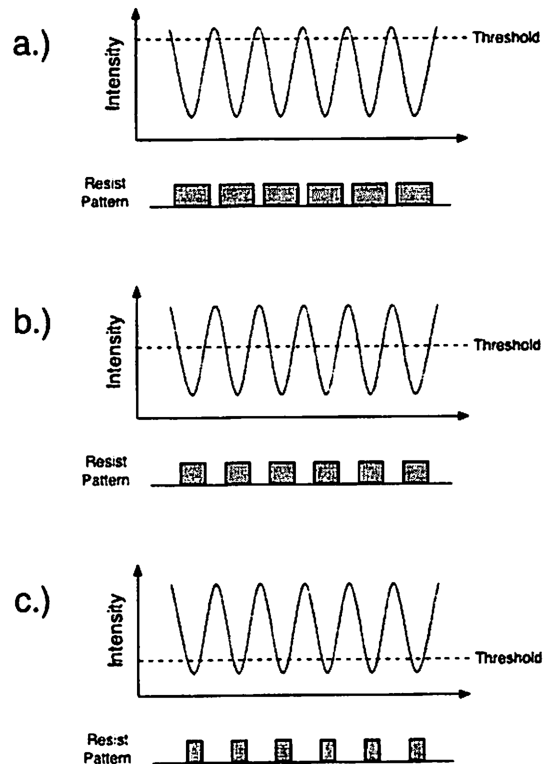

Figure 3.13: Principle of contrast measurement in photoresist. As the exposure dose is increased from a.) to c.), the developed linewidth shrinks.

3.3.1 Simulation of Contrast Transfer Function for the MET Optic

The expected CTF for an optical system can be obtained through simulation given the important system parameters, including information about the wavefront quality. The expected CTF for the MET system was simulated using the PROLITH software package

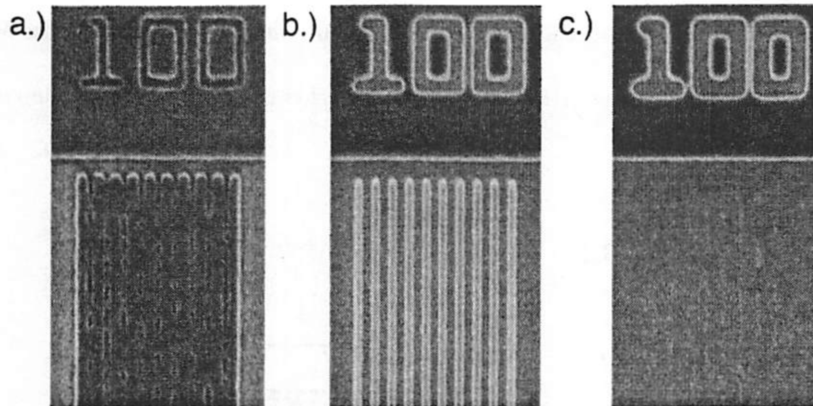

Figure 3.14: Resist images of 100 nm lines and spaces in EUV-2D resist showing contrast measurement technique. a.) Resist image at D_{max}, b.) resist image half way between D_{max} and D_{min}, c.) resist image at D_{min}.

[74]. In this case the lateral-shearing interferometry (LSI) measurements of the MET optic [67] were used to accurately model the impact of aberrations on the CTF. The wavefront data for the center of the field was used as this is where the measurements were performed. Annular illumination was used, with $\sigma_{inner} = 0.3$ and $\sigma_{outer} = 0.7$. The simulated CTF for vertical lines is shown in Figure 3.15 for both the ideal (unaberrated) and aberrated cases. The results show clearly that aberrations have a strong impact on the image contrast.

3.3.2 Darkfield Contrast Transfer Function

The CTF for the MET was first measured experimentally using a darkfield mask, meaning that the majority of the mask area is covered with an absorber layer. Three resists were used, Rohm and Haas EUV-2D, Rohm and Haas MET-1K (XP 3454C), and a derivative of KRS [75]. A resist thickness of 125 nm was used in each case. The PAB and PEB temperatures for EUV-2D and MET-1K were 130°C, while KRS does not require a

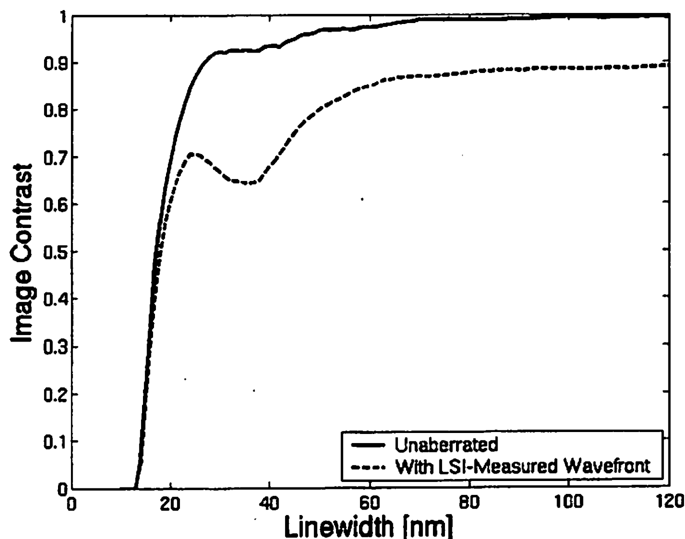

Figure 3.15: Simulated contrast transfer function for the MET under annular illumination with $\sigma_{inner} = 0.3$ and $\sigma_{outer} = 0.7$.

PEB step. Annular illumination was used, with $\sigma_{inner} = 0.3$, $\sigma_{outer} = 0.7$, and $\lambda = 13.5$ nm. The mask pattern contained vertical lines and spaces of equal size ranging from 20 nm to 120 nm.

Due to limited resist resolution and limited dose range in the focus-exposure matrices available on the test wafers, measurements throughout the full 20-120 nm range were not possible. The results of the measurements are shown in Figure 3.18. Clearly the measured contrast values are well below those predicted by the aerial image simulations. This is most likely due to limited resist resolution, an issue that will be discussed in Section 4.4. The CTF is also a useful method for comparing photoresist performance. The CTF measured with EUV-2D resist (Table 3.2, Figure 3.19), an older formulation, is below the CTF for both MET-1K (Table 3.3, Figure 3.20) and KRS (Table 3.4, Figure 3.21) resists,

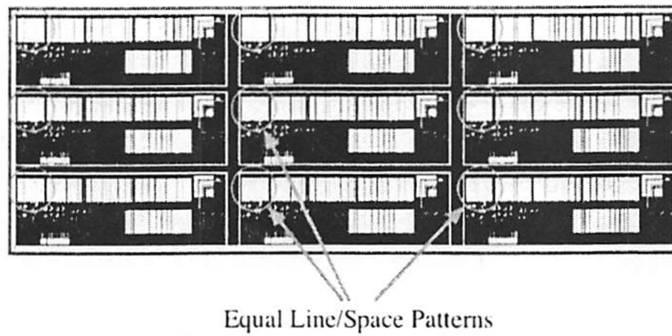

Figure 3.16: Mask pattern for darkfield contrast transfer function measurements. Circled areas indicate locations of equal line/space patterns used for measurements.

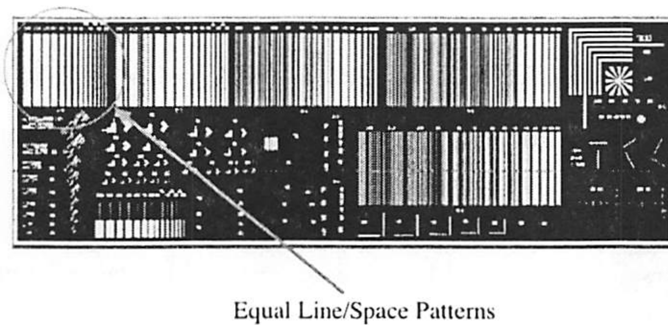

Figure 3.17: Cell view of mask pattern for darkfield contrast transfer function measurements, repeated nine times within the field (three columns × three rows). Circled area indicates location of equal line/space patterns used for measurements.

which have been shown to have superior resolution to EUV-2D.

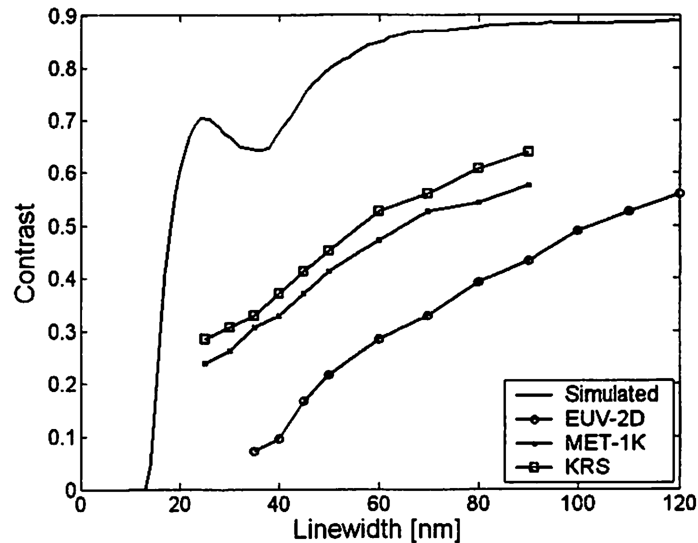

Figure 3.18: Measured darkfield contrast transfer function for the MET using a variety of photoresists.

3.3.3 Brightfield Contrast Transfer Function

The CTF was also measured using a brightfield mask with identical patterns to the darkfield mask, but with the multilayer coatings exposed over the majority of the mask area. The results for both brightfield and darkfield measurements using Rohm and Haas MET-1K resist are shown in Figure 3.22. The contrast data for the brightfield CTF in MET-1K resist is given in Table 3.5 and Figure 3.23.

Although there is some difference between the two curves, the difference is relatively small. The likely reason for this is that in EUV optical systems such as the MET much of the flare is short-range and therefore highly dependent upon local pattern density.

Table 3.2: Darkfield contrast data for Rohm and Haas EUV-2D resist. D_0 is the dose-to-clear.

Feature Size [nm]	D_{min}/D_0	D_{max}/D_0	Contrast
35	2.527	2.925	0.073
40	2.406	2.925	0.097
45	2.183	3.071	0.169
50	2.079	3.225	0.216
60	1.796	3.225	0.285
70	1.629	3.225	0.329
80	1.551	3.556	0.392
90	1.477	3.733	0.433
100	1.407	4.116	0.490
110	1.340	4.322	0.527
120	1.340	4.765	0.561

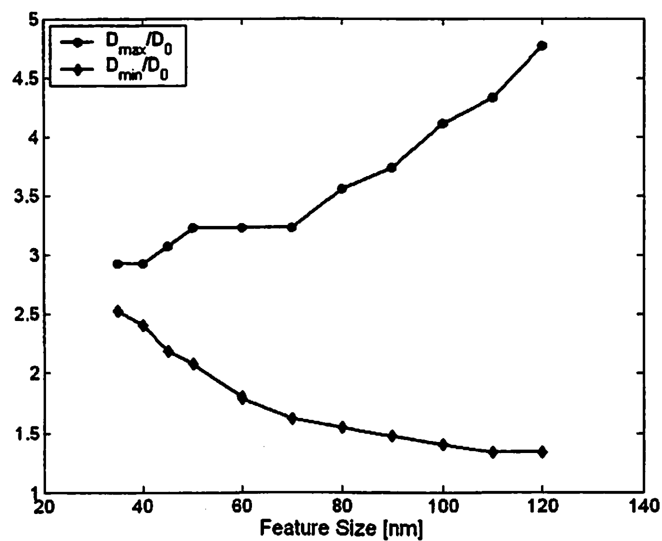

Figure 3.19: Behavior of D_{max}/D_0 and D_{min}/D_0 as a function of feature size for EUV-2D resist with a darkfield mask pattern. D_0 is the dose-to-clear.

Table 3.3: Darkfield contrast data for Rohm and Haas MET-1K (XP 3454C) resist. D_0 is the dose-to-clear.

Feature Size [nm]	D_{min}/D_0	D_{max}/D_0	Contrast
25	2.292	3.734	0.239
30	2.079	3.734	0.285
35	1.886	3.556	0.307
40	1.710	3.387	0.329
45	1.551	3.387	0.372
50	1.407	3.387	0.413
60	1.216	3.387	0.472
70	1.103	3.556	0.527
80	1.103	3.734	0.544
90	1.103	4.116	0.577

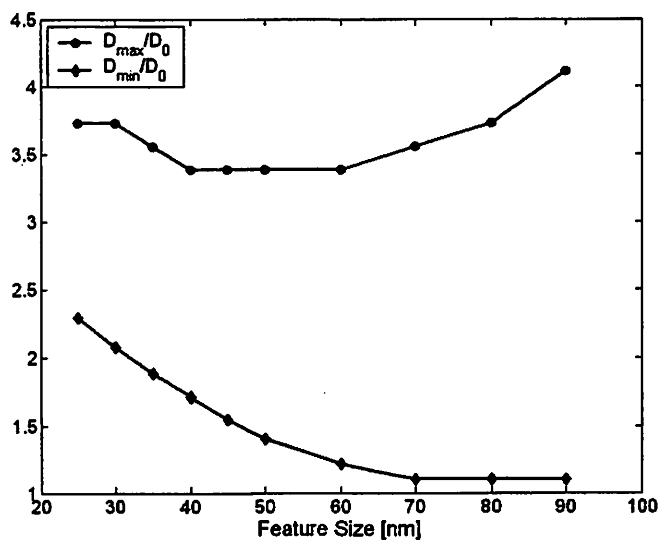

Figure 3.20: Behavior of D_{max}/D_0 and D_{min}/D_0 as a function of feature size for MET-1K resist with a darkfield mask pattern. D_0 is the dose-to-clear.

Table 3.4: Darkfield contrast data for KRS resist. D_0 is the dose-to-clear.

Feature Size [nm]	D_{min}/D_0	D_{max}/D_0	Contrast
25	2.292	4.116	0.285
30	2.079	3.920	0.307
35	1.886	3.734	0.329
40	1.710	3.734	0.372
45	1.551	3.734	0.413
50	1.477	3.920	0.453
60	1.340	4.322	0.527
70	1.276	4.538	0.561
80	1.216	5.003	0.609
90	1.216	5.516	0.639

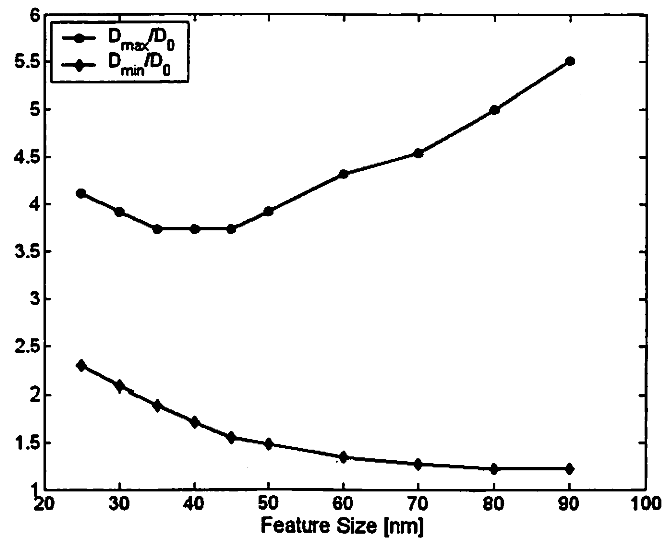

Figure 3.21: Behavior of D_{max}/D_0 and D_{min}/D_0 as a function of feature size for KRS resist with a darkfield mask pattern. D_0 is the dose-to-clear.

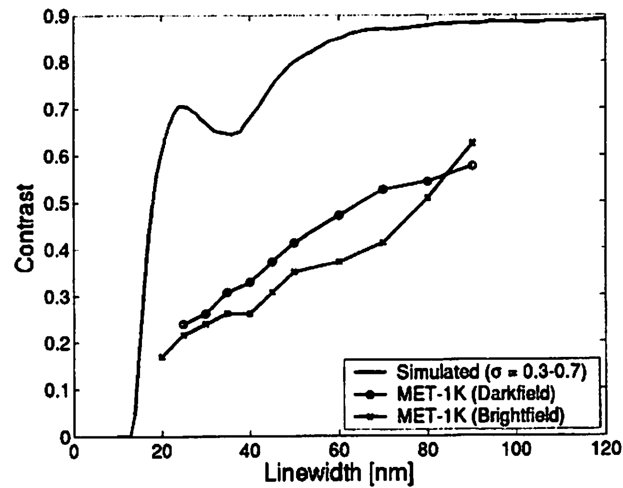

Figure 3.22: Comparison of contrast transfer function for brightfield and darkfield cases using Rohm and Haas MET-1K. D_0 is the dose-to-clear.

Table 3.5: Brightfield contrast data for Rohm and Haas MET-1K (XP 3454C) resist.

Feature Size [nm]	D_{min}/D_0	D_{max}/D_0	Contrast
20	2.292	3.225	0.169
25	1.886	2.925	0.216
30	1.796	2.925	0.239
35	1.710	2.925	0.262
40	1.629	2.786	0.262
45	1.478	2.786	0.307
50	1.407	2.925	0.350
60	1.340	2.925	0.372
70	1.276	3.072	0.413
80	1.276	3.920	0.509
90	1.216	5.254	0.624

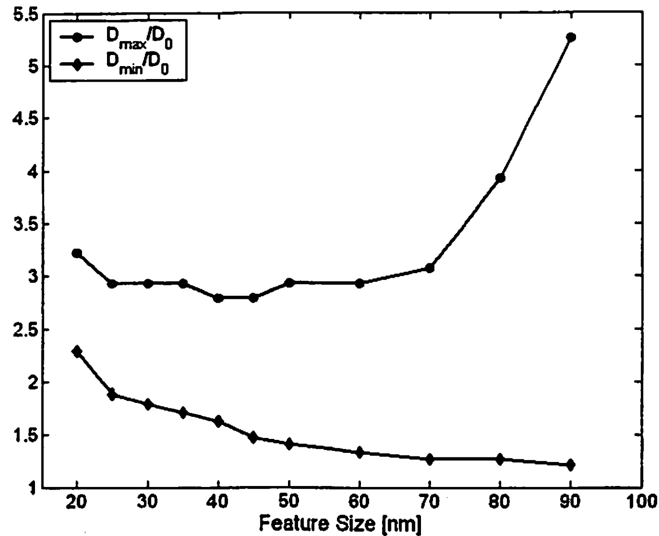

Figure 3.23: Behavior of D_{max}/D_0 and D_{min}/D_0 as a function of feature size for MET-1K resist with a brightfield mask pattern. D_0 is the dose-to-clear.

Examination of the test patterns used to measure the CTF (shown in Figure 3.17) shows that the line and space patterns are grouped closely together, meaning there is little empty area around the line groups. Therefore, there will be only slight differences in local pattern density between the brightfield and darkfield cases, and the primary difference between them will come from long-range flare.

3.3.4 Orientation Dependence of Contrast Transfer Function

One possible explanation for the large difference between the simulated and experimental results in Figures 3.18 and 3.22 is that a large amount of aberration was introduced into the system between the time when the interferometric wavefront measurement (used in the simulations) was done and when the wafers were exposed. In order to investigate this

possibility, the CTF was measured for four different orientations: −45°, 0°, 45°, and 90°. If any non-rotationally symmetric aberrations are present in a significant amount, the CTF for the different orientations should show significant variation.

The experiment was conducted using Rohm and Haas MET-1K (XP 3454C) resist. Annular illumination was used with $\sigma_{inner} = 0.3$ and $\sigma_{outer} = 0.7$. The results of the experiment are shown in Figure 3.24.

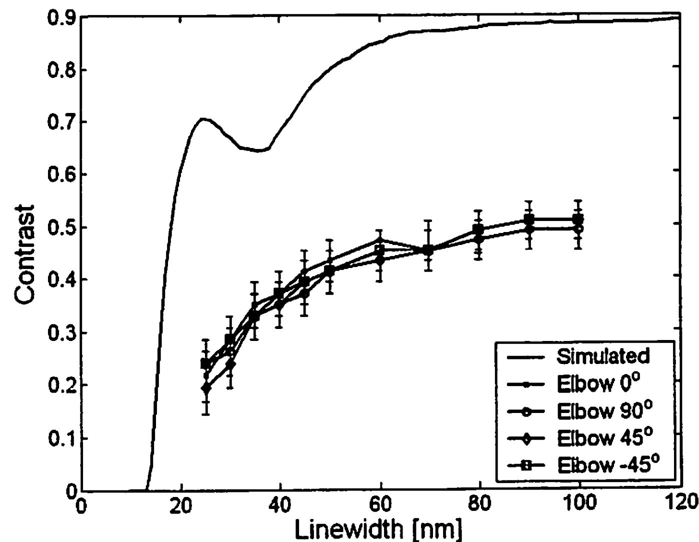

Figure 3.24: CTF for four different feature orientations in Rohm and Haas MET-1K resist. The error bars represent the uncertainty due to finite exposure dose step size in the focus-exposure matrix used in the experiment.

The error bars in Figure 3.24 represent the uncertainty due to finite exposure dose step size in the focus-exposure matrix used in the experiment. The fact that there is little variation seen (no variation outside the error bars) between the CTF curves for the four orientations shown in Figure 3.24 is evidence that at least non-rotationally symmetric aberrations do not play a significant role in the measured CTF. This indicates that some

other factors may be at work. These issues will be discussed in more detail in Chapter 4.

3.4 Resist-Based Measurement of Optical Aberrations

3.4.1 Focal Plane Tilt

In order to ensure optimal performance across the field, the wafer must be properly positioned in the focal plane of the projection optics. If this is not the case, the best focus position will vary across the field so that some parts of the field will see better image quality than others, leading to unwanted CD variation. In order to characterize the focal plane tilt in the MET system, a large focus-exposure matrix (FEM) was printed on a test wafer. Scanning electron microscopy (SEM) was then used to study the image quality of 50 nm equal line and space patterns through focus. No gold coating was used for the resist samples. The measurements were collected at nine points across the field. The metric used for image quality was line edge roughness (LER). It has been shown that LER is a function of aerial image contrast [76]. As any departure from best focus will decrease the image contrast, the LER will show a minimum at best focus. The LER measurements were performed using the SuMMIT software package [77] with default settings. The resulting LER plots for each point in the field are shown in Figure 3.25.

Note that the LER curves for each field position do not all have the same minimum. This indicates that the focal plane is tilted. Using the focal position at which each field point showed the minimum LER, a contour map of best focus can be determined. This is shown in Figure 3.26. Here the focus values are relative to the best focus for the center of the field. Note that there is significant tilt evident in the focal plane. This was determined

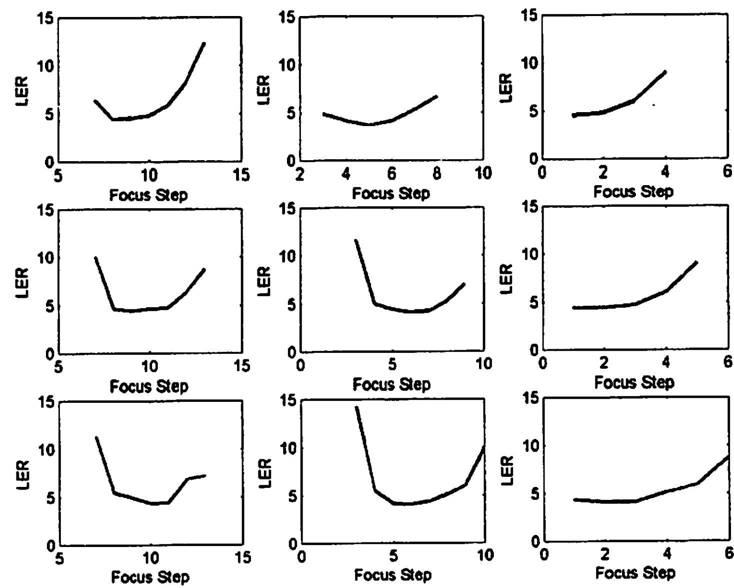

Figure 3.25: Line edge roughness (LER) measurements through focus at nine different points within the field. Minimum LER at each point represents the best focus at that position.

to be due to a slight tilt in the mask stage, which was corrected to improve across-field focus uniformity.

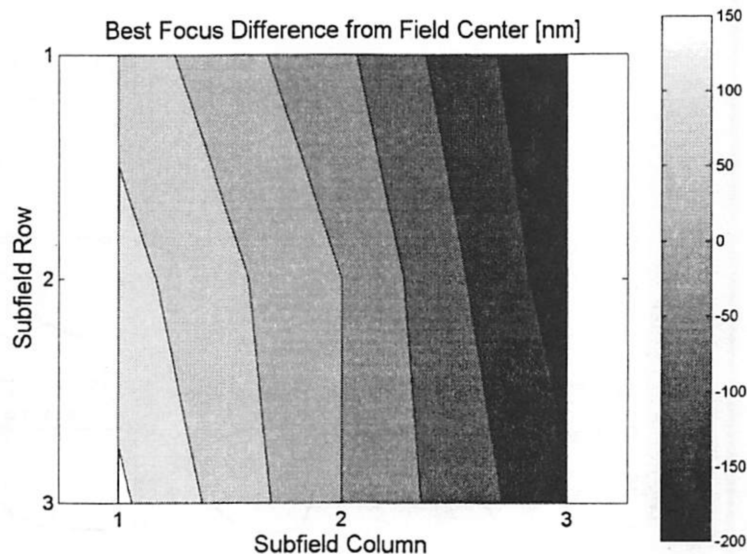

Figure 3.26: Contour map of best focus across the field relative to the best focus at the center of the field.

3.4.2 Astigmatism

The effect of astigmatism on imaging performance is an orientation-dependent focus shift [78]. For example, for primary astigmatism (Z_5), the best focus position will be different for vertical and horizontal features. Therefore, the astigmatism can be measured using a technique similar to that discussed in Section 3.4.1. The best focus is determined for vertical and horizontal features for primary astigmatism (Z_5), and for 45° and $-45°$ features for 45°-astigmatism (Z_6) using "elbow" patterns as shown in Figure 3.27.. In this case CD was measured through focus, with the minimum CD corresponding to best focus.

Note that care must be taken not to operate at the iso-focal dose for this technique to be successful. Lithography modeling software may then be used to determine the amount of astigmatism which will produce the observed focus shift between feature orientations.

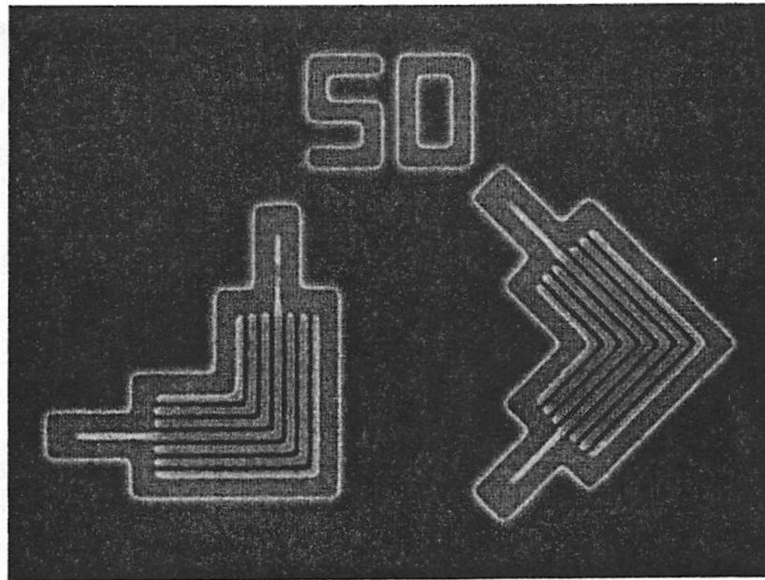

Figure 3.27: 50 nm elbow patterns in Rohm and Haas MET-1K (XP 3454C) used for measuring astigmatism.

In order to extract the astigmatism in the MET, a focus-exposure matrix (FEM) wafer was exposed with fine (40 nm) focus steps. Rohm and Haas MET-1K (XP 3454C) resist was used along with annular illumination ($\sigma_{inner} = 0.3$, $\sigma_{outer} = 0.7$). High-resolution SEM images were captured of 50 nm lines in each of the relevant orientations ($-45°$, $0°$, $45°$, and $90°$), and the CD was measured using the SuMMIT software package [77]. This data was plotted, and a second-order polynomial was fit to the data for each feature orientation. The focal position corresponding to the minimum of the polynomial was taken to be the best focus position for that feature type. Simulations with lithography modeling software

showed that the focus offset between orthogonal feature orientations has a linear dependence on astigmatism with a slope of 60 nm focus offset per 0.5 nm RMS astigmatism.

The primary astigmatism and 45° astigmatism were measured for a single point in the MET field. The results for primary astigmatism are shown in Figures 3.28 and 3.29 and Table 3.6, while the 45° astigmatism results are shown in Figures 3.30 and 3.31 and Table 3.7. In addition, the total astigmatism ($\sqrt{Z_5^2 + Z_6^2}$) is shown in Figure 3.32 and Table 3.8.

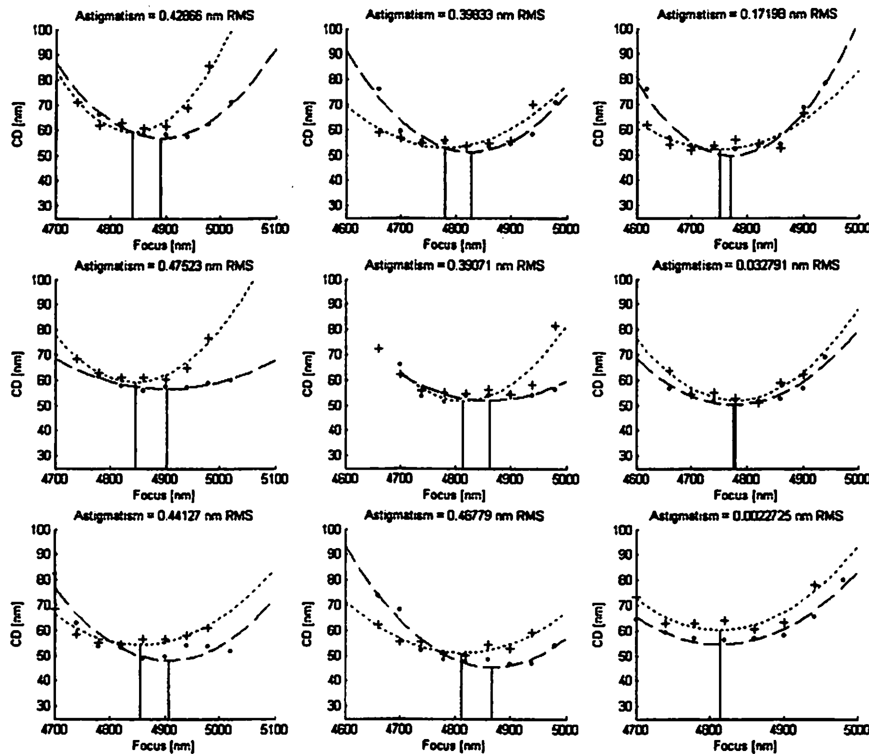

Figure 3.28: Extraction of astigmatism in the MET through focus offset between vertical (0°) and horizontal (90°) features. Plots are arranged in the same order as the corresponding field locations.

In general the total astigmatism measured in this experiment agrees with the

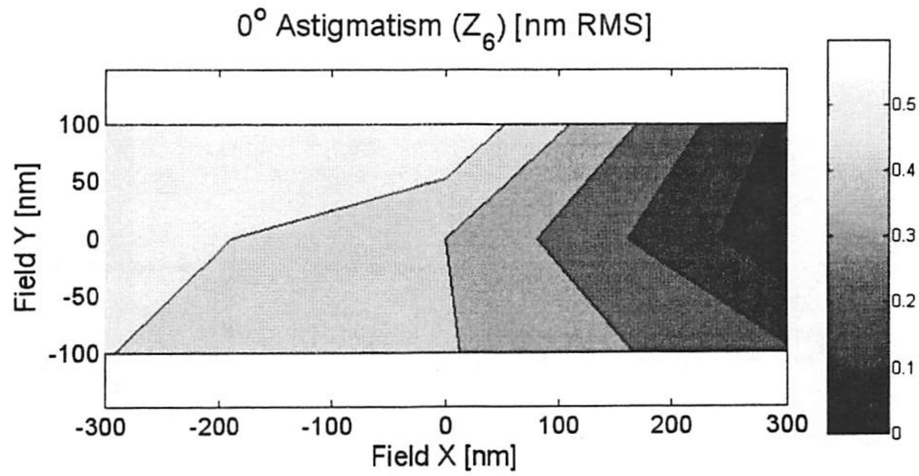

Figure 3.29: Contour map of 0° astigmatism (Z_6) in the MET optic.

Table 3.6: Extracted 0° astigmatism (Z_6, in [nm] RMS) by field location.

0.43 nm	0.40 nm	0.17 nm
0.48 nm	0.39 nm	0.03 nm
0.44 nm	0.47 nm	0.00 nm

Table 3.7: Extracted 45° astigmatism (Z_5, in [nm] RMS) by field location.

0.00 nm	0.22 nm	0.29 nm
0.03 nm	0.07 nm	0.20 nm
0.03 nm	0.08 nm	0.15 nm

Table 3.8: Extracted total astigmatism ($\sqrt{Z_5^2 + Z_6^2}$, in [nm] RMS) by field location.

0.43 nm	0.45 nm	0.34 nm
0.48 nm	0.40 nm	0.20 nm
0.44 nm	0.47 nm	0.15 nm

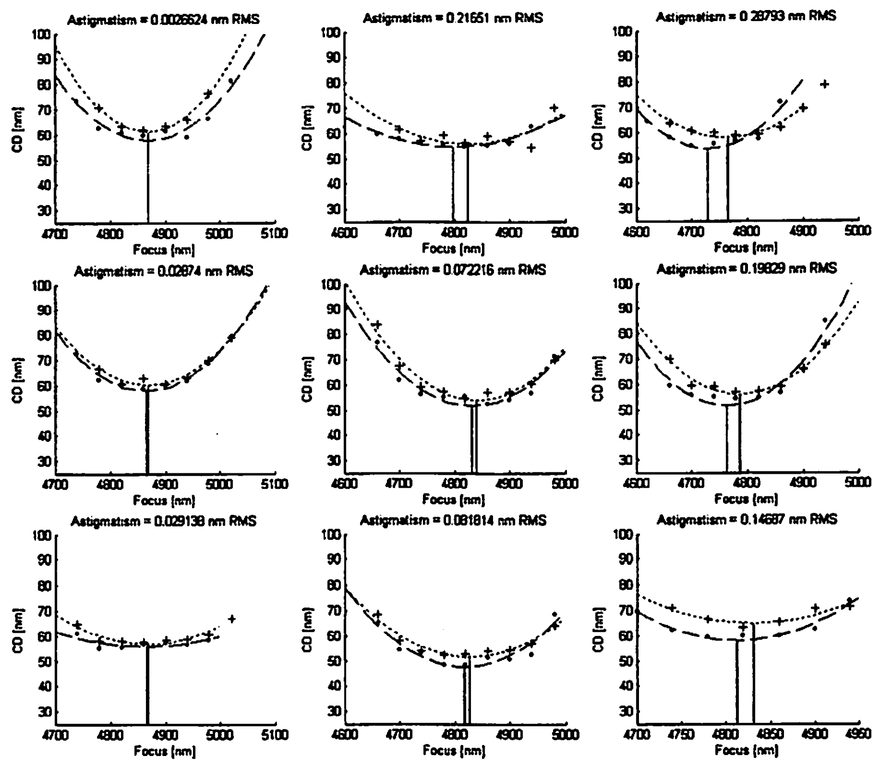

Figure 3.30: Extraction of 45° astigmatism in the MET through focus offset between 45° and −45° features. Plots are arranged in the same order as the corresponding field locations.

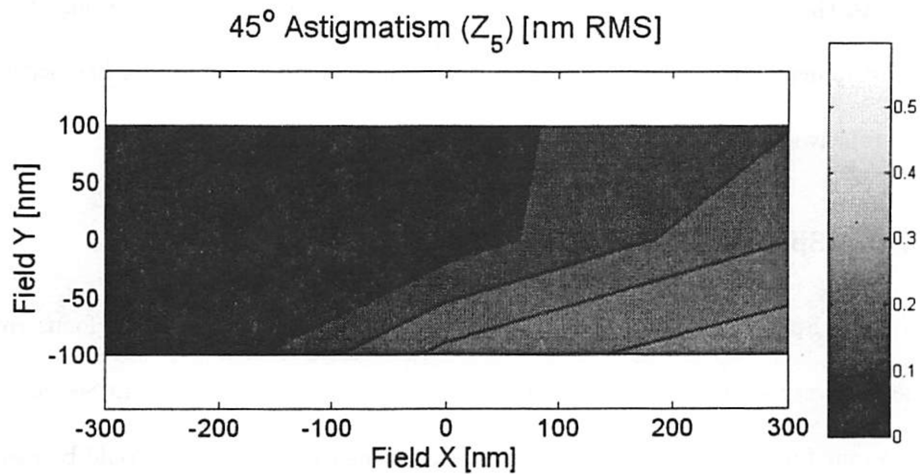

Figure 3.31: Contour map of 45° astigmatism (Z_5) in the MET optic.

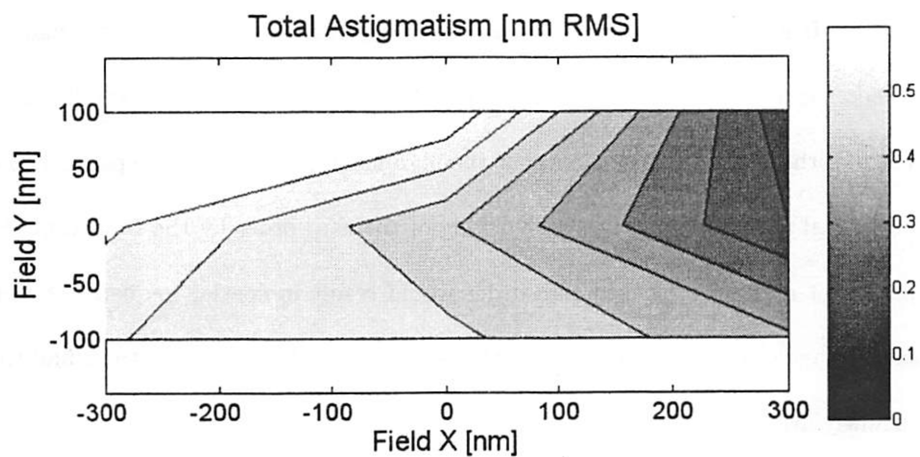

Figure 3.32: Contour map of total astigmatism ($\sqrt{Z_5^2 + Z_6^2}$) in the MET optic.

interferometrically-measured astigmatism, except for the column in the center of the field. Due to the fact that the optic exhibited significant aberration drift during interferometry measurements, it seems quite possible that a slight drift in alignment has occurred during the relatively long time interval between the two measurements.

3.4.3 Spherical Aberration

Spherical aberration results in a spatial frequency-dependent focus shift [78]. A method very similar to the method used for measuring astigmatism in Section 3.4.2 could be applied to measure spherical aberration. In this case, best focus would be measured as a function of pitch rather than orientation. Lithography modeling software may then be used to determine the magnitude of focus shift expected as a function of pitch for varying levels of spherical aberration, and the results of the modeling may be compared with experimental results to determine the amount of spherical aberration.

It is important in this case to use highly coherent illumination (small σ) in order to keep the area of the pupil which is "sampled" by diffracted orders small. The particular design of the MET optic requires that the illumination should also be positioned away from the optical axis in order to avoid blocking of the zero order by the central obscuration. If this is not done, the blocked zero order would result in spatial frequency-doubling in the aerial image (see Section 3.5.1), and the resulting pattern would be too small to resolve in currently available photoresists.

3.4.4 Coma

The effect of coma on the aerial image is to produce asymmetry and spatial frequency-dependent lateral shift [78]. The asymmetry may be used to measure coma by observing asymmetries in resist patterns which should ideally be symmetric. For example, a line and space pattern should ideally be symmetric in terms of linewidth. However, in the presence of coma (of the proper orientation with respect to the lines), lines on one side of the pattern may show an increase in resist linewidth relative to the other lines. This may be used along with lithography modeling software to determine the amount of coma which will produce the observed difference in linewidth.

Unfortunately, the pattern sizes required to cause a measurable change in linewidth are on the order of 20 nm, and are therefore too small to resolve with currently available resists.

3.5 Interferometric Method of Aberrometry for Obscurated Optical Systems

Given the fact that aberrations in lithography tools such as the MET system can drift over time [68], it would be highly desirable to have a method for monitoring such drift. In this section a novel method for measuring lens aberrations is proposed which takes advantage of the central obscuration in the MET optic to create two-wave interference at the wafer.

3.5.1 Method

This method uses line/space patterns and highly coherent illumination ($\sigma \simeq 0.05$) to create diffracted orders which "sample" the wavefront of the projection optics. The zero order is entirely blocked by the central obscuration, and the pitch is chosen so that the first orders pass through the lens at a specified radius within the pupil. These two waves will then interfere at the wafer plane to create the aerial image which is then transferred into photoresist. If aberrations are present in the lens, then an optical path difference (OPD) will exist between the two waves. As shown in Figure 3.33, this may be thought of as causing a "tilt" in the wavefront. This tilt will result in a lateral shift of the aerial image at the wafer. By measuring the lateral shift as a function of pitch (and therefore a function of pupil position), the "signature" of a particular set of aberrations may be recorded. Changes in this signature over time indicate a drift in the aberrations present in the system.

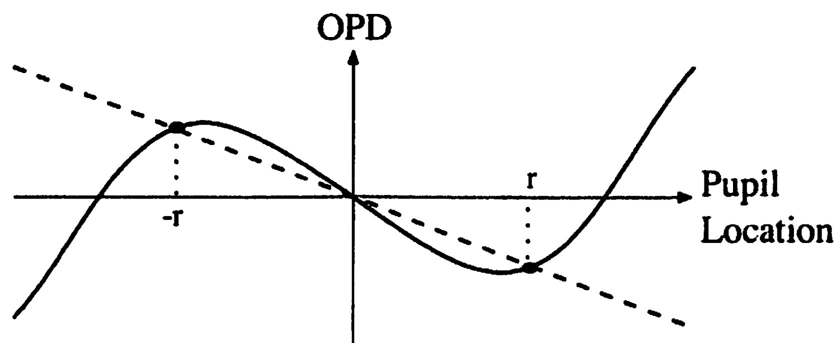

Figure 3.33: The interference of two waves with a non-zero optical path difference (OPD) may be interpreted as a tilted wavefront, resulting in a lateral shift of the aerial image at the wafer.

The blocking of the zero order in this method has one important consequence: the aerial image becomes frequency-doubled relative to the mask pattern. The process by

which this occurs is illustrated in Figure 3.34. The aerial image electric field and intensity for the case with no central obscuration are shown In Figure 3.34a.) and b.), respectively. Here the aerial image intensity, I, is given by

$$I = E^{*}E, \tag{3.23}$$

where E is the aerial image electric field. The aerial image electric field and intensity for the case with the central obscuration are shown in Figure 3.34c.) and d.), respectively.

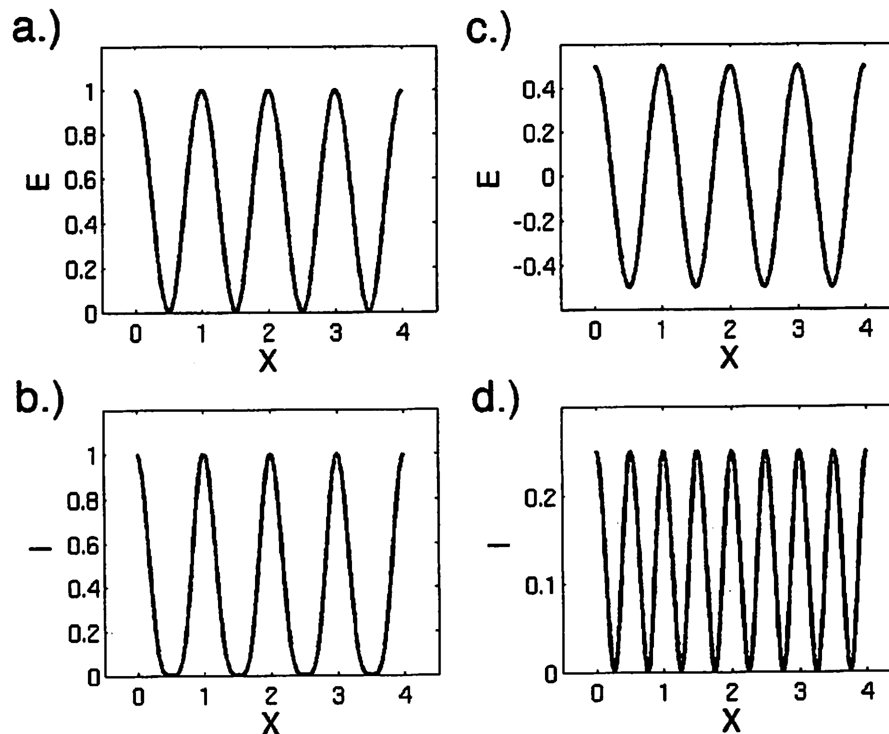

Figure 3.34: Illustration of frequency doubling with central obscuration. a.) Aerial image electric field with no central obscuration, b.) aerial image intensity with no central obscuration, c.) aerial image electric field with central obscuration blocking zero order, d.) aerial image intensity with central obscuration blocking zero order.

Table 3.9: Expected pattern shifts for the base wavefront of the MET system (shown in Figure 3.3).

r_{pupil}	P_{mask}	Pattern Shift
0.35	129 nm	-6.8 nm
0.45	100 nm	-5.3 nm
0.55	82 nm	-4.5 nm
0.65	69 nm	-3.2 nm
0.75	60 nm	-2.0 nm
0.85	53 nm	0.8 nm
0.95	47.4 nm	3.2 nm

The amount of lateral shift expected in the aerial image for a given OPD may be deduced by noting that the difference in phase between the two waves interfering at the wafer goes from 0° to 180° (one half-wave) over a lateral distance of $P_{wafer}/2$, where P_{wafer} is the pitch of the aerial image at the wafer. Due to the frequency doubling which occurs when the zero order is blocked, $P_{wafer} = P_{mask}/2$. Therefore, the amount of lateral shift Δx which will occur for an OPD $\Delta\phi$ in waves as a function of normalized pupil radius r_{pupil} is given by

$$\Delta x(r_{pupil}) = \Delta\phi \cdot P_{mask}/2. \qquad (3.24)$$

3.5.2 Practical Implementation Considerations

Although this method is viable in principle, there are several practical considerations which make it challenging to implement. The first is the requirement for structures whose position is insensitive to the aberrations present in the optical system. These structures serve as a reference with which to measure the lateral shift of the line and space

patterns. One possible reference structure is an array of 100 nm $\times$ 100 nm squares. However, due to the fact that these structures contain a relatively large amount of low-spatial frequency information which is blocked by the central obscuration in the pupil, only the corners of the square (the locations with the highest spatial frequency content) are likely to show up in the aerial image. In addition, because most of the energy from the square patterns is in lower diffraction orders which are blocked, the effective dose at the wafer for the square patterns is much lower than the dose for the line and space patterns. One possible solution to this problem is to target the exposure dose in order to print the square corners, which will result in overexposure of the line and space patterns. However, as only the lateral position of the line and space patterns is important, it is not necessary to resolve individual lines, and the overexposure will not pose a problem.

A second challenge is the development of image processing software to perform the actual measurements. Because the relative position measurements required by this technique are not supported in commercial SEM software, this would most likely be implemented as an offline software package. The software would need the capability to read a SEM image, locate both the reference structures and line and space patterns, find the center of each, and measure the relative position shifts.

One additional practical consideration is the alignment of the illumination within the pupil. For measuring odd aberrations, it is desirable to have a small illumination size at the center of the pupil. However, due to the central obscuration, this illumination pattern cannot be seen by the illumination pupil fill monitor in the MET. Therefore, it is difficult to ensure that the illumination is properly centered. This is critical because any

position deviation from the pupil center will result in lateral shifts in the line and space patterns, which may be erroneously interpreted as the result of aberrations. In addition, the measurement of even aberrations requires a small illumination size at a specific off-axis location in the pupil. Again, the position of the line and space patterns at the wafer is highly sensitive to the placement of the illumination within the pupil. Achieving the required precision in illumination placement is therefore critical.

Finally, for other commercial EUV lithography systems which use a similar optic but different illuminators [79], achieving the required level of partial coherence may be problematic. In the MET system at LBNL, the use of synchrotron radiation as a source provides a high degree of coherence. However, this may be more difficult to achieve in systems which use Xe gas discharge plasmas, for example.

Each of these challenges must be addressed in order for this technique to be viable. However, if they can be met successfully, this method may provide a relatively quick way of monitoring aberration drift over time.

Chapter 4

Characterization of EUV Photoresists

One of the key challenges in EUV lithography is the development of suitable photoresists. These resist much meet strict requirements in terms of resolution, sensitivity, line-edge roughness (LER), among others.

4.1 Resist Overview

A photoresist is simply a chemical which can be applied to the surface of a silicon wafer as a thin film. A photoresist is sensitive to photons such that it undergoes a change in solubility when exposed to light. In addition, it should be at least somewhat resistant to the etching process which will be used to transfer the pattern into the underlying thin film layers to form useful device structures. The photoresist is a sacrificial layer, and is removed after the pattern is transferred.

4.1.1 Types of Photoresists

Two types of photoresists exist: positive and negative resists. Positive resists undergo an increase in solubility when exposed to light through a process called deprotection. Negative resists undergo a decrease in solubility when exposed to light through a process called crosslinking. Positive resists are the most commonly used in industry, and will be the focus of work performed here. In addition, most resists currently in production use fall into the category of chemically-amplified resists [80, 81, 82]. The chemical amplification process is critical in achieving the high-throughput required for volume manufacturing. This process is based upon a chain-reaction property of the deprotection reaction. When a chemically-amplified resist is exposed to light, photoacids are generated. Then during the post-exposure bake process, these photoacids attack the resist polymers, causing deprotection (and therefore increased solubility) and also generating another acid as a side effect. This acid may then deprotect another resist polymer, which generates another acid, and so on. In this way a single photoacid generated by the exposure process may cause the deprotection of 100 resist polymers or more.

4.1.2 Photoresist Process Flow

The process of patterning a wafer using photoresist involves many steps. Depending on the particular process being used, the wafer may first be coated with an adhesion-promoter such as hexamethyldisilazane (HMDS) to prevent the final resist lines from falling over or lifting off of the wafer. In addition, an anti-reflective coating (ARC) may be used to help minimize standing waves in the photoresist. These coatings may be organic or

inorganic.

After these layers are applied, if necessary, the wafer is coated with photoresist. This is most often accomplished by dispensing the photoresist in liquid form onto the surface of the resist, then spinning the wafer rapidly to even out the resist film thickness. The final film thickness is controlled by modifying the spin speed and duration. After the wafer is coated with photoresist, a post-application bake (PAB, also known as a soft bake) is performed to drive excess solvent out of the resist. The wafer is then ready to be exposed using a stepper or scanner.

After exposure, the a post-exposure bake (PEB) is performed to drive the chemical amplification process and complete the deprotection reactions. The wafer is then exposed to a liquid developer which selectively removes the less soluble regions of the photoresist. At this point, the mask pattern has been transferred into the photoresist. Wet or dry etch processes may then be used to transfer the photoresist pattern into the underlying film stack. Finally, the remaining photoresist is removed, leaving behind only the patterned film stack.

4.2 CD Sensitivity to Post Exposure Bake Temperature Variations

Chemically-amplified photoresists depend strongly on the post-exposure bake step to drive the chemical chain reactions that lead to deprotection in the exposed areas. However, this also makes these resists sensitive to PEB temperature variations. Therefore, it is important the accurately characterize the critical dimension sensitivity to variations in the

PEB temperature.

In order to characterize the CD sensitivity to temperature variation, accurate temperature measurements of the PEB bake plate are required. This is accomplished using commercial temperature sensor wafers designed to mimic actual product wafers [83]. These sensor wafers have multiple temperature sensors spread across the wafer surface, and onboard electronics to record and transmit data.

A sample temperature trajectory measured with a sensor wafer is shown in Figure 4.1. This plot shows the measured temperature for all sensors on the wafer. Two regions of the temperatue trajectory are considered here, as labeled in Figure 4.1. Region 1 is the initial temperature transient as the wafer warms up from the ambient temperature to the bake temperature. Region 2 is the steady-state portion of the temperature trajectory. Typically CD sensitivity to PEB temperature is given in terms of steady-state temperature variation. However, recent work has suggested that the initial temperature transient is highly correlated with final resist CD. The two regimes are considered individually here.

4.2.1 Steady-State Temperature Variation

In order to observe the effect of steady-state temperature variation on resist CD, the target temperature of the PEB bake plate was changed in small increments, and the resulting effect on CD was observed. Rohm and Haas EUV-2D resist was used, with a nominal PEB temperature of 130°C and temperature increments of 2°C on either side of the nominal.

The temperature uniformity of the bake plate was measured using a temperature sensor wafer for each temperature set-point, and the results are shown in Figures 4.2–4.4

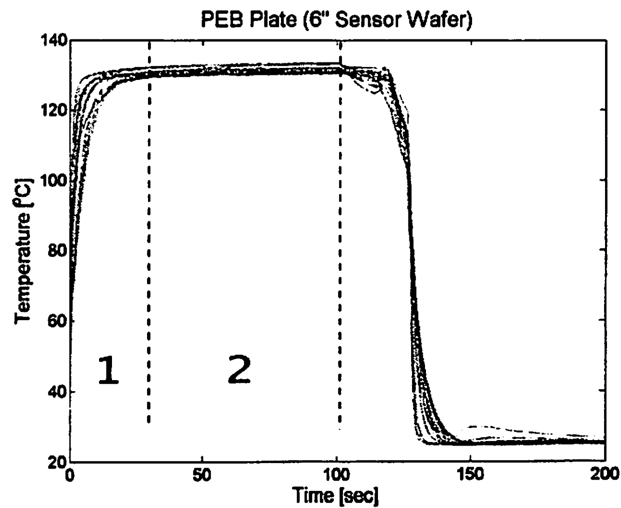

Figure 4.1: Sample PEB temperature trajectory. Region 1 indicates the initial temperature transient, region 2 indicates the steady state phase of the bake step.

after the wafer had reached its "steady-state" temperature near the end of the bake cycle. Clearly, the poor temperature uniformity of this bake plate would be unacceptable for use in a production environment. However, in this case the exposed area of the wafer is only approximately 1 cm^2, meaning that good temperature uniformity is not required across the entire 4" wafer.

Examination of the temperature uniformity data shows a similar signature for all three cases: a relatively uniform area near the center of the bake plate, then a rapid drop-off in temperature towards the edges. Therefore, care was taken in all PEB experiments to ensure that the exposed area of the wafer was placed at the center of the bake plate. In addition, the temperature data from the sensor in the center of the sensor wafer was used as the effective PEB temperature for data analysis. The temperature trajectory for the center sensor is shown for all three steady-state temperature settings in Figure 4.5. Note that

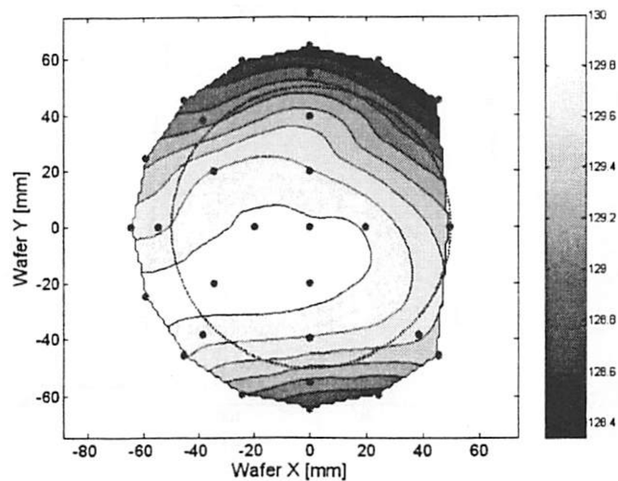

Figure 4.2: PEB temperature uniformity measured using temperature sensor wafer with bake plate center targeted for the baseline temperature of 130°C. The dotted outline represents the diameter of a 4" wafer, while the points show the temperature sensor locations.

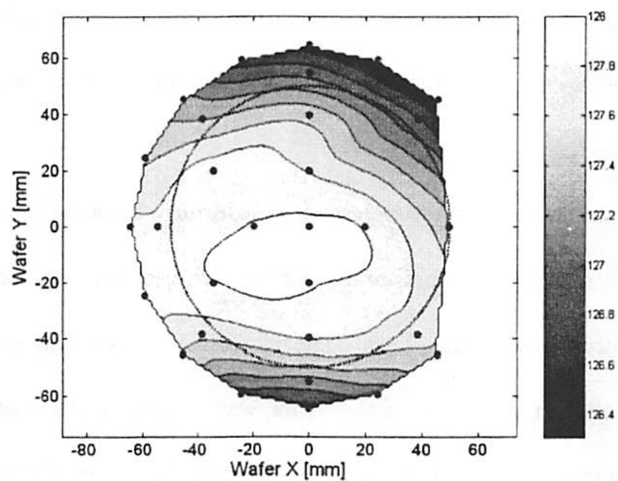

Figure 4.3: PEB temperature uniformity measured using temperature sensor wafer with bake plate center targeted for 128°C. The dotted outline represents the diameter of a 4" wafer, while the points show the temperature sensor locations.

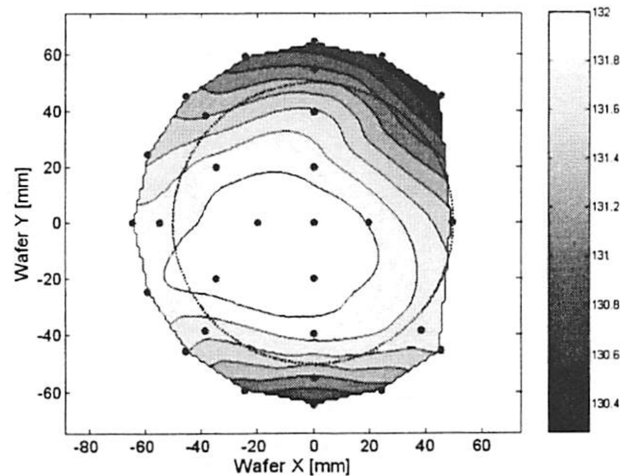

Figure 4.4: PEB temperature uniformity measured using temperature sensor wafer with bake plate center targeted for 132°C. The dotted outline represents the diameter of a 4" wafer, while the points show the temperature sensor locations.

the sensor wafer was set to begin data acquisition on a certain temperature change, and therefore some of the initial temperature ramp-up was not captured by this measurement. However, as the goal of this experiment is to determine the effect of steady-state PEB temperature on CD, this was not deemed important.

In order to measure the effect of the steady-state PEB temperature on critical dimension, focus-exposure matrix (FEM) wafers were exposed and baked at each of the different temperatures. Rohm and Haas EUV-2D resist was used with a post-application bake temperature of 130°C. The wafers were exposed using the darkfield resolution pattern shown in Figure 3.16 with annular illumination ($\sigma_{inner} = 0.3$, $\sigma_{outer} = 0.7$) and $\lambda = 13.5$ nm. The post-exposure bake step was performed immediately after exposure to minimize any environmental contamination effects. Each FEM took approximately 45 minutes to expose, which is long compared to the exposure time for a single field (less than one second).

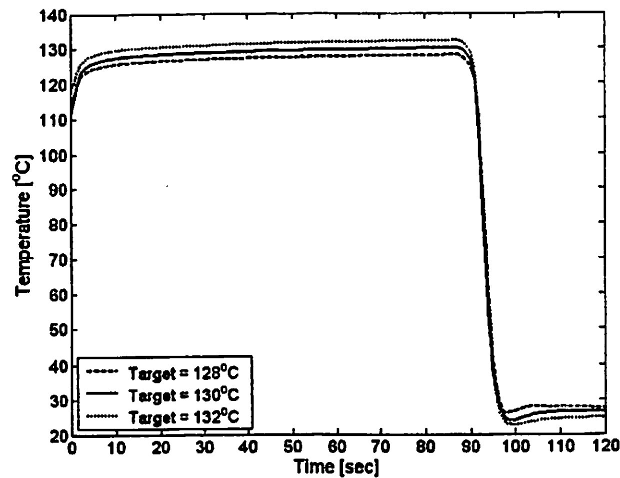

Figure 4.5: PEB temperature trajectories for steady-state CD sensitivity experiment measured using temperature sensor wafer.

However, because the wafer was under vacuum it is expected that contamination effects are unlikely. In addition, at the exposure temperature (27°C) little acid diffusion is expected and acid evaporation should be negligible.

The temperature data discussed previously was collected immediately before the PEB of the corresponding wafers in order to minimize the effect any potential temperature drift between the time of measurement and the actual PEB. Each row in the FEM was replicated three times, meaning that each focus-exposure combination had three instances on the wafer. The dose-to-size (E_{size}) for the relevant feature sizes was then determined for the baseline PEB temperature (130°C), and CD data collected for each replication at E_{size} and best focus. Next wafers were exposed at 128°C and 132°C using the same FEM recipe as the baseline wafer. In each case the CD was measured at the dose corresponding to E_{size} of the baseline wafer and best focus for each replication.

The CD data for 100 nm and 60 nm features is shown in Figures 4.6 and 4.7, respectively. In each case, a line is fit to the data using linear regression. The slope of the line gives a measure of the CD sensitivity to PEB temperature variation. In this case, the CD sensitivity is -1.46 nm/°C for 100 nm features and -1.82 nm/°C for 60 nm features. The CD variation seen within each temperature group is most likely due to random dose variation within the FEM. This is particularly problematic for smaller features, as they are more sensitive to dose variation.

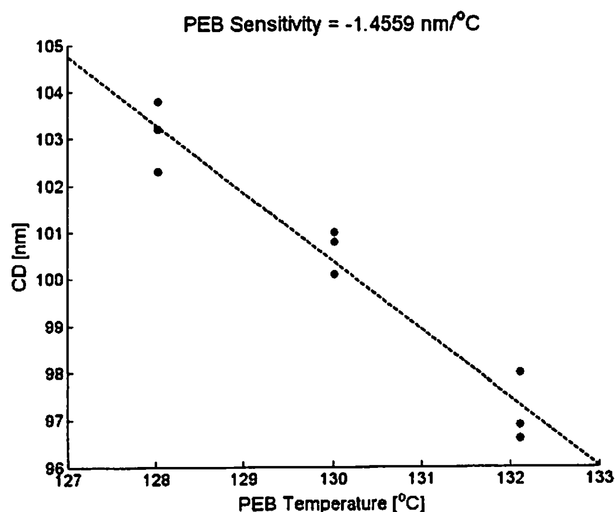

Figure 4.6: CD sensitivity to steady-state PEB temperature for 100 nm features.

4.2.2 Transient Temperature Variation

Modifying the temperature trajectory in the transient phase is more difficult than the steady-state. This is accomplished by inserting a thin film of Kapton polyimide film (0.005" thick) between the wafer and the bake plate. This has the effect of slowing the temperature "ramp-up" at the beginning of the PEB step. The effect on the Kapton film

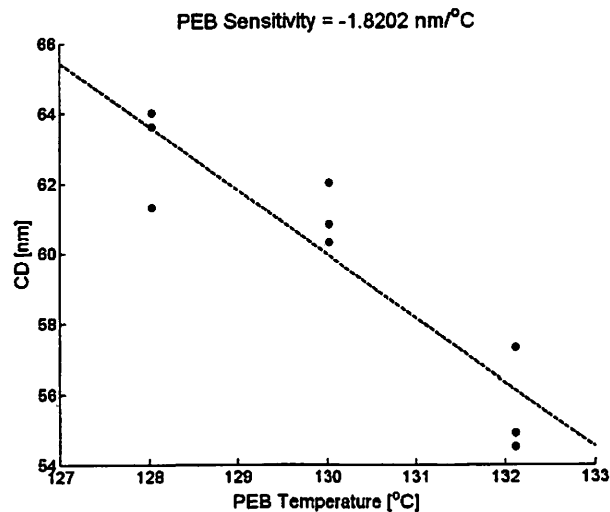

Figure 4.7: CD sensitivity to steady-state PEB temperature for 60 nm features.

on the initial temperature transient is shown in Figure 4.8. The ramp time (from 24°C to 110°C) without the Kapton film was 3.1 seconds, while the ramp time with the Kapton film was 30.5 seconds.

In order to determine the effect of the change in temperature ramp-up time on CD, wafers were coated with a 125 nm layer of Rohm and Haas MET-1K (XP 3454C) photoresist. The wafers were exposed using the darkfield resolution pattern shown in Figure 3.16 with annular illumination (σ_{inner} = 0.3, σ_{outer} = 0.7) and λ = 13.5 nm. The post-exposure bake step was performed immediately after exposure to minimize any environmental contamination effects. Post-application bake temperature was 120°C, while the nominal post-exposure bake temperature was 120°C. However, with the Kapton film in place the temperature sensor wafer recorded a temperature of only 118°C at the end of the PEB cycle, so the bake plate setpoint was adjusted between wafers to achieve a steady-state temperature of 118°C without the Kapton film for the control wafer.

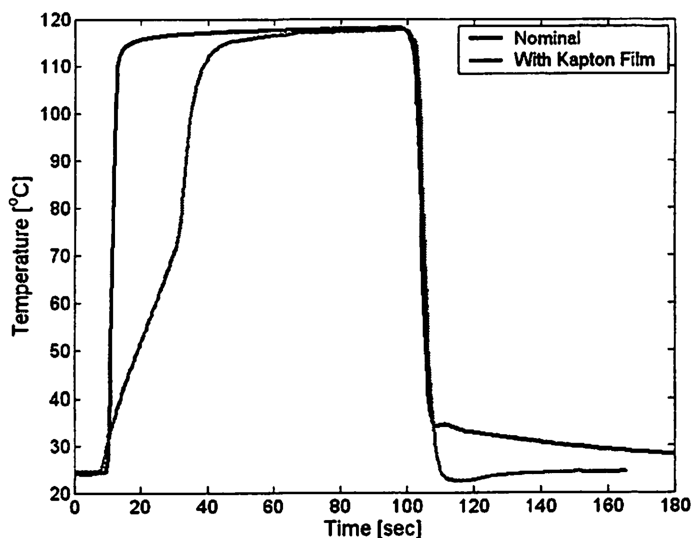

Figure 4.8: Post exposure bake temperature trajectories with and without 0.005" Kapton polyimide film between the wafer and the bake plate as measured with a commercial temperature sensor wafer.

Table 4.1: Effect of PEB temperature ramp time on CD for Rohm and Haas MET-1K (XP 3454C).

Nominal CD	CD (no Kapton)	CD (with Kapton)	Ramp Time Sensitivity
50 nm	48.6 nm	56.5 nm	0.29 nm/sec
60 nm	57.4 nm	63.9 nm	0.24 nm/sec
100 nm	89.0 nm	95.3 nm	0.23 nm/sec

The CD was then measured for three different feature sizes (50 nm, 60 nm, and 100 nm, equal lines and spaces) in the center of the field using a SEM (acceleration voltage of 2 kV) and the SuMMIT software package [77] with default parameters. The results are shown in Figure 4.9 and Table 4.1.

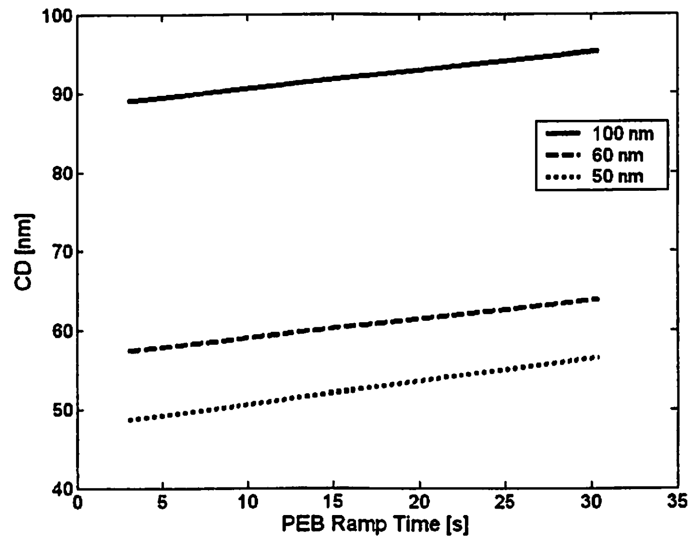

Figure 4.9: CD sensitivity to PEB temperature ramp time for Rohm and Haas MET-1K resist.

4.3 CD Sensitivity to PEB Time Variation

Variations in the duration of the PEB step can also affect the resulting critical dimension by changing the amount of time in which the chemical reactions responsible for changing the solubility of the exposed resist can occur. In order to characterize this effect for a sample EUV photoresist, an experiment was performed in which the PEB time was varied and the resulting CD measured.

The experimental setup was very similar to that described in Section 4.2.2. Wafers were coated with a 125 nm layer of Rohm and Haas MET-1K (XP 3454C) photoresist. The wafers were exposed using the darkfield resolution pattern shown in Figure 3.16 with annular illumination (σ_{inner} = 0.3, σ_{outer} = 0.7) and λ = 13.5 nm. The post-exposure bake step was performed immediately after exposure to minimize any environmental contamination

Table 4.2: Effect of PEB time on CD for Rohm and Haas MET-1K (XP 3454C).

Nominal CD	CD (PEB = 90s)	CD (PEB = 100s)	PEB Time Sensitivity
50 nm	52.6 nm	48.4 nm	0.42 nm/sec
60 nm	61.1 nm	56.9 nm	0.42 nm/sec
100 nm	90.5 nm	87.6 nm	0.29 nm/sec

effects. Post-application bake and post-exposure bake temperatures were both 120°C. One wafer was baked for the nominal PEB time of 90 seconds, while a second wafer was baked for 100 seconds.

The CD was then measured for three different feature sizes (50 nm, 60 nm, and 100 nm, equal lines and spaces) in the center of the field using a SEM (acceleration voltage of 2 kV) and the SuMMIT software package [77] with default parameters. The results are shown in Table 4.2.

4.4 Resist Modeling with Resist Point Spread Function

An accurate model of the photoresist response is extremely useful for process development, control, and other applications. These models are often complex systems of differential equations, making them fairly computationally intensive. A much simpler resist modeling technique using a resist point spread function [73] has been shown to have good agreement with experiments for certain EUV resists such as Shipley EUV-2D [84]. The resist point spread function is a two-dimensional function that, when convolved with the simulated aerial image for a given mask pattern and applied to a threshold function, gives a representation of the photoresist pattern remaining after development. This is summarized for positive resists in Equation 4.1:

$$I_{resist}(x,y) = \begin{cases} 1, & I_{aerial}(x,y) \otimes PSF_{resist}(x,y) < T \\ 0, & \text{otherwise} \end{cases} \tag{4.1}$$

where $I_{resist}(x,y)$ is the resist image intensity (binary), $I_{aerial}(x,y)$ is the aerial image intensity, $PSF_{resist}(x,y)$ is the resist point spread function (PSF), and T is the resist threshold. The same relationship holds for negative resists if the 'less than' symbol is changed to a 'greater than' symbol. Note that because a simple threshold approach is used to determine the resist image, only first-order effects such as feature size can be predicted using this model. Therefore, second-order effects such as sidewall angle or feature height cannot be predicted.

4.4.1 Extraction of Resist Point Spread Function

The resist point spread function may be extracted from the contrast transfer function (CTF) data discussed in Section 3.3. The first step in the procedure is to select the form for the point spread function. In this work a Gaussian function is used. Because the PSF is being fit to one-dimensional features (the equal-width lines and spaces used to measure CTF), it is only necessary to use a one-dimensional Gaussian of the form

$$PSF_{resist}(x) = \frac{1}{\sigma_{PSF}\sqrt{2\pi}} e^{-x^2/2\sigma_{PSF}^2}, \tag{4.2}$$

where σ_{PSF} is the standard deviation of the Gaussian function used for the resist PSF. Note that the full width at half maximum (FWHM) of the resist PSF is related to σ_{PSF} by

$$\text{FWHM} = 2\sqrt{2\ln 2}\sigma_{PSF}. \tag{4.3}$$

This is equivalent to measuring a cross-section of the PSF in the direction perpendicular to the lines and spaces. In this case, the PSF is assumed to be rotationally symmetric. However, by measuring the CTF for lines of different orientations and fitting the data individually, the two-dimensional PSF may be reconstructed.

In order to extract the resist PSF for a given resist, the measured CTF and the simulated CTF (including effects of optical aberrations) are required. In order to account for any constant "DC offset" between the measured and simulated CTF, a variable parameter , F_{DC}, is subtracted from each point in the simulated MTF curve before the convolution step. The F_{DC} term may be considered another model parameter which may be varied to obtain the best fit. For each feature size (or spatial frequency) in the measured data, a sinusoid of appropriate pitch is generated with a contrast matching the corresponding simulated value. The sinusoid is then convolved with the chosen resist PSF function, and the contrast of the result is compared with the measured value. The parameters of the resist PSF may be varied in order to find the values which best fit the measured data. In the case of a one-dimensional Gaussian resist PSF, the σ_{PSF} (or, equivalently, the FWHM) is varied. The best fit is determined to be the value of the FWHM which minimizes the sum of squared errors (SSE) between the fitted curve and the measured data.

4.4.2 Gaussian Resist Point Spread Function

Rohm and Haas EUV-2D

The results of the resist PSF extraction with DC offset term for Rohm and Haas EUV-2D are shown in Figure 4.10. The best fit was a Gaussian FWHM of 53 nm, very close to the value of 50 nm previously reported for this resist by Naulleau [84], with a DC offset value of 0.26. The fit quality is also greatly improved.

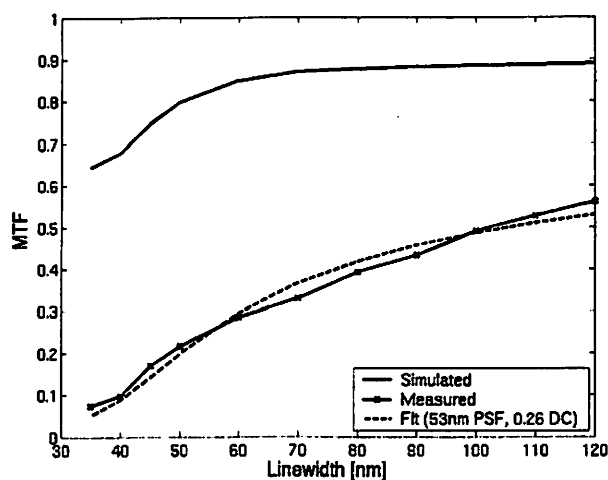

Figure 4.10: Extraction of resist point spread function with DC offset for Rohm and Haas EUV-2D resist.

Rohm and Haas MET-1K (XP 3454C)

The results of the resist PSF extraction with DC offset term for Rohm and Haas MET-1K (XP 3454C) are shown in Figure 4.11. The best fit was a Gaussian FWHM of 18 nm with a DC offset value of 0.31. Again, the fit quality is greatly improved.

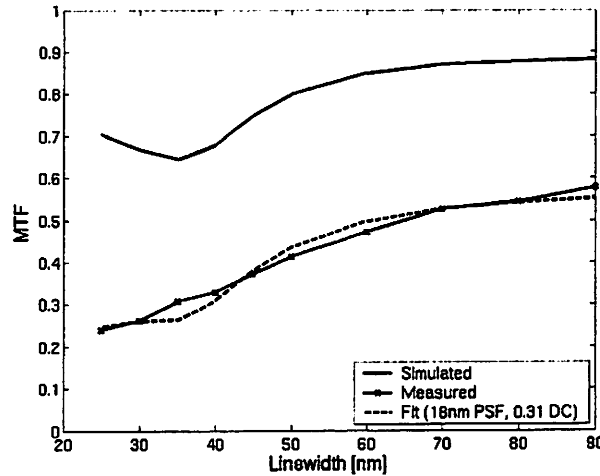

Figure 4.11: Extraction of resist point spread function with DC offset for Rohm and Haas MET-1K (XP 3454C) resist.

KRS resist

The results of the resist PSF extraction with DC offset term for KRS [75] are shown in Figure 4.12. The best fit was a Gaussian FWHM of 18 nm with a DC offset value of 0.25. Once again, the fit quality is greatly improved.

4.4.3 Interpretation of DC Offset Term

As the results of Section 4.4.2 have shown, adding a DC offset term to the model greatly improves the resist PSF fit. The question of how to interpret the DC offset term must therefore be addressed. Optical flare, which is often thought of as a uniform background contrast level, is a likely component. However, as shown in Section 3.2, the amount of flare present in the MET tool is significantly lower (less than 15% in the worst case) than the DC offset seen in these resists (25-30%). The lack of orientation dependence in the CTF

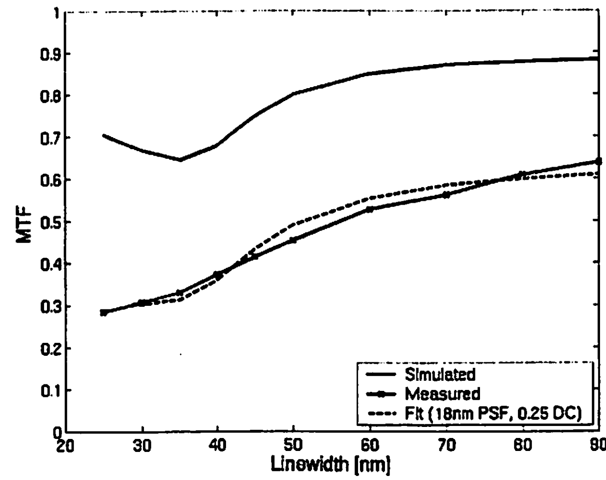

Figure 4.12: Extraction of resist point spread function with DC offset for JSR Micro KRS resist.

as shown in Section 3.3.4 is evidence that at least non-rotationally symmetric aberrations are not dominant in the CTF measurements. However, if a significant amount of spherical aberration (a rotationally symmetric aberration) is present in the system, the contrast could be degraded significantly, leading to the observed results.

Chapter 5

Optical Metrology for Future Technology Nodes

Although the workhorse for CD metrology in the semiconductor industry has long been the critical dimension scanning electron microscope (CD-SEM), the trend towards ever-smaller features in integrated circuits has led the industry to search for other metrology options which can meet the precision and accuracy requirements of manufacturing at these dimensions. One such option is scatterometry, an optical metrology technique in which polarized light is reflected off of a periodic structure on the wafer surface and collected by a detector. Changes in the polarization state of the light collected by the detector may then be analyzed to determine the shape of the features on the wafer. Scatterometry has many advantages: it is non-destructive, fast, and provides the full profile of the features being measured (as opposed to a simple top-down linewidth measurement as with CD-SEMs). This chapter evaluates the effectiveness of scatterometry as a CD metrology technique for

future technology nodes.

5.1 Background

Critical dimension measurements made using scatterometry require two steps. In the first step, polarized light is reflected off of a periodic structure on the surface of a wafer. This periodic structure may be a periodic grating for measuring line profiles, or it could be an array of contact holes. One or more diffracted orders are then measured by a detector. This process is often performed at different wavelengths or angles of incidence in order to obtain more data points. The signal obtained for a given feature is often referred to as a diffraction response. The process of obtaining the diffraction response for the purpose of scatterometry measurements is addressed in Section 5.1.1.

In the second step of scatterometry CD measurements, the feature profile responsible for the observed diffraction response must be determined. This is known as the inverse problem, and will be discussed in Section 5.1.2.

5.1.1 Scatterometry Equipment

There are a variety of different types of scatterometry equipment, and at least three different types have found use in the semiconductor industry. The first type is based on normal-incidence reflectometry. These instruments are simple in construction and simply measure the fraction of light reflected from the surface of a sample. This tool configuration is shown in Figure 5.1a). The primary advantage of this configuration is its simplicity. It requires no polarization optics and typically has a small "footprint," making it a good can-

didate for integration into other processing tools such as resist tracks for *in-situ* metrology applications. However, normal-incidence reflectometers have limited sensitivity for scatterometry when compared with other more complicated techniques.

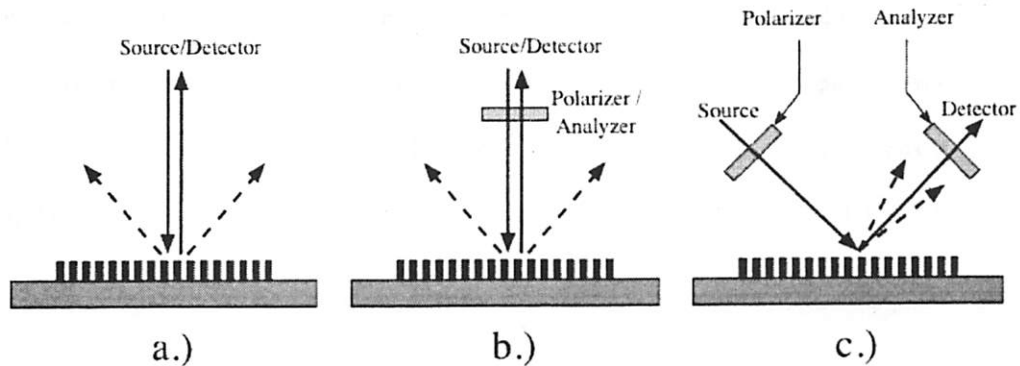

Figure 5.1: Common scatterometry tool configurations. a.) Normal-incidence reflectometer, b.) polarization-sensitive normal-incidence reflectometer, c.) rotating analyzer ellipsometer.

A slight modification to the conventional normal-incidence reflectometer is to add a polarizer between the source and the sample and a second polarizer (called the analyzer) between the sample and the detector. This arrangement allows for independent measurement of the reflectivity of a sample under different polarizations, and is shown in Figure 5.1b). This allows for an increase in the amount of information which can be obtained, and therefore an increase in sensitivity, at the price of a slight increase in tool complexity. Polarization-sensitive normal-incidence reflectometry is also a good candidate for integrated metrology applications.

A third class of scatterometry tools is based upon the spectroscopic ellipsometer. One common type of ellipsometer, the rotating analyzer ellipsometer, is shown in Figure 5.1c), although there are many other types in use as well (nulling ellipsometer, rotating

compensator ellipsometer, etc.). These tools share some of the elements of polarization-sensitive reflectometers, but typically operate at large angles of incidence (that is, far from normal incidence). As the angle of incidence approaches Brewster's angle, the difference between TE and TM polarizations increases, increasing the information contained in the detected signal. In addition, ellipsometers do not measure intensities directly, but rather two signals known as Ψ and Δ, which are related to the complex reflection coefficients for TE (r_s) and TM (r_p) polarization states according to the fundamental equation of ellipsometry,

$$\frac{r_p}{r_s} = \tan(\Psi)e^{i\Delta}. \tag{5.1}$$

Note that $\tan(\Psi)$ represents the ratio of the magnitudes of the TM and TE modes, while Δ represents the relative phase difference between the two modes. Typically only the real part of the phase term, $\cos(\Delta)$, is used. Because ellipsometers depend on the ratio of the magnitudes of the two polarization modes, they are less sensitive to fluctuations in absolute source intensity than reflectometers. In addition, they offer greater sensitivity as mentioned previously. However, they are more complex than the reflectometer configurations discussed, and are more cumbersome to integrate into processing tools due to the need for off-normal angles of incidence.

5.1.2 Solving the Inverse Problem

Each of the tool types discussed in Section 5.1.1 essentially involves reflecting light off of a sample containing periodic structures and measuring some signal (reflectance, Ψ and Δ, etc.) which presumably contains information about the shape of the periodic structures.

This is often referred to as the forward problem. The next step is to analyze the measured signal and deduce the parameters of the periodic structures which would result in such a signal. This step is known as the inverse problem. In order to solve the inverse problem two components are required: a model linking grating parameters with the resulting optical signal, and a method to quickly find the particular parameters which will yield a signal matching the measured results. These components are discussed below.

Rigorous Coupled-Wave Analysis

One of the most popular theoretical diffraction models is known as Rigorous Coupled-Wave Analysis (RCWA) [85,86,87,88,89,90,91]. This method divides the grating into an arbitrary number of horizontal layers, as shown in Figure 5.2. A vector differential formulation of Maxwell's equations is used to describe the electromagnetic fields within each layer, and boundary conditions are applied at each layer interface. The periodic nature of the grating layers is modeled using a Fourier expansion of the electromagnetic permittivity in these layers. Arbitrary grating structures may be represented by dividing the grating into many horizontal layers and varying the width of the grating material for each layer as shown in Figure 5.3.

There are two primary tradeoffs between accuracy and calculation speed for RCWA. The first is the number of layers in the grating structure. Using more layers to represent the grating allows for greater accuracy in representing the actual physical structure, but also increases the computer memory requirements and therefore slows down the calculation speed. The second tradeoff is the number of diffracted orders retained in the calculation. Again, using a higher number of diffracted orders yields greater accuracy, but decreases sim-

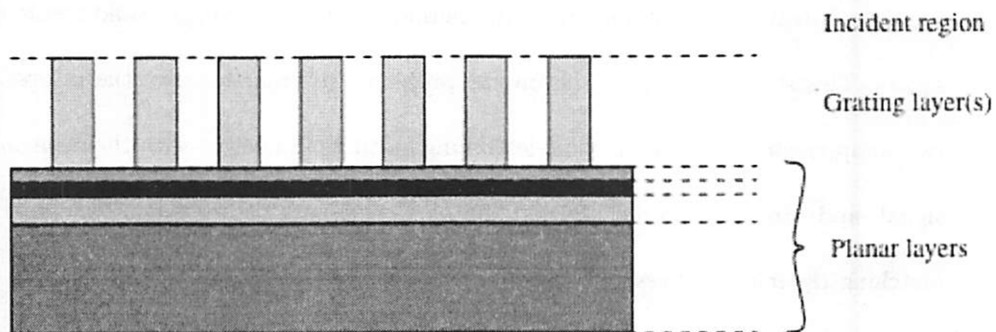

Figure 5.2: Layers within a grating structure as represented in the RCWA formulation.

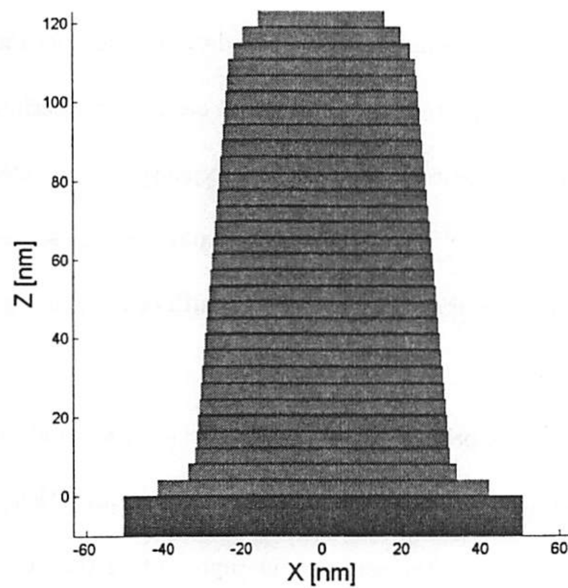

Figure 5.3: Arbitrary grating profiles may be represented by dividing the grating profile into horizontal layers.

ulation speed. These two tradeoffs must be balanced based upon the speed and accuracy requirements of a particular application.

Grating Parameterization

It is important to find a method of describing the film stack and grating layers which is physically realistic while minimizing the total number of parameters (important to solving the inverse problem). One popular profile model which meets these requirements is the "rounded trapezoid" model. This is essentially a trapezoid with a given width, height, and sidewall angle, with corners modeled by circle segments with a specified radius of curvature. This model has only five parameters (width, height, sidewall angle, top rounding and bottom rounding radii), yet it is capable of describing a wide range of grating structures as shown in Figure 5.4.

Regression-Based Versus Library-Based Methods

With measurement data from a scatterometry tool and an RCWA-based model of grating diffraction in place, the final step in a scatterometry measurement is to find the grating profile parameters which produced the measured signal. There are two primary methods for achieving this. The first is through compact modeling run at the time of measurement, also known as real-time regression. This method essentially solves an optimization problem in which the objective is to minimize the difference between the measured and simulated spectra using a metric such as root-mean-square error (RMSE) or mean-square-error (MSE) to quantify this difference. The second method uses a library of simulation results calculated before the measurement is performed. The library should contain all possible combinations

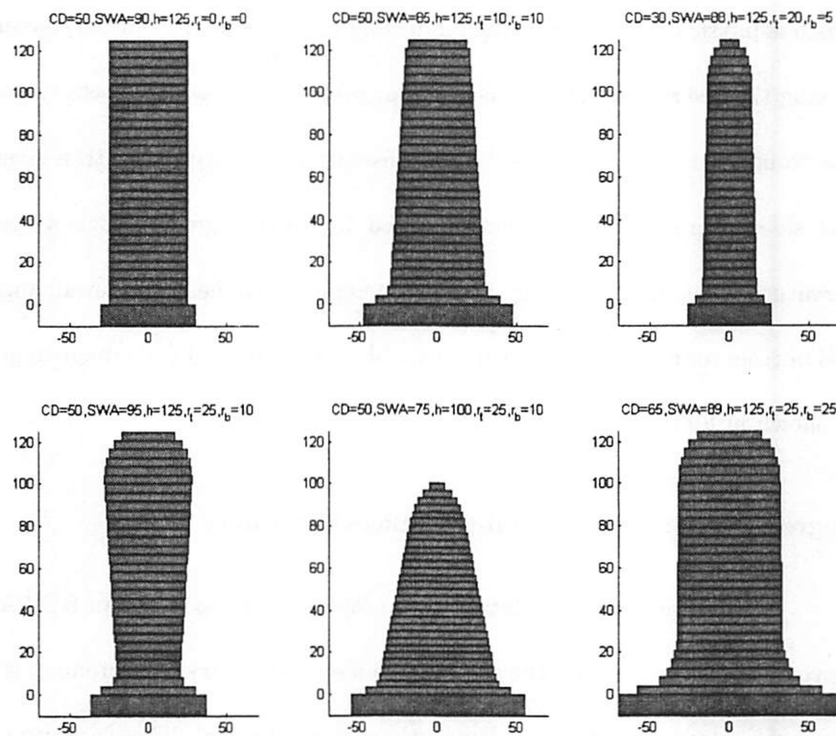

Figure 5.4: Examples of grating profiles described using the "rounded trapezoid" model.

of parameters which could be reasonably be expected to appear in the experiment. A simple search is then conducted to find the library entry which most closely matches the measured diffraction response.

Each method has its advantages and disadvantages. The simulations required to build a library can take hours or days. Regression-based methods do not require these long library simulations, but by the nature of the regression algorithm chosen they may be highly sensitive to the initial parameter values chosen to begin the regression and therefore may converge to a local rather than a global minimum. In addition, library-based techniques require some discretization of parameter values when building the library, while regression-based methods can use continuous parameter values. The correct method to use will most likely depend on the application.

Optical Property Extraction

Regardless of the method used for extracting the profile parameters, it is essential that the optical properties (index of refraction, n, and extinction coefficient, k) of the different materials in the film stack be known with high accuracy. The optical properties are typically measured in a manner similar to scatterometry measurements. An ellipsometer is used to collect data from a sample, and an appropriate dispersion model is selected for each film present in the stack. A regression is then performed to find the dispersion model parameters which correspond to the measured signal. The dispersion model may then be used to determine n and k.

This process was used to measure the optical properties of an extreme ultraviolet photoresist, Rohm and Haas MET-1K (XP 3454C). The resist thickness was 125 nm, and

both post application and post exposure bake temperatures were 130°C. The results are shown in Figure 5.5.

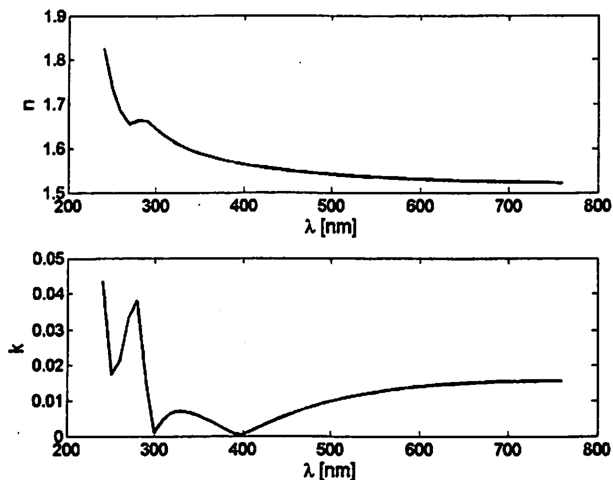

Figure 5.5: Optical properties of Rohm and Haas MET-1K (XP 3454C) photoresist.

In some cases it is also possible to measure the optical properties of a single film within the stack during scatterometry measurements. This is accomplished by measuring the optical properties of a film sample using the process described above to obtain a dispersion model for the film. Then one or more dispersion model parameters may be set as a variable during the regression or library matching stage. It should be noted that this method is best suited to measuring relatively small variations in the optical properties of a material rather than characterizing an unknown material.

5.2 Scatterometry Sensitivity Study for Future Technology Nodes

As feature sizes continue to decrease in future technology nodes, the demands placed on metrology increase dramatically. In this section, a simulation study of the sensitivity of different types of scatterometry tools is conducted to determine whether these tools can meet the CD precision requirements of future technology nodes. Three types of scatterometry tools are considered: normail-incidence reflectometers, polarization-sensitive normal-incidence reflectometers, and spectroscopic ellipsometers.

The feature dimensions and precision requirements are taken from the International Technology Roadmap for Semiconductors (ITRS), 2004 Update [40]. The angle-of-incidence used for simulation of spectroscopic ellipsometry tools is 70°, and the simulation engine used for this study is *gtk* [92]. Only sensitivity to critical dimension variation is studied here; second-order resist effects such as sidewall angle and footing or top-rounding are not considered. Representative values for each of these parameters were chosen for each technology node. In each case, simulations are run at the nominal CD value and at CD values which differ from the nominal by the required metrology precision for each node. Both dense feaures (representative of DRAM structures) and isolated features (representative of microprocessor transistor gates) are considered. For simplicity, the film stack is resist on bare silicon.

Typical noise levels in reflectometers and ellipsometers are on the order of 10^{-3} near the middle of the spectrum used here (240–760 nm) and 10^{-2} at the extreme ends (note that reflectance and the ellipsometry signals $\tan(\Psi)$ and $\cos(\Delta)$ are dimensionless

Table 5.1: Grating parameters and metrology requirements for the 65 nm node from the ITRS [40].

	Dense Features	Isolated Features
Resist CD	65 nm	35 nm
Resist Thickness	180 nm	180 nm
Sidewall Angle	87°	87°
Top Rounding Radius	5 nm	5 nm
Bottom Footing Radius	5 nm	5 nm
CD control (3σ)	8.0 nm	2.2 nm
CD metrology tool precision (3σ)	1.6 nm	0.4 nm

quantities). Exact values are dependent upon the particular details of tool design (source type, detector type, optical design, etc.). Therefore, the objective of this study will be to determine the regions of the spectrum which contain the greatest sensitivity to CD variation, and make at least an estimate of the detection limits which will be required to detect these variations.

5.2.1 The 65 nm Node

The 65 nm technology node is currently forecast to begin in the year 2007. The key grating parameters used for simulations for this node are given in Table 5.1. The simulation results for dense features are given in Figures 5.6–5.8, while the results for isolated features are shown in Figures 5.9–5.11.

For dense features at the 65 nm node, the reflectometry simulation results (Figure 5.6) show that there is a region of sensitivity between about 310 nm and 460 nm which would be detectable if noise levels can be controlled to below 10^{-3} in this region. There are also smaller regions of sensitivity at the extreme ends of the spectrum, but noise levels are typically higher at these wavelengths. The polarized reflectometry simulations (Figure 5.7)

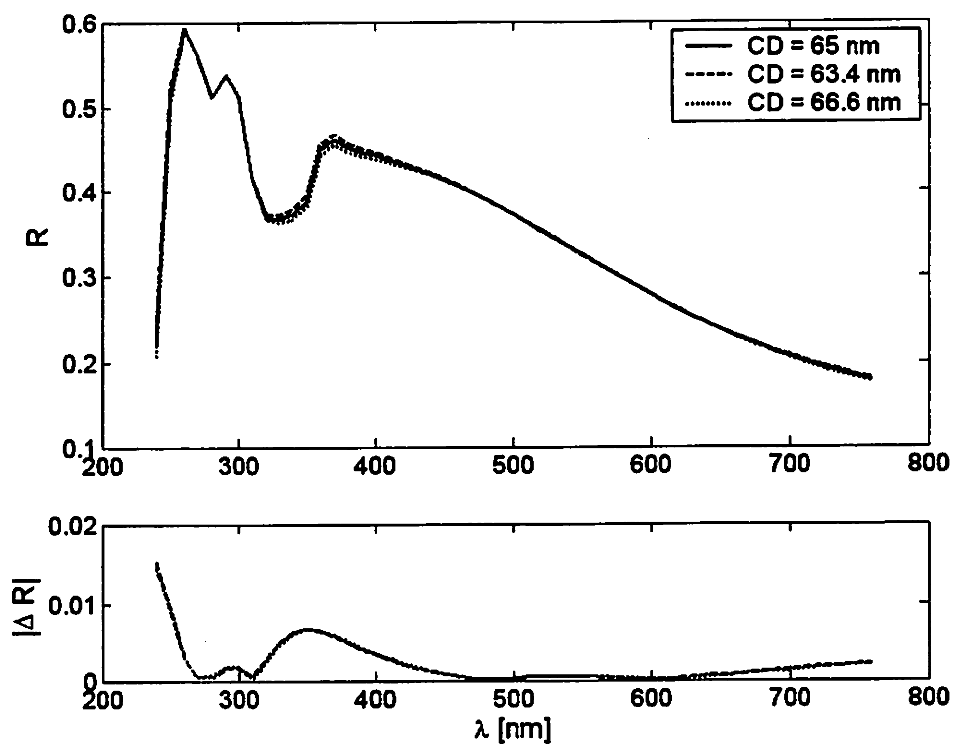

Figure 5.6: Reflectometer response for 65 nm node dense features and change in reflectometer response ($|\Delta R|$) for CD change equivalent to required metrology tool 3σ precision.

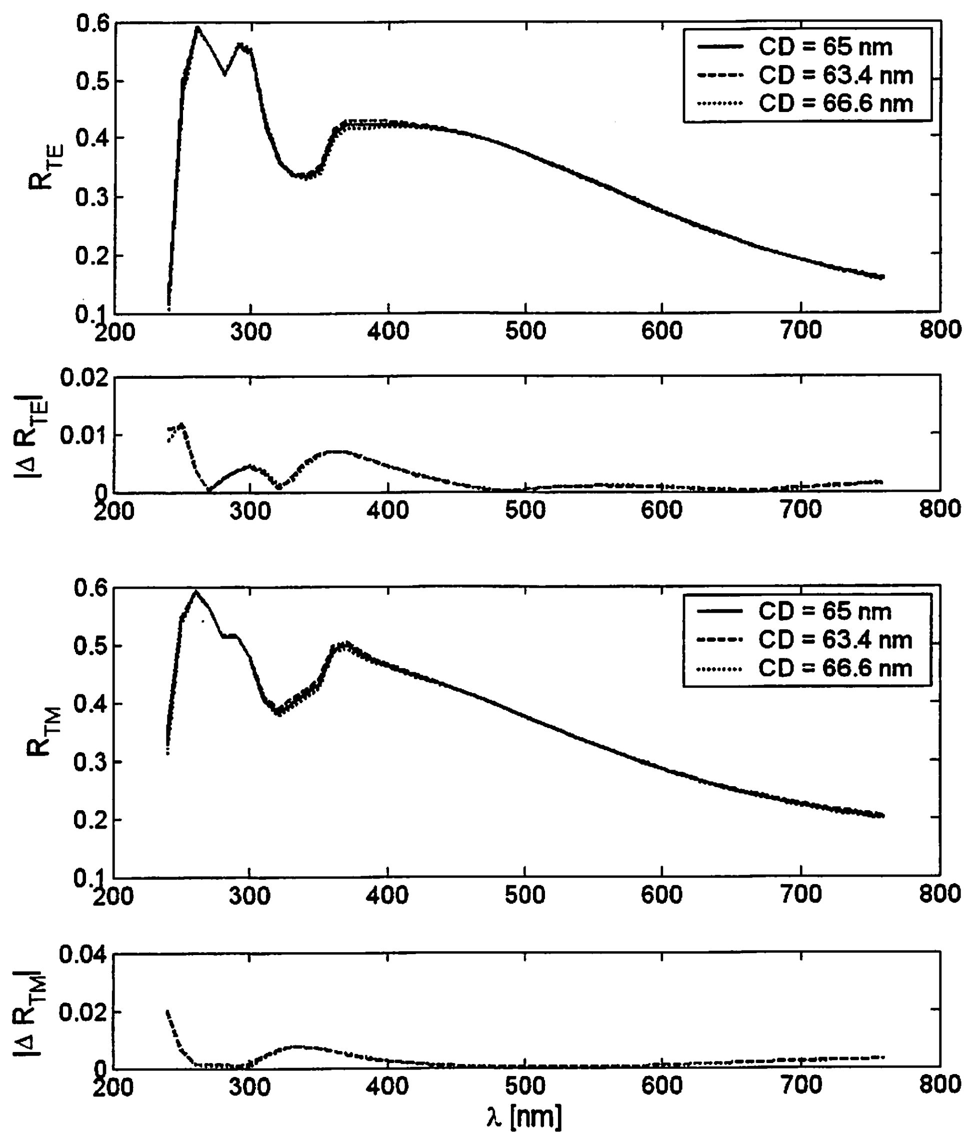

Figure 5.7: Polarization-sensitive reflectometer response for 65 nm node dense features and change in reflectometer response ($|\Delta R_{TE}|$ and $|\Delta R_{TM}|$) for CD change equivalent to required metrology tool 3σ precision.

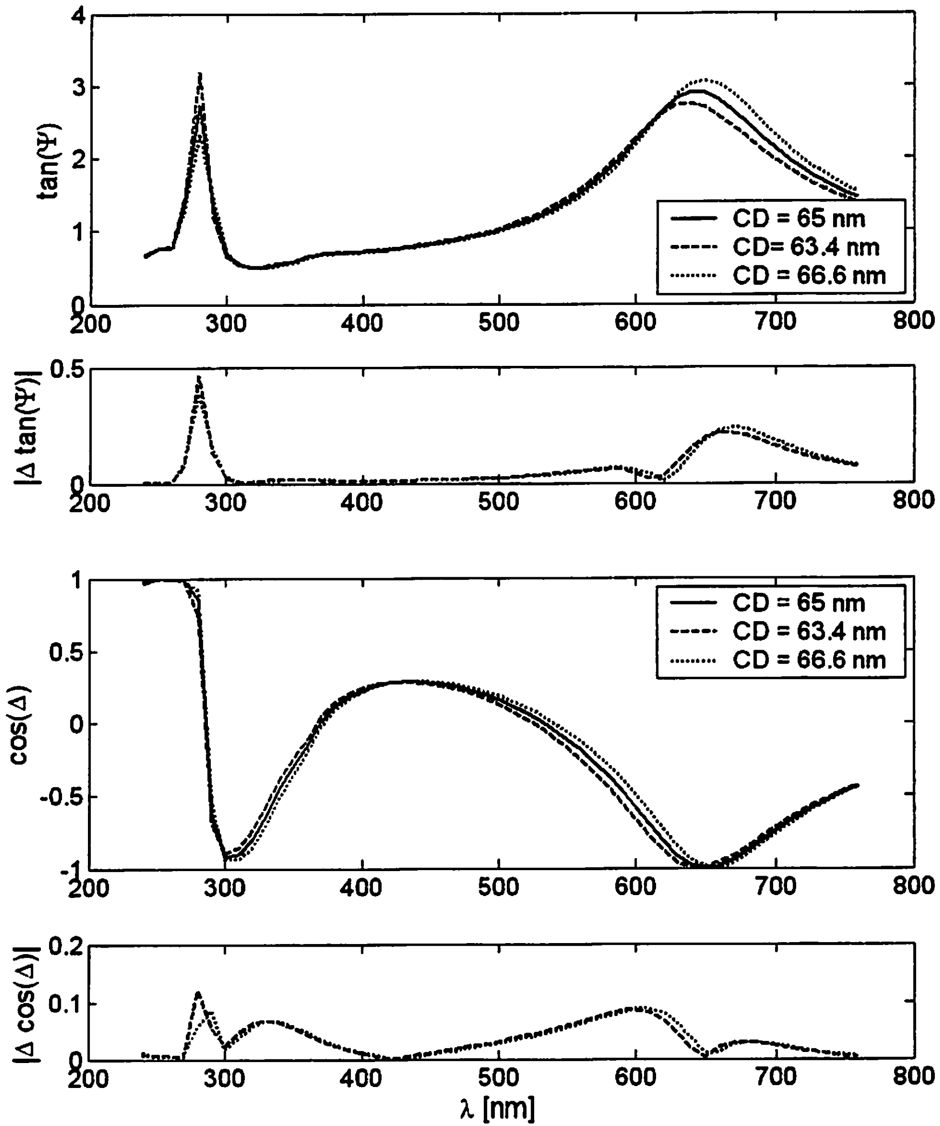

Figure 5.8: Spectroscopic ellipsometry response for 65 nm node dense features and change in ellipsometry response ($|\Delta \tan(\Psi)|$ and $|\Delta \cos(\Delta)|$ for CD change equivalent to required metrology tool 3σ precision.

show sensitivity of a similar magnitude and over a similar spectral region to the unpolarized reflectometry results. However, this technique has the advantage of providing two signals with which to perform model fitting, which reduces the overall sensitivity to noise (at the expense of a slower measurement). The ellipsometry results (Figure 5.8) show good sensitivity virtually throughout the entire spectrum. The sensitivity levels are also higher than for either reflectometry technique. This indicates that ellipsometry offers higher precision than either reflectometry technique, at the expense of slower measurement time, larger spot size (due to the large angle of incidence), and mechanical complexity.

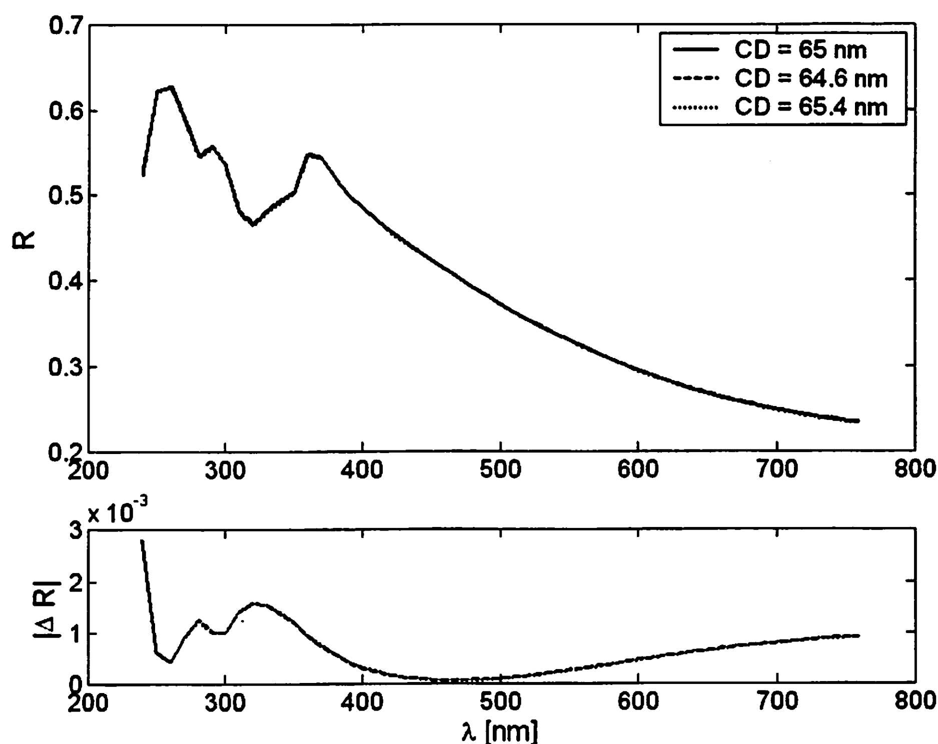

Figure 5.9: Reflectometer response for 65 nm node isolated features and change in reflectometer response ($|\Delta R|$) for CD change equivalent to required metrology tool 3σ precision.

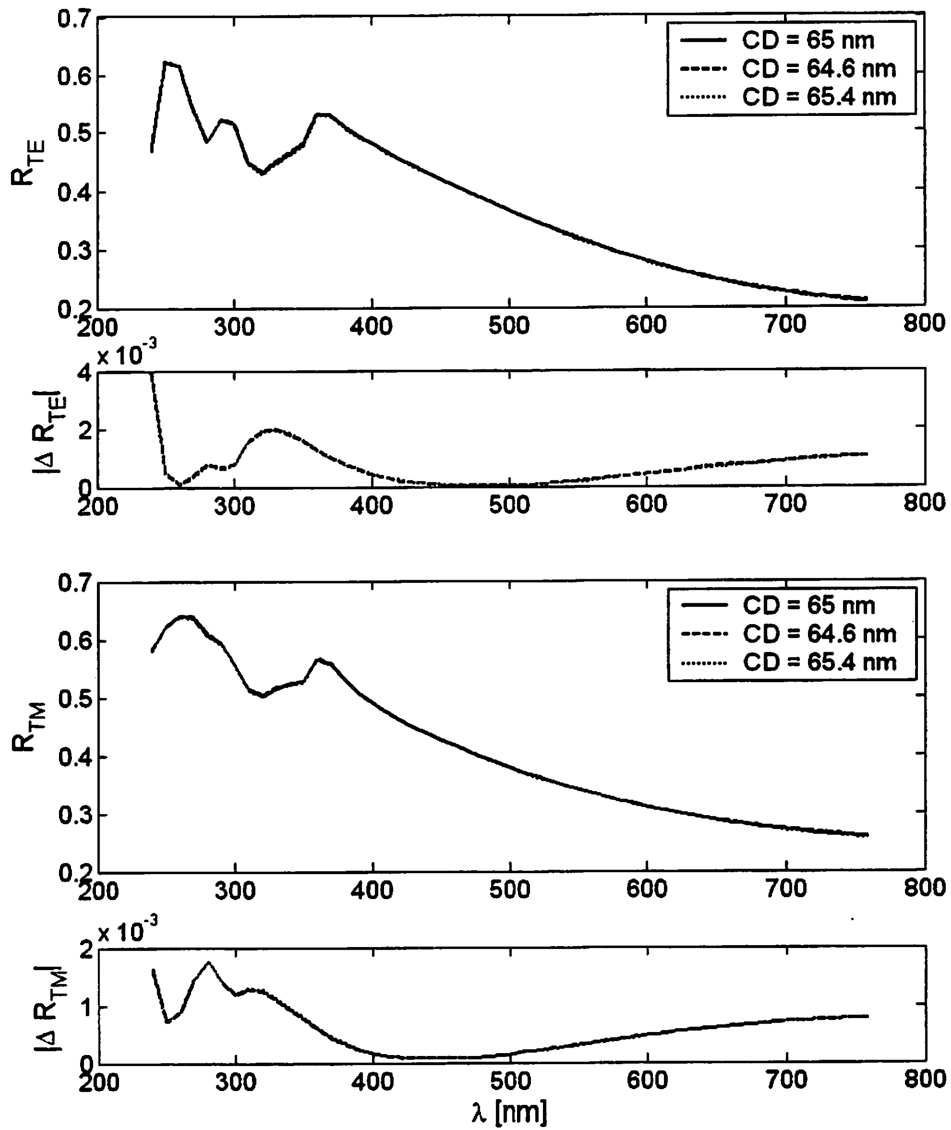

Figure 5.10: Polarization-sensitive reflectometer response for 65 nm node isolated features and change in reflectometer response ($|\Delta R_{TE}|$ and $|\Delta R_{TM}|$) for CD change equivalent to required metrology tool 3σ precision.

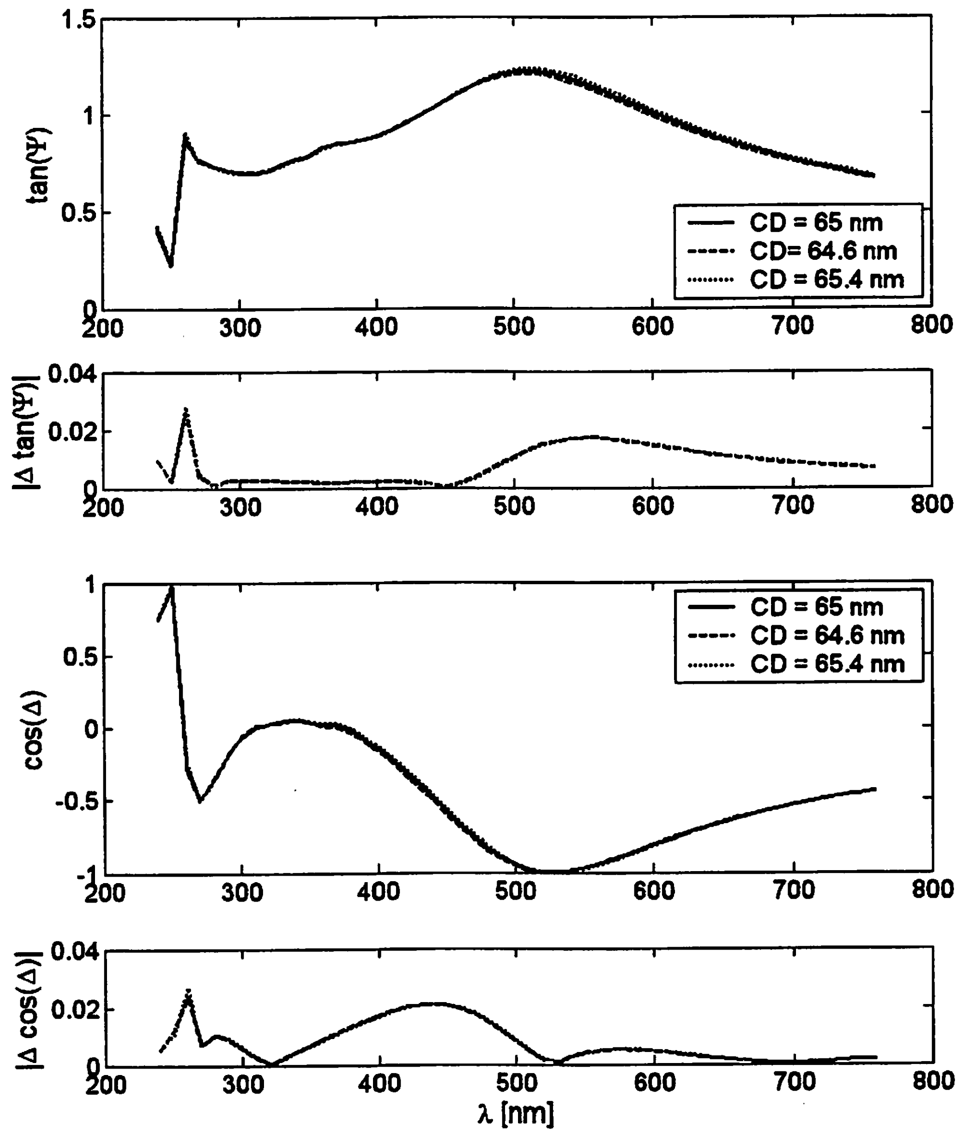

Figure 5.11: Spectroscopic ellipsometry response for 65 nm node isolated features and change in ellipsometry response ($|\Delta \tan(\Psi)|$ and $|\Delta \cos(\Delta)|$ for CD change equivalent to required metrology tool 3σ precision.

Table 5.2: Grating parameters and metrology requirements for the 45 nm node from the ITRS [40].

	Dense Features	Isolated Features
Resist CD	45 nm	25 nm
Resist Thickness	140 nm	140 nm
Sidewall Angle	87°	87°
Top Rounding Radius	3 nm	3 nm
Bottom Footing Radius	3 nm	3 nm
CD control (3σ)	5.5 nm	1.6 nm
CD metrology tool precision (3σ)	1.1 nm	0.3 nm

For isolated features at the 65 nm node, the reflectometry results (Figure 5.9) show relatively low sensitivity levels. Only a small window between about 270 nm and 350 nm exceeds the 10^{-3} threshold, and this window is close enough to the short wavelength end of the spectrum that achieving such noise levels is a significant challenge. The polarized reflectometry results 5.10) show a slight improvement in sensitivity over the unpolarized results, and at least in the TE case this sensitivity occurs at a slightly higher wavelength range. Again, the ellipsometry results (Figure 5.11) show sensitivity across most of the spectrum, with the $\tan(\Psi)$ signal showing good sensitivity above about 450 nm and the $\cos(\Delta)$ signal showing good sensitivity below about 520 nm.

5.2.2 The 45 nm Node

The 45 nm technology node is currently forecast to begin in the year 2010. The key grating parameters used for simulations for this node are given in Table 5.2. The simulation results for dense features are given in Figures 5.12–5.14, while the results for isolated features are shown in Figures 5.15–5.17.

For dense features at the 45 nm node, the reflectometry simulation results (Figure

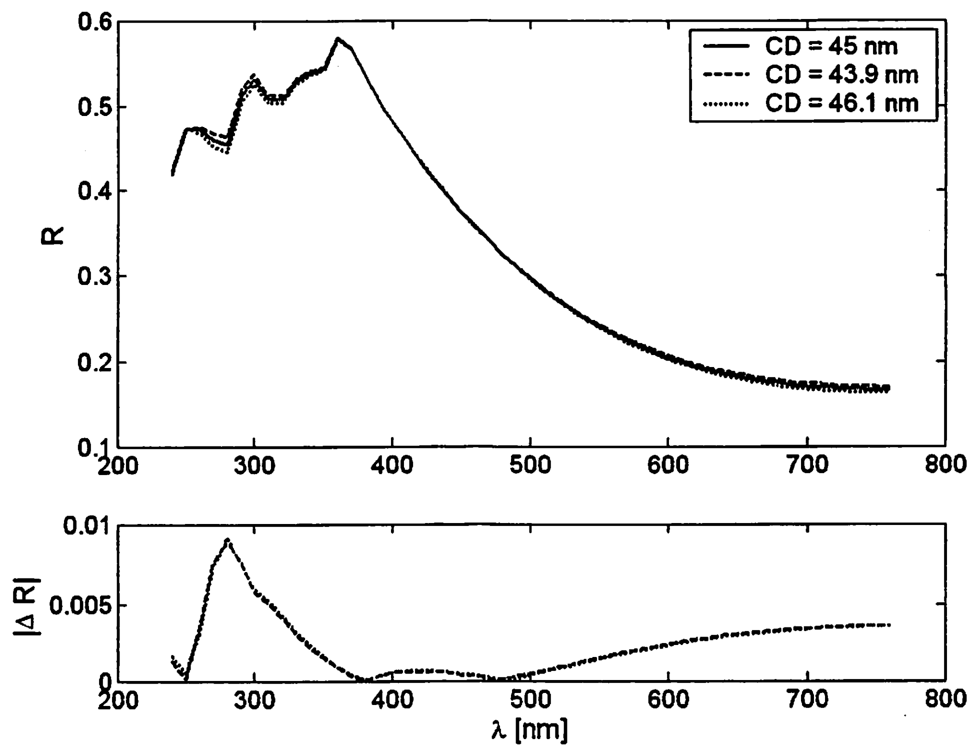

Figure 5.12: Reflectometer response for 45 nm node dense features and change in reflectometer response ($|\Delta R|$) for CD change equivalent to required metrology tool 3σ precision.

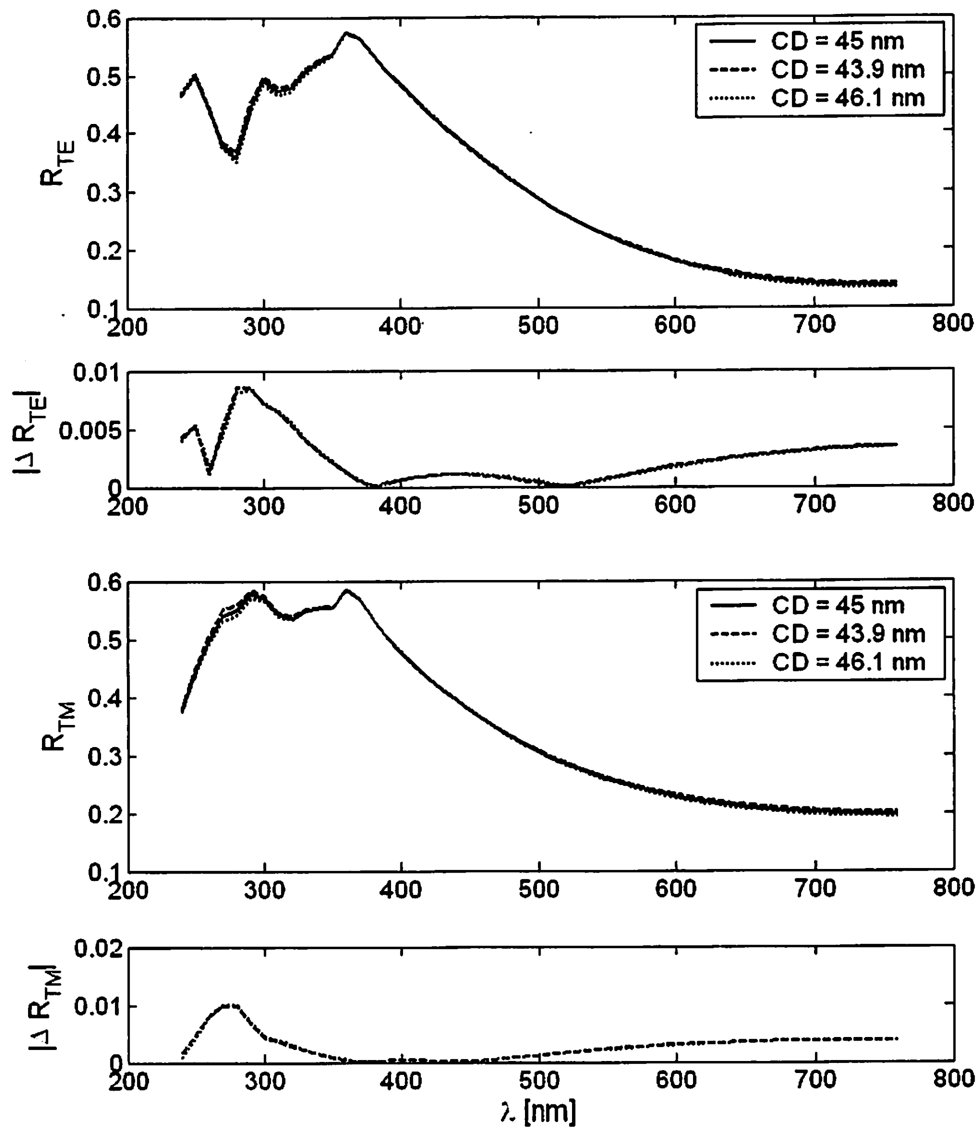

Figure 5.13: Polarization-sensitive reflectometer response for 45 nm node dense features and change in reflectometer response ($|\Delta R_{TE}|$ and $|\Delta R_{TM}|$) for CD change equivalent to required metrology tool 3σ precision.

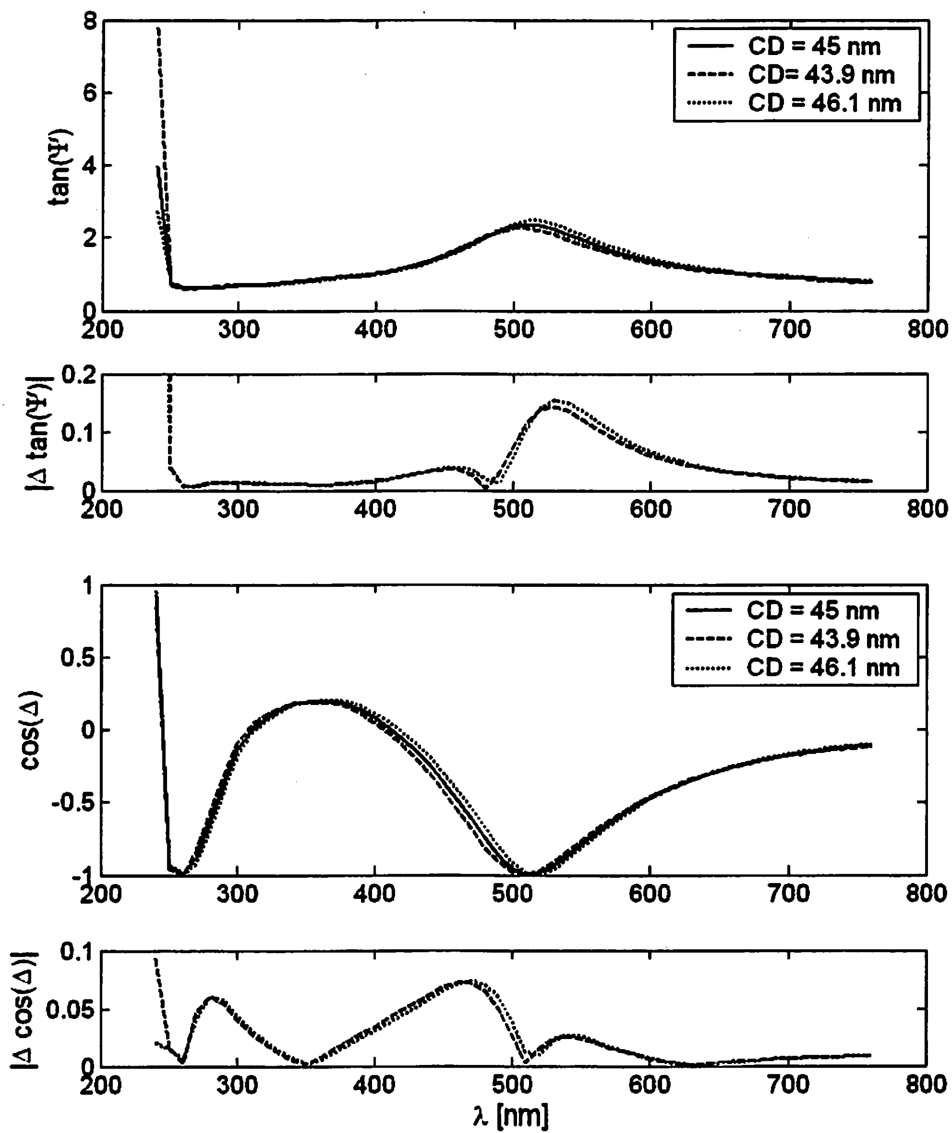

Figure 5.14: Spectroscopic ellipsometry response for 45 nm node dense features and change in ellipsometry response ($|\Delta \tan(\Psi)|$ and $|\Delta \cos(\Delta)|$ for CD change equivalent to required metrology tool 3σ precision.

5.12) show that there is a region of sensitivity between about 260 nm and 370 nm which would be detectable if noise levels can be controlled to below 10^{-3} in this region. In addition, sensitivity levels increase to potentially detectable levels above about 520 nm. The polarized reflectometry simulations (Figure 5.13) show sensitivity of a similar magnitude and over a similar spectral region to the unpolarized reflectometry results. The ellipsometry results (Figure 5.14) show good sensitivity virtually throughout the entire spectrum. The sensitivity levels are also higher than for either reflectometry technique.

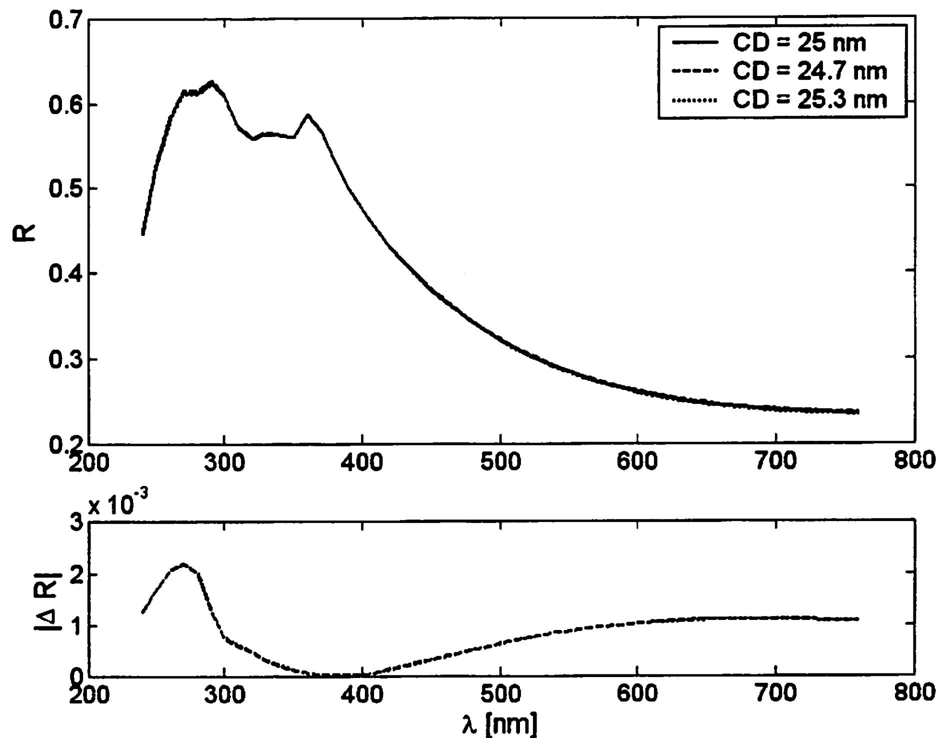

Figure 5.15: Reflectometer response for 45 nm node isolated features and change in reflectometer response ($|\Delta R|$) for CD change equivalent to required metrology tool 3σ precision.

For isolated features at the 45 nm node, the reflectometry simulation results (Fig-

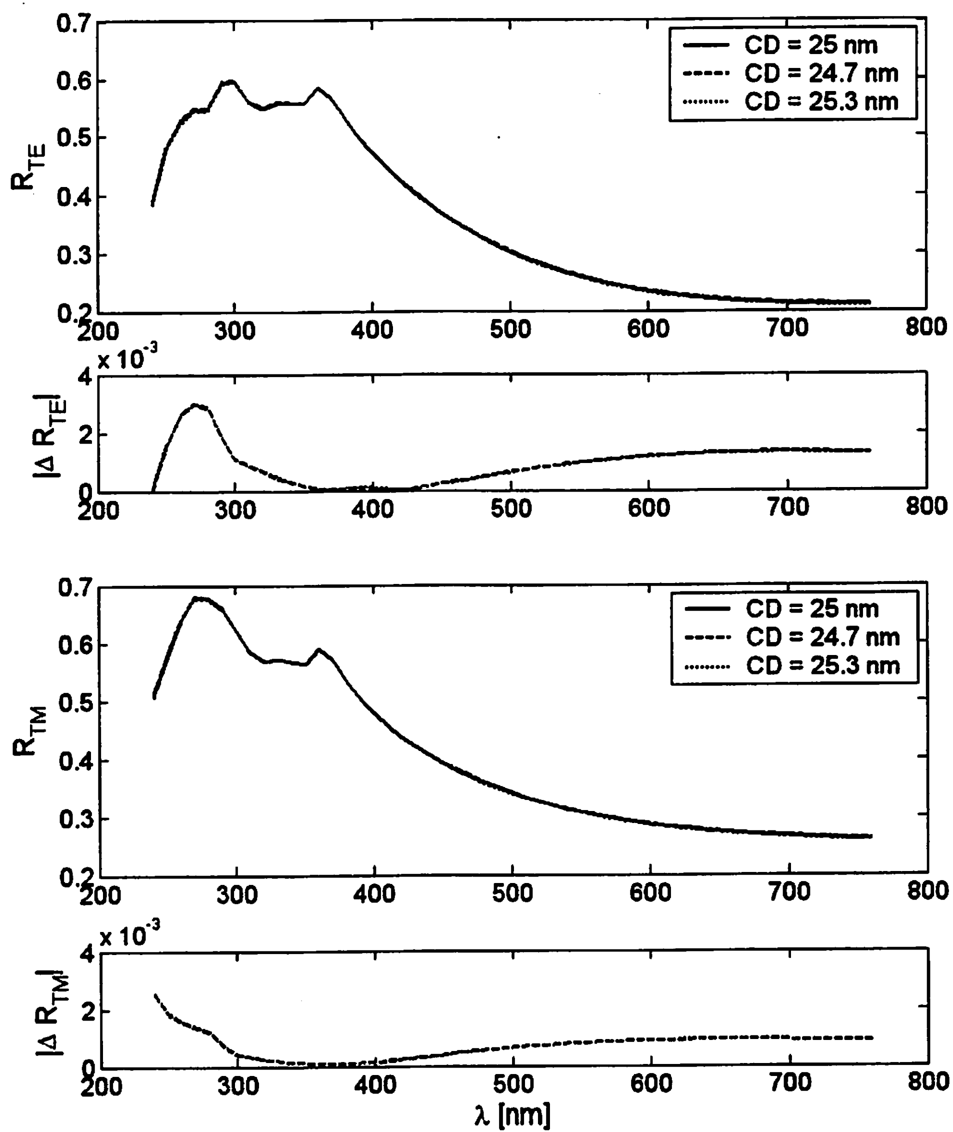

Figure 5.16: Polarization-sensitive reflectometer response for 45 nm node isolated features and change in reflectometer response ($|\Delta R_{TE}|$ and $|\Delta R_{TM}|$) for CD change equivalent to required metrology tool 3σ precision.

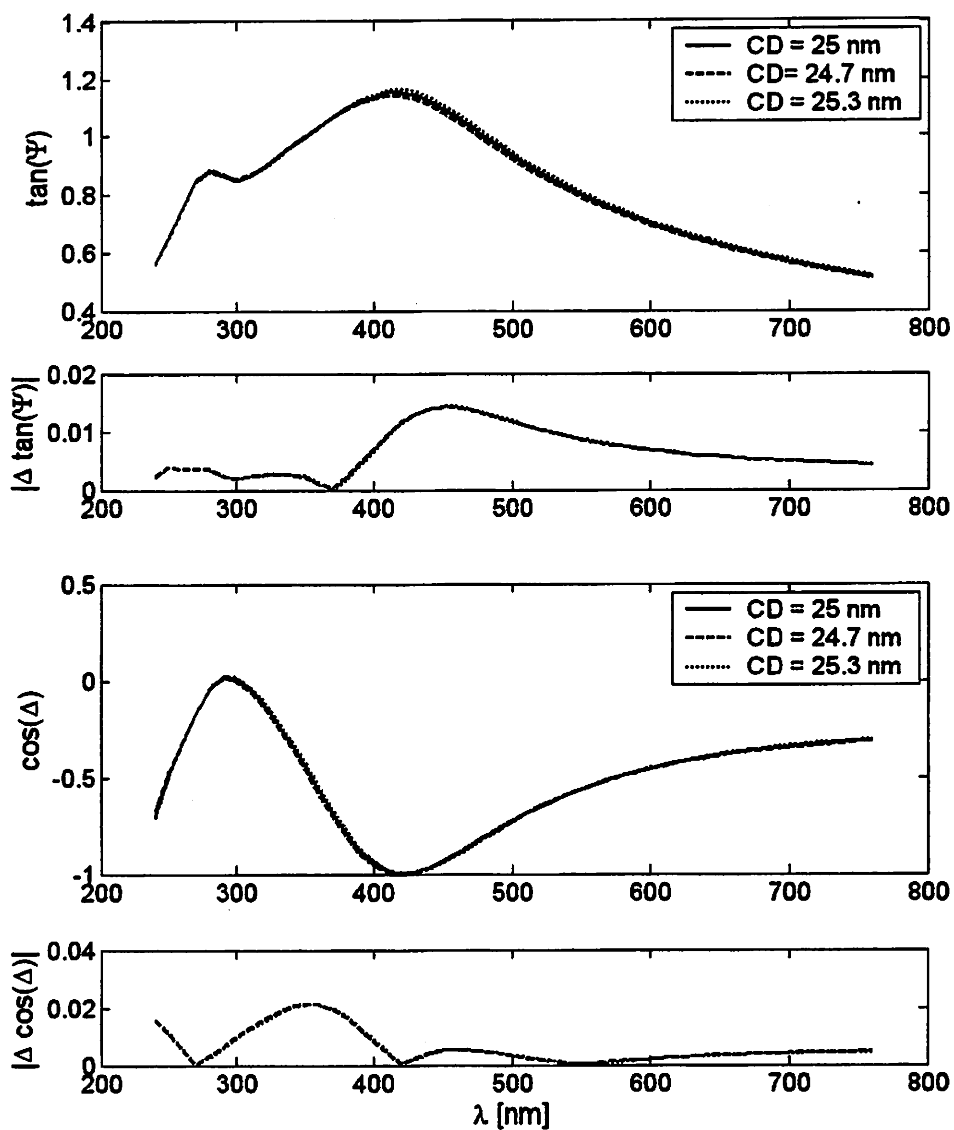

Figure 5.17: Spectroscopic ellipsometry response for 45 nm node isolated features and change in ellipsometry response ($|\Delta \tan(\Psi)|$ and $|\Delta \cos(\Delta)|$ for CD change equivalent to required metrology tool 3σ precision.

Table 5.3: Grating parameters and metrology requirements for the 32 nm node from the ITRS [40].

	Dense Features	Isolated Features
Resist CD	32 nm	18 nm
Resist Thickness	120 nm	120 nm
Sidewall Angle	87°	87°
Top Rounding Radius	2 nm	2 nm
Bottom Footing Radius	2 nm	2 nm
CD control (3σ)	3.9 nm	1.2 nm
CD metrology tool precision (3σ)	0.8 nm	0.2 nm

ure 5.15) show that the greatest sensitivity lies below 300 nm. Noise levels in this portion of the spectrum may exceed the signal variations due to CD change, however. Therefore, reflectometry methods may be unable to measure CD for isolated features with the required precision at the 45 nm node. The polarized reflectometry simulations (Figure 5.16) show slightly increased sensitivity compared with unpolarized reflectometry, and the sensitivity occurs over a similar wavelength range. In addition, the sensitivity at wavelengths above about 550 nm increases to levels which may be detectable, although they are still near the noise levels. Once again, the ellipsometry results (Figure 5.17) show good sensitivity virtually throughout the entire spectrum. The sensitivity levels are also higher than for either reflectometry technique.

5.2.3 The 32 nm Node

The 32 nm technology node is currently forecast to begin in the year 2013. The key grating parameters used for simulations for this node are given in Table 5.3. The simulation results for dense features are given in Figures 5.18–5.20, while the results for isolated features are shown in Figures 5.21–5.23.

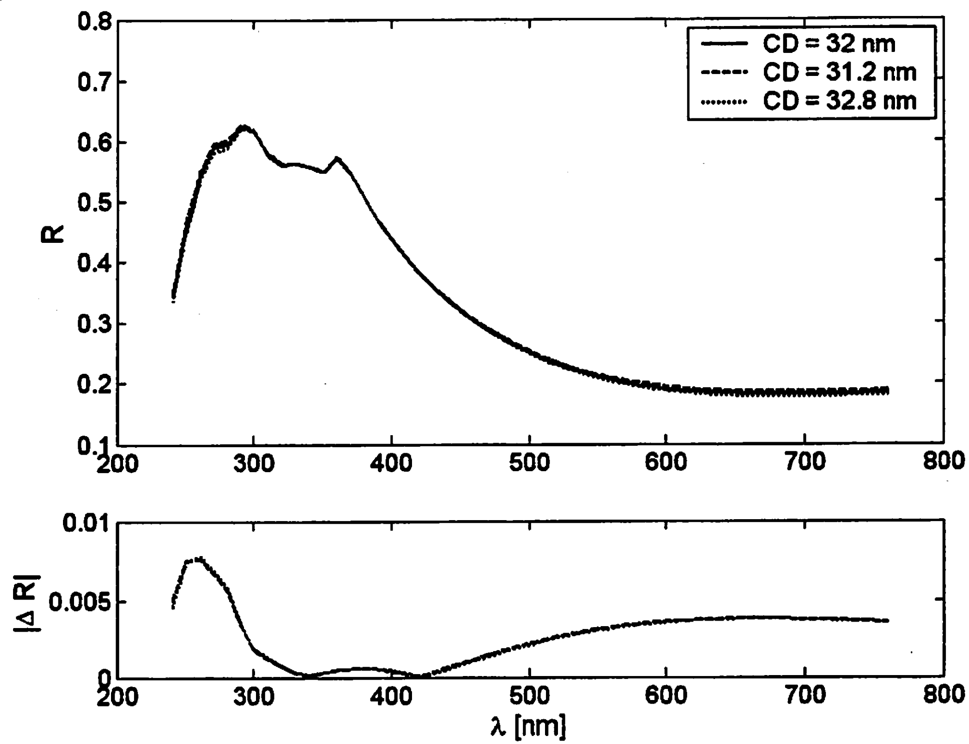

Figure 5.18: Reflectometer response for 32 nm node dense features and change in reflectometer response ($|\Delta R|$) for CD change equivalent to required metrology tool 3σ precision.

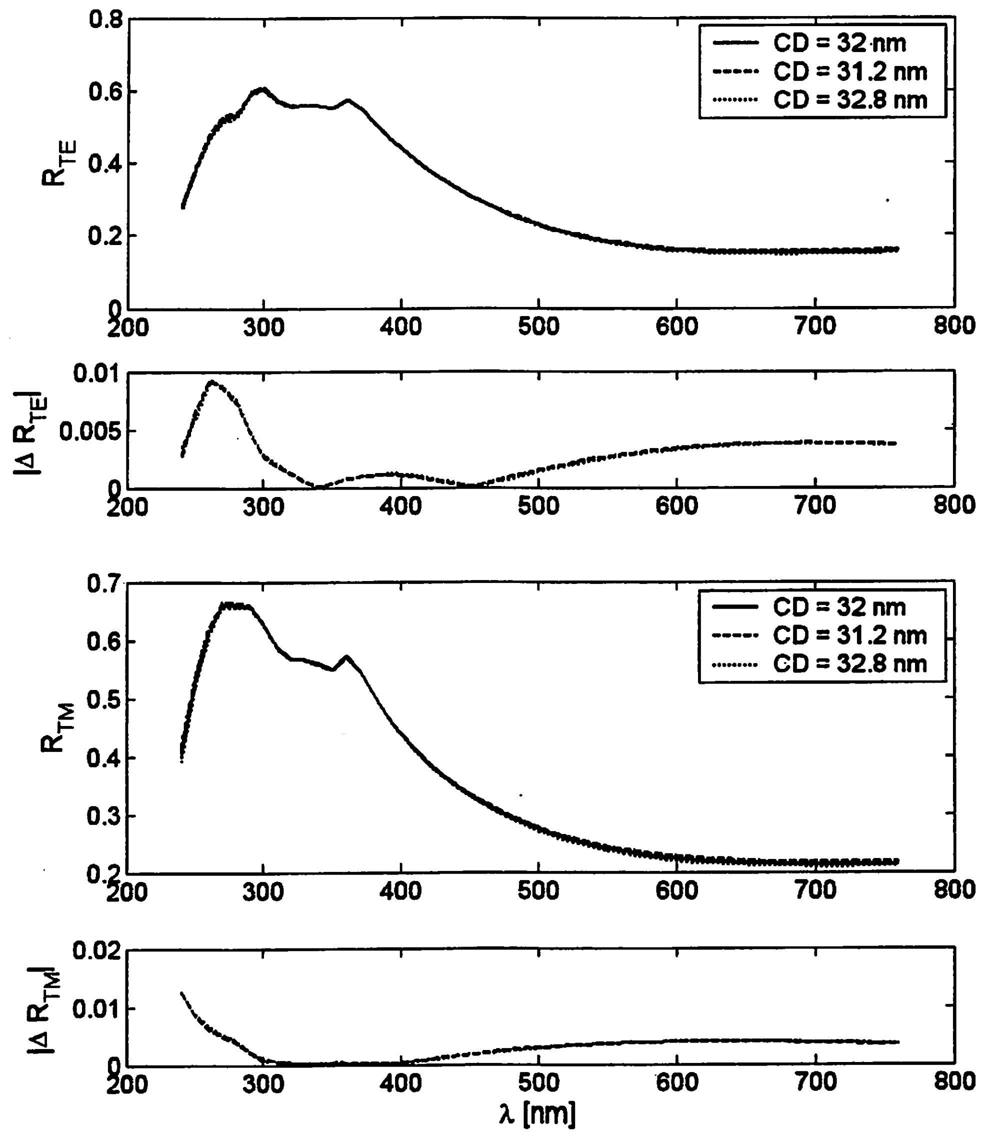

Figure 5.19: Polarization-sensitive reflectometer response for 32 nm node dense features and change in reflectometer response ($|\Delta R_{TE}|$ and $|\Delta R_{TM}|$) for CD change equivalent to required metrology tool 3σ precision.

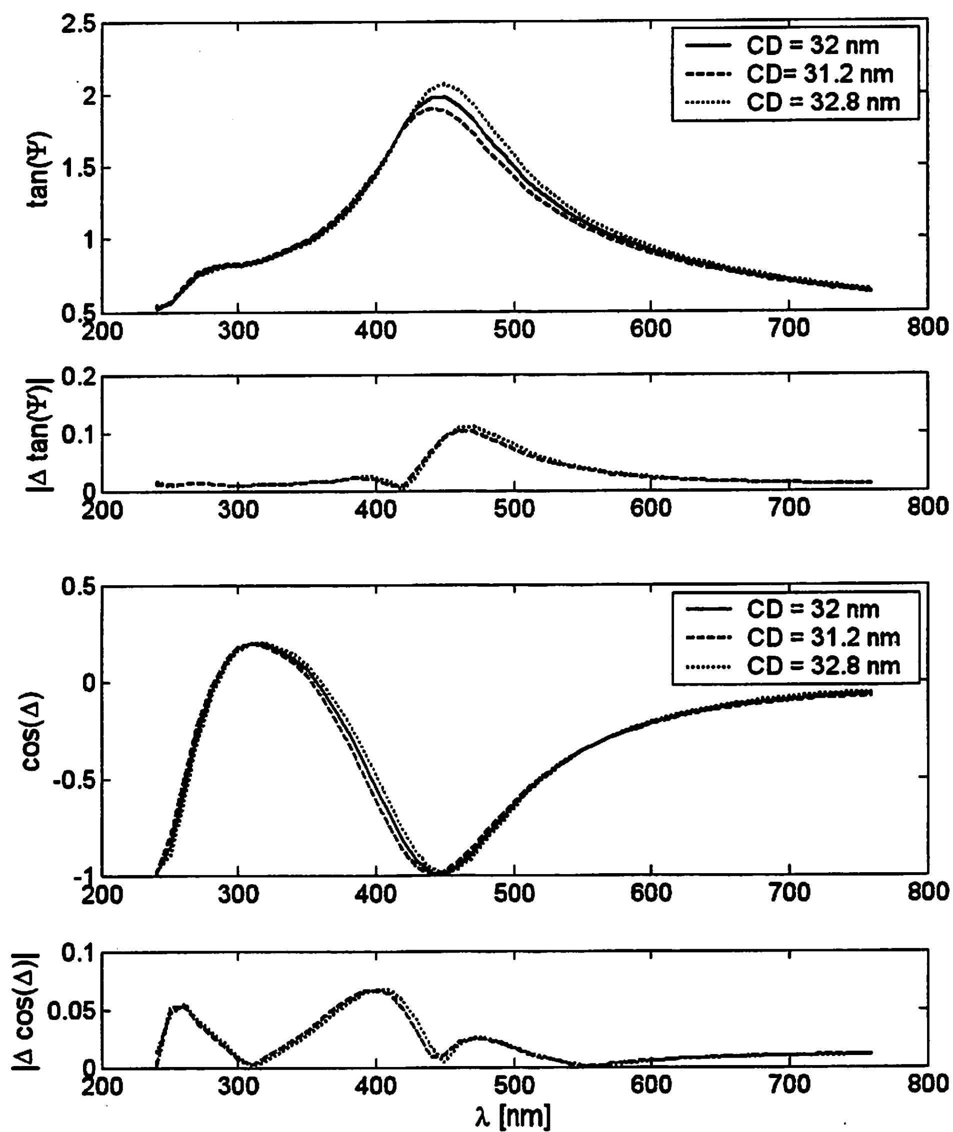

Figure 5.20: Spectroscopic ellipsometry response for 32 nm node dense features and change in ellipsometry response ($|\Delta \tan(\Psi)|$ and $|\Delta \cos(\Delta)|$ for CD change equivalent to required metrology tool 3σ precision.

For dense features at the 32 nm node, the reflectometry simulation results (Figure 5.18) show that although there is a region of sensitivity below about 310 nm, this level of signal variation may not be detectable above the noise levels in this region. However, sensitivity levels increase to potentially detectable levels above about 500 nm. The polarized reflectometry simulations (Figure 5.19) show sensitivity of a similar magnitude and over a similar spectral region to the unpolarized reflectometry results. The ellipsometry results (Figure 5.20) show good sensitivity virtually throughout the entire spectrum. The sensitivity levels are also higher than for either reflectometry technique.

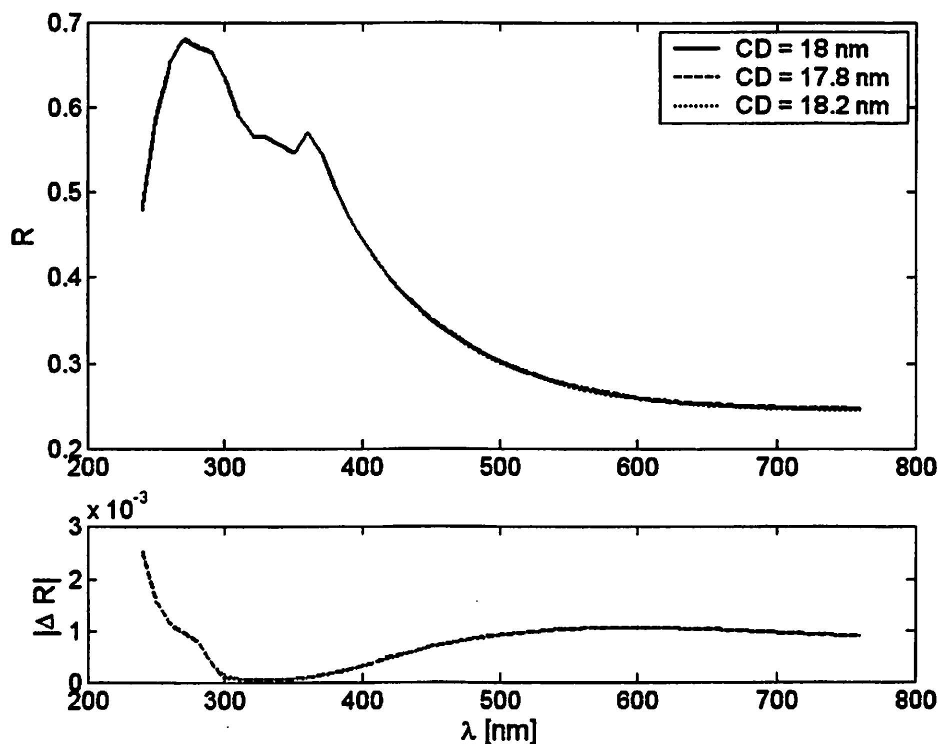

Figure 5.21: Reflectometer response for 32 nm node isolated features and change in reflectometer response ($|\Delta R|$) for CD change equivalent to required metrology tool 3σ precision.

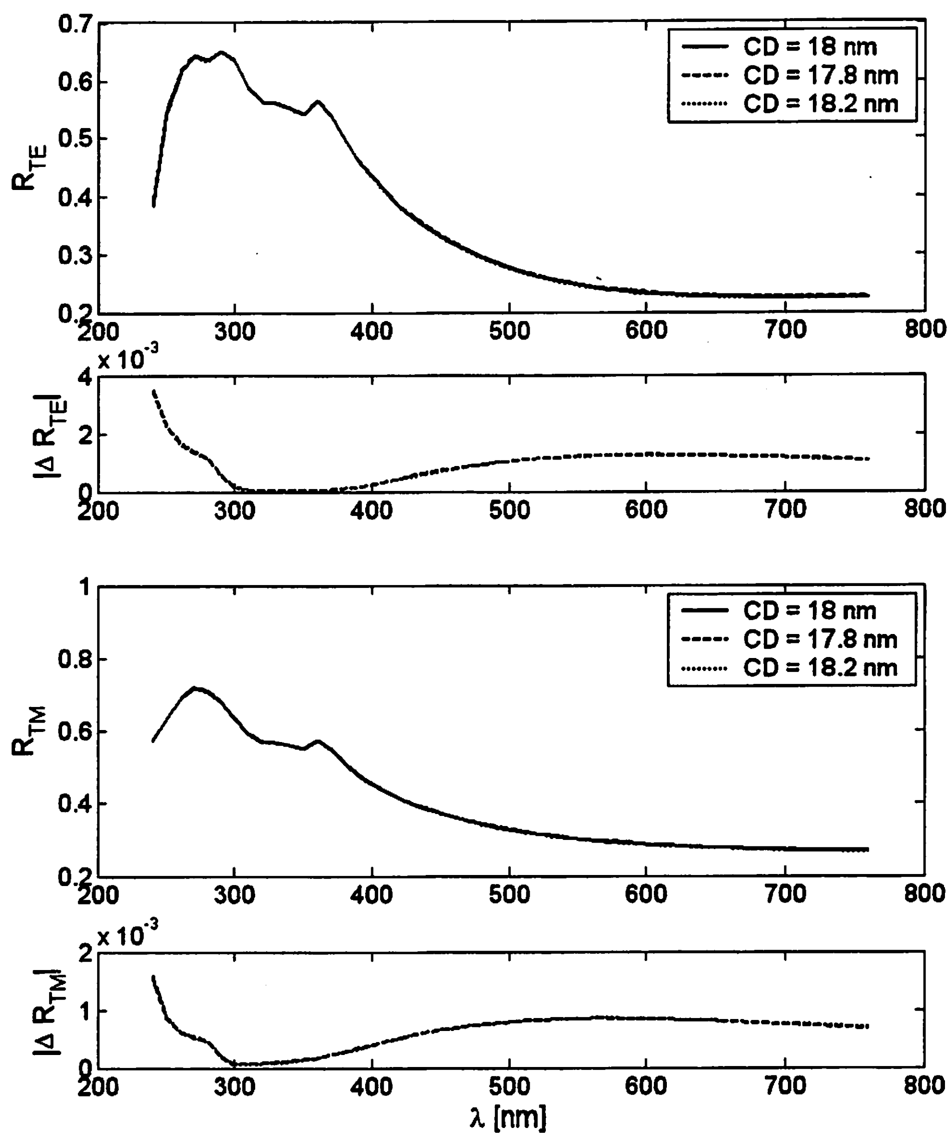

Figure 5.22: Polarization-sensitive reflectometer response for 32 nm node isolated features and change in reflectometer response ($|\Delta R_{TE}|$ and $|\Delta R_{TM}|$) for CD change equivalent to required metrology tool 3σ precision.

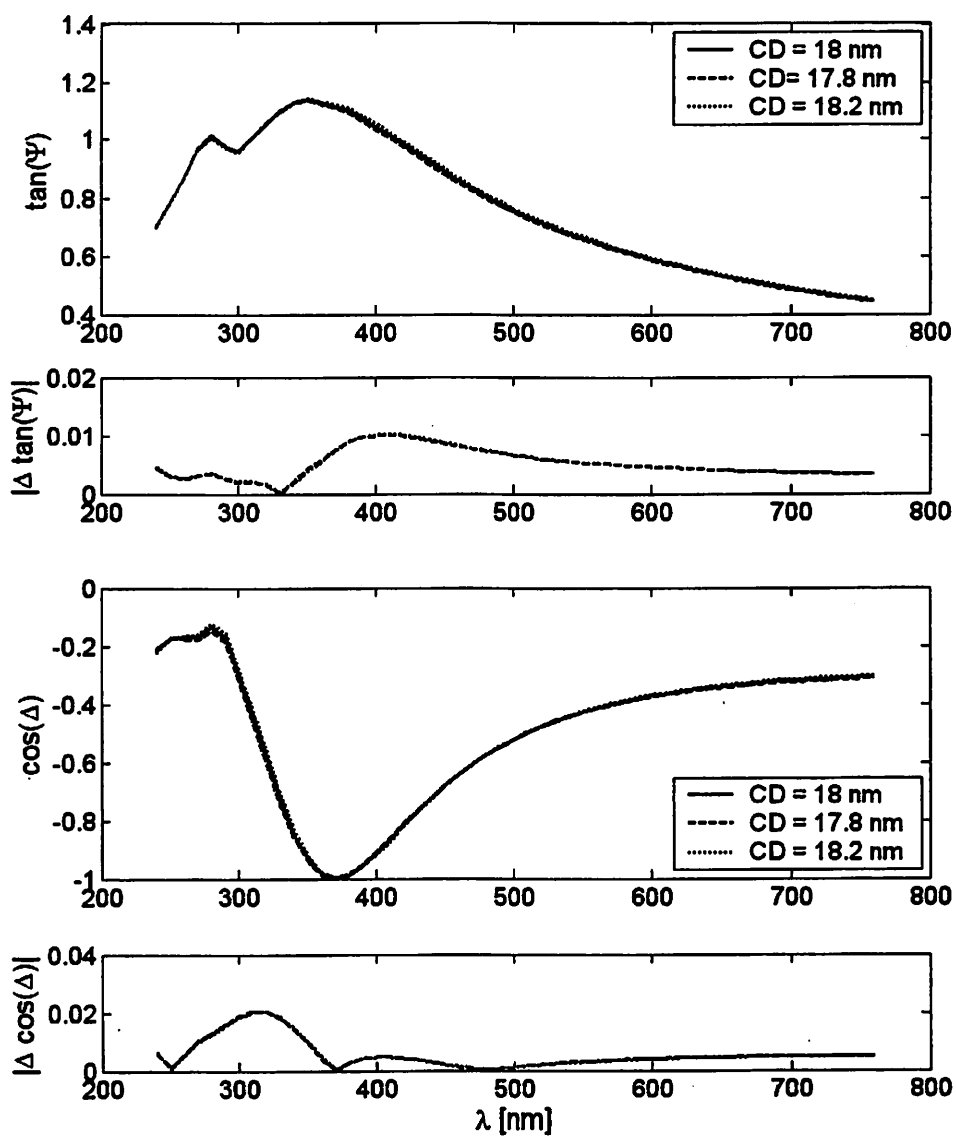

Figure 5.23: Spectroscopic ellipsometry response for 32 nm node isolated features and change in ellipsometry response ($|\Delta \tan(\Psi)|$ and $|\Delta \cos(\Delta)|$ for CD change equivalent to required metrology tool 3σ precision.

Table 5.4: Grating parameters and metrology requirements for the 22 nm node from the ITRS [40].

	Dense Features	Isolated Features
Resist CD	22 nm	13 nm
Resist Thickness	80 nm	80 nm
Sidewall Angle	87°	87°
Top Rounding Radius	2 nm	2 nm
Bottom Footing Radius	2 nm	2 nm
CD control (3σ)	2.7 nm	0.8 nm
CD metrology tool precision (3σ)	0.5 nm	0.2 nm

For isolated features at the 32 nm node, the reflectometry simulation results (Figure 5.21) show that there may be no spectrum region where the signal variation due to CD change exceeds the noise levels present in th system. Therefore, reflectometry methods may be unable to measure CD for isolated features with the required precision at the 32 nm node. The polarized reflectometry simulations (Figure 5.22) show slightly increased sensitivity compared with unpolarized reflectometry, and the sensitivity occurs over a similar wavelength range. In addition, the sensitivity at wavelengths above about 550 nm increases to levels which may be detectable, although they are still near the noise levels. Once again, the ellipsometry results (Figure 5.23) show good sensitivity virtually throughout the entire spectrum. The sensitivity levels are also higher than for either reflectometry technique.

5.2.4 The 22 nm Node

The 22 nm technology node is currently forecast to begin in the year 2016. The key grating parameters used for simulations for this node are given in Table 5.4. The simulation results for dense features are given in Figures 5.24–5.26, while the results for isolated features are shown in Figures 5.27–5.29.

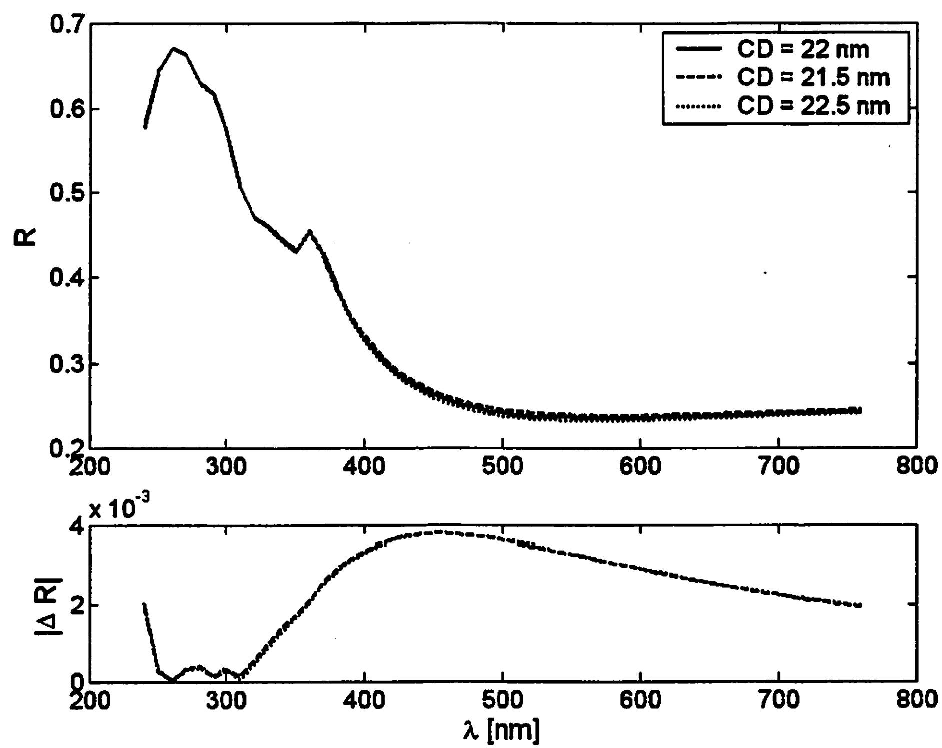

Figure 5.24: Reflectometer response for 22 nm node dense features and change in reflectometer response ($|\Delta R|$) for CD change equivalent to required metrology tool 3σ precision.

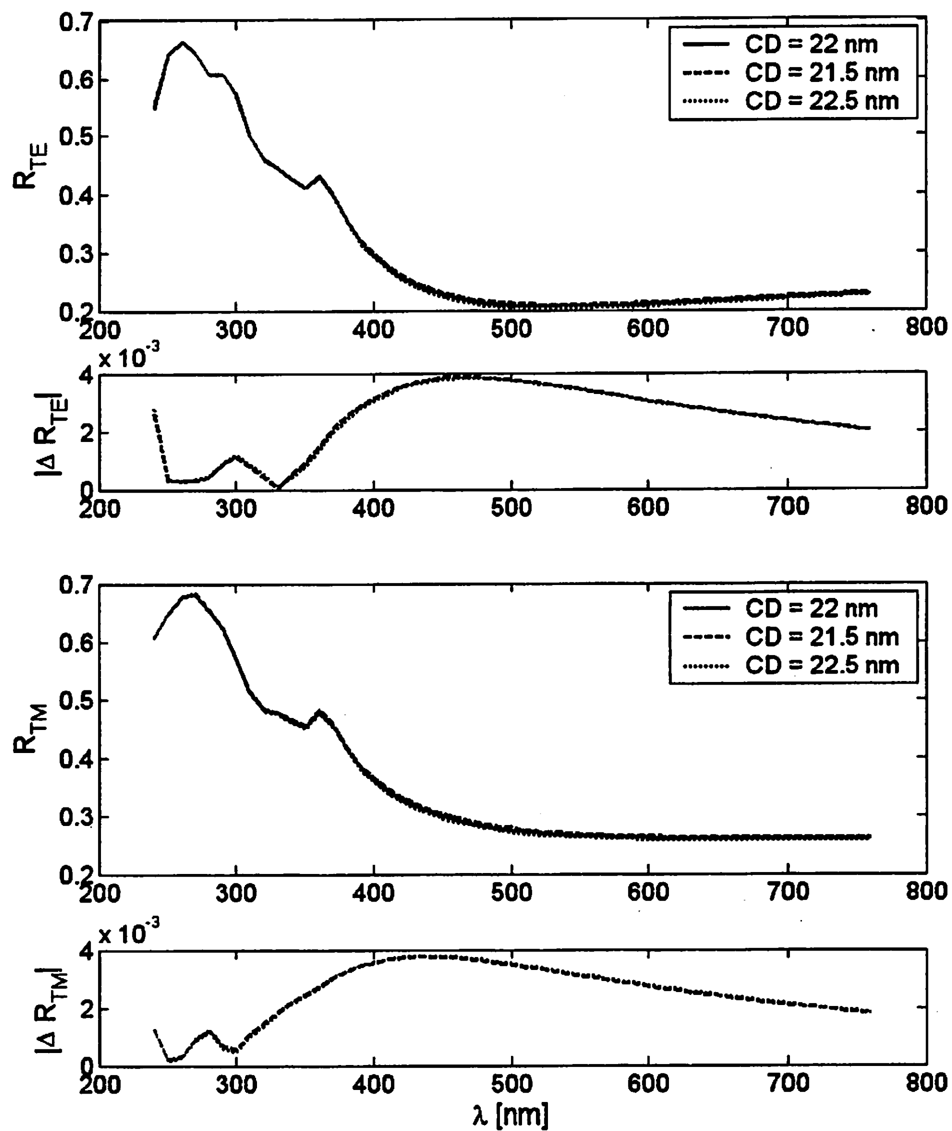

Figure 5.25: Polarization-sensitive reflectometer response for 22 nm node dense features and change in reflectometer response ($|\Delta R_{TE}|$ and $|\Delta R_{TM}|$) for CD change equivalent to required metrology tool 3σ precision.

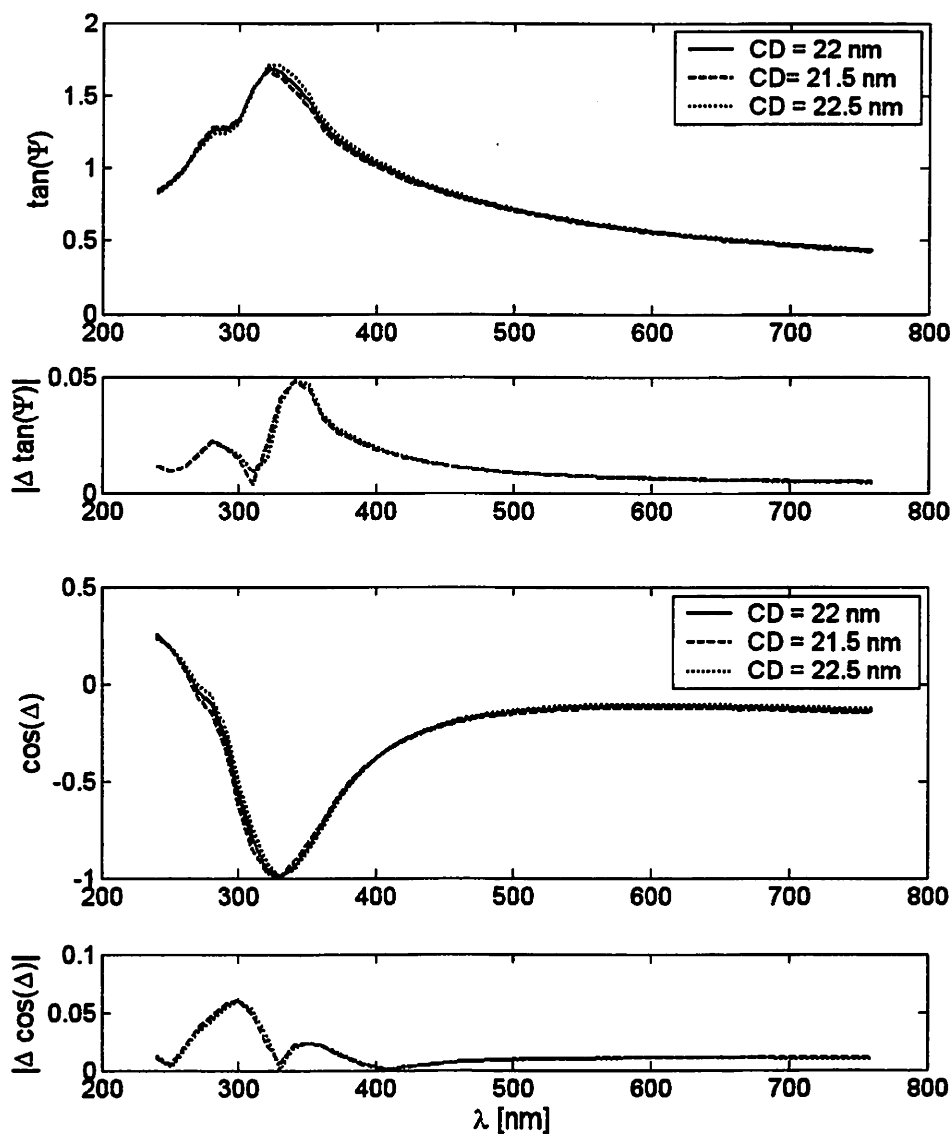

Figure 5.26: Spectroscopic ellipsometry response for 22 nm node dense features and change in ellipsometry response ($|\Delta \tan(\Psi)|$ and $|\Delta \cos(\Delta)|$ for CD change equivalent to required metrology tool 3σ precision.

For dense features at the 22 nm node, the reflectometry simulation results (Figure 5.24) show that detectable sensitivity levels exist above about 340 nm. The polarized reflectometry simulations (Figure 5.25) show sensitivity of a similar magnitude and over a similar spectral region to the unpolarized reflectometry results. The ellipsometry results (Figure 5.26) show good sensitivity virtually throughout the entire spectrum. The sensitivity levels are also higher than for either reflectometry technique.

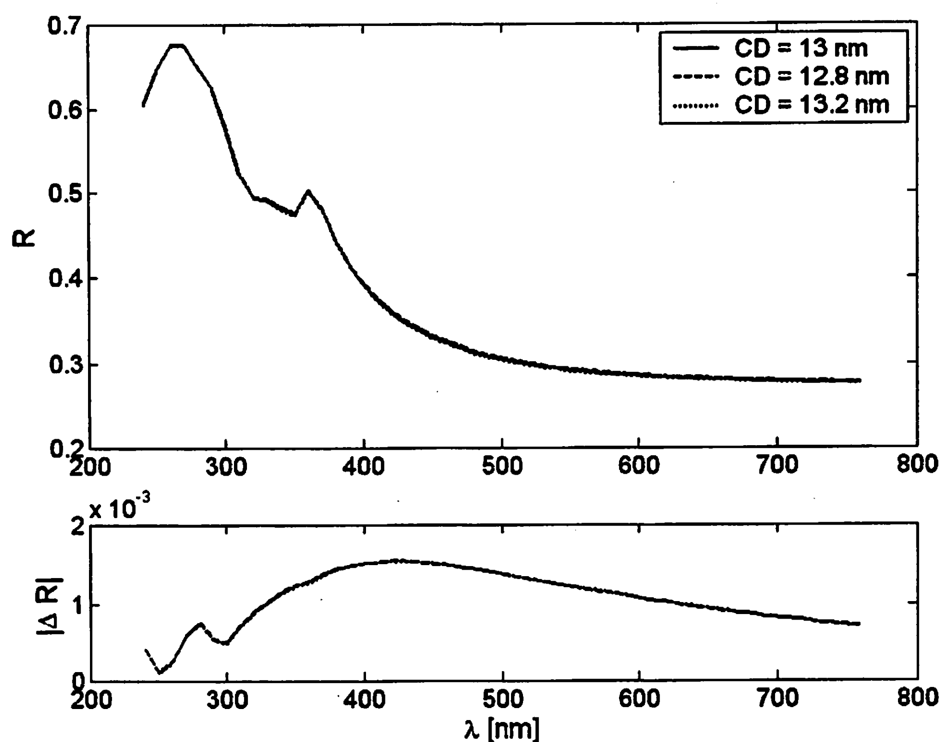

Figure 5.27: Reflectometer response for 22 nm node isolated features and change in reflectometer response ($|\Delta R|$) for CD change equivalent to required metrology tool 3σ precision.

For isolated features at the 22 nm node, the reflectometry simulation results (Figure 5.27) show that there may be a spectral region between about 320 nm and 600 nm in

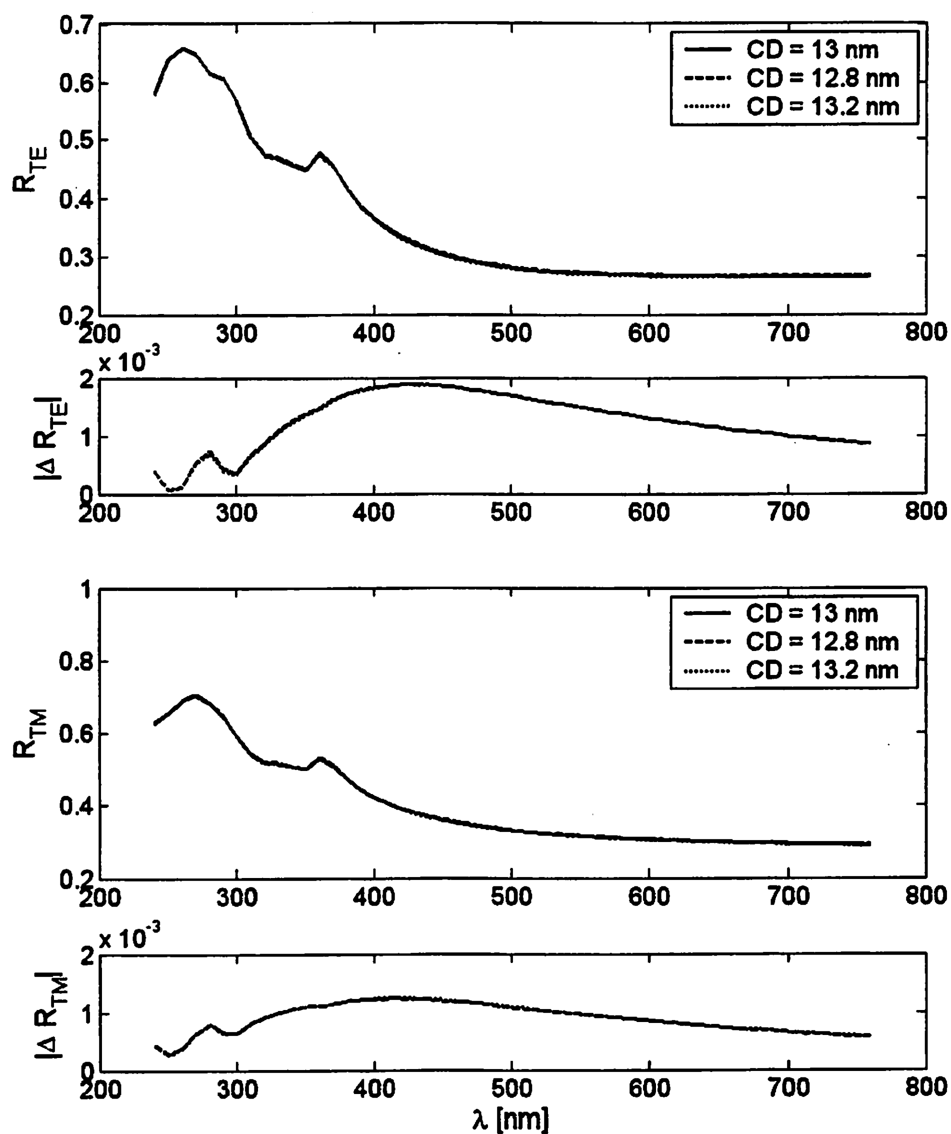

Figure 5.28: Polarization-sensitive reflectometer response for 22 nm node isolated features and change in reflectometer response ($|\Delta R_{TE}|$ and $|\Delta R_{TM}|$) for CD change equivalent to required metrology tool 3σ precision.

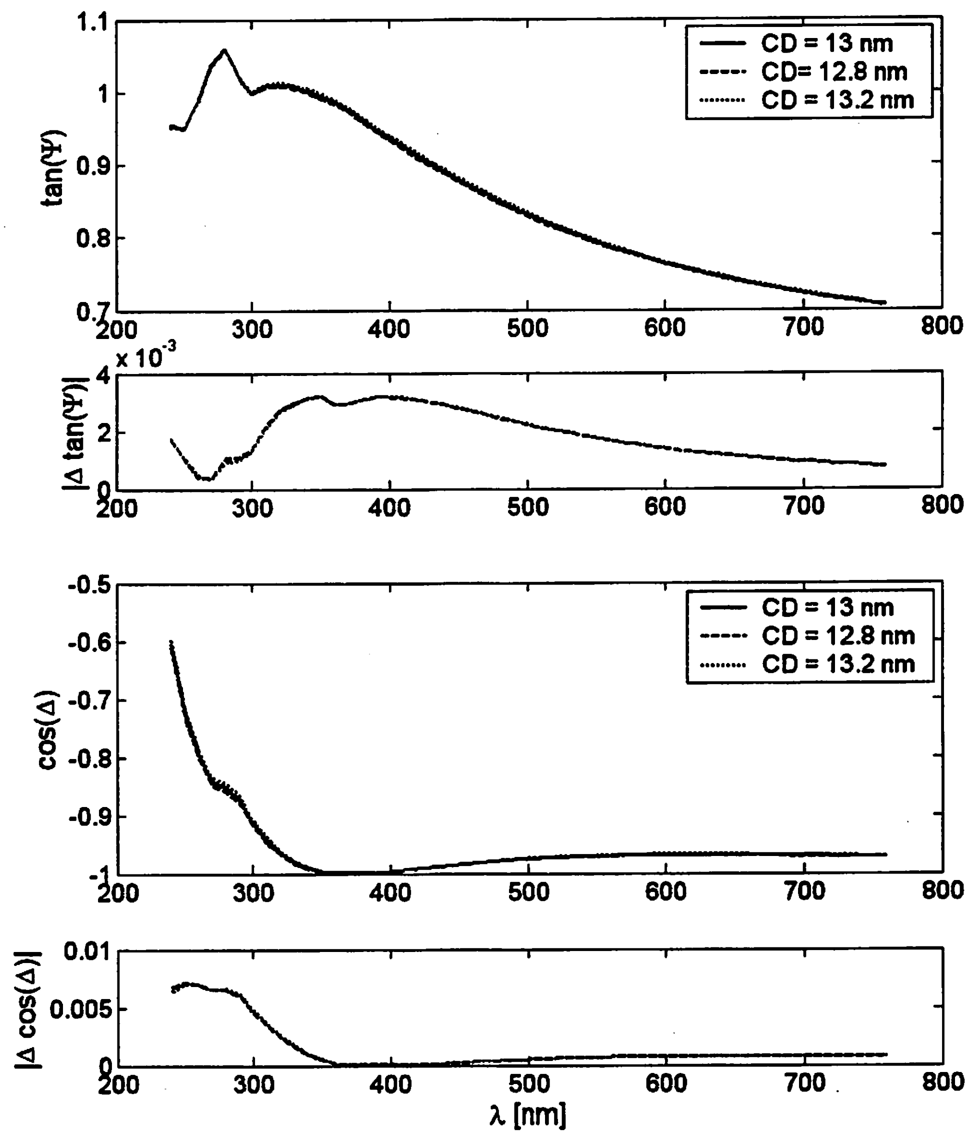

Figure 5.29: Spectroscopic ellipsometry response for 22 nm node isolated features and change in ellipsometry response ($|\Delta \tan(\Psi)|$ and $|\Delta \cos(\Delta)|$ for CD change equivalent to required metrology tool 3σ precision.

which the CD changes of the required precision level may be detectable if the noise limit of 10^{-3} is achieved here. The polarized reflectometry simulations (Figure 5.28) show slightly increased sensitivity compared with unpolarized reflectometry, and the sensitivity occurs over a similar wavelength range. Although the sensitivity levels for the ellipsometry results (Figure 5.29) are lower than for previous technology nodes, there appears to still be show good sensitivity virtually in the range of about 300 nm to 700 nm. The sensitivity levels are also higher than for either reflectometry technique.

In order to determine the region of greatest sensitivity for both wavelength and angle of incidence, gratings representing isolated features at the 22 nm node were simulated over a reasonable range for both parameters. This was done for both the nominal CD (13 nm) and for a CD deviation of 0.2 nm (corresponding to the required metrology precision for isolated lines at the 22 nm node). The absolute value of the difference between the two cases for the $\tan(\Psi)$ and $\cos(\Delta)$ signals is shown in Figures 5.30 and 5.31, respectively.

These results show that the sensitivity is greatest in the region of short wavelengths and high angles of incidence (*i.e.*, far from the normal). While there are obvious limitations to the angle of incidence which may be used, the wavelength may be decreased to some extent in an attempt to gain more sensitivity. It must be noted that material properties at wavelengths in the deep ultraviolet portion of the spectrum make measurements difficult due to absorption. Although spectroscopic ellipsometers which can operate down to 157 nm are currently available, these tools must operate in a purged atmosphere, making measurements more cumbersome and potential integration into other tools much more difficult.

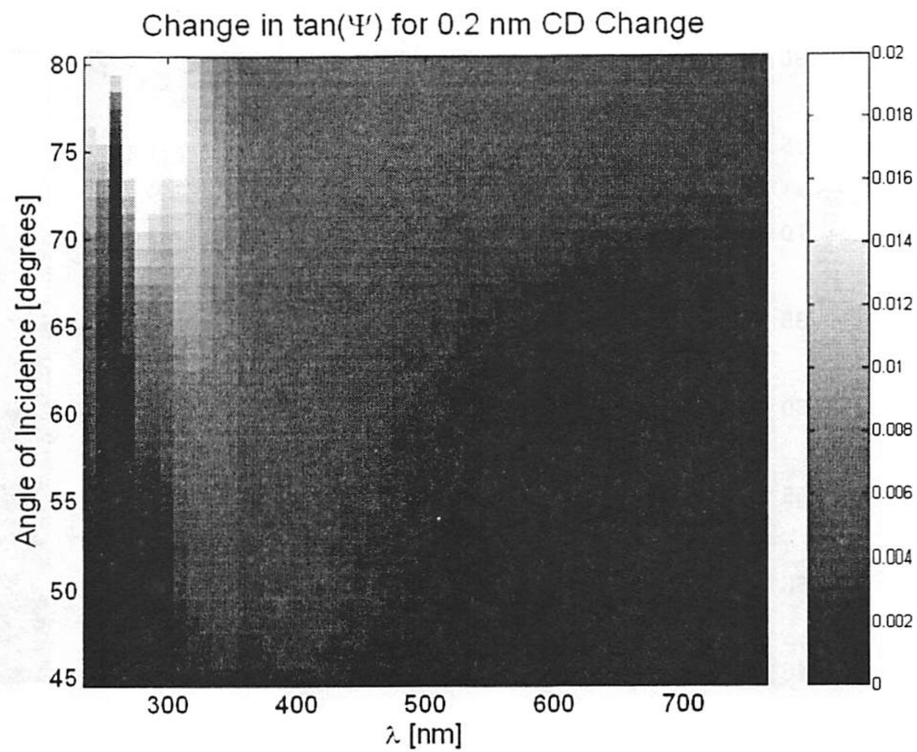

Figure 5.30: Change in $\tan(\Psi)$ for a 0.2 nm change in CD of a 13 nm line on 44 nm pitch as a function of wavelength and angle of incidence.

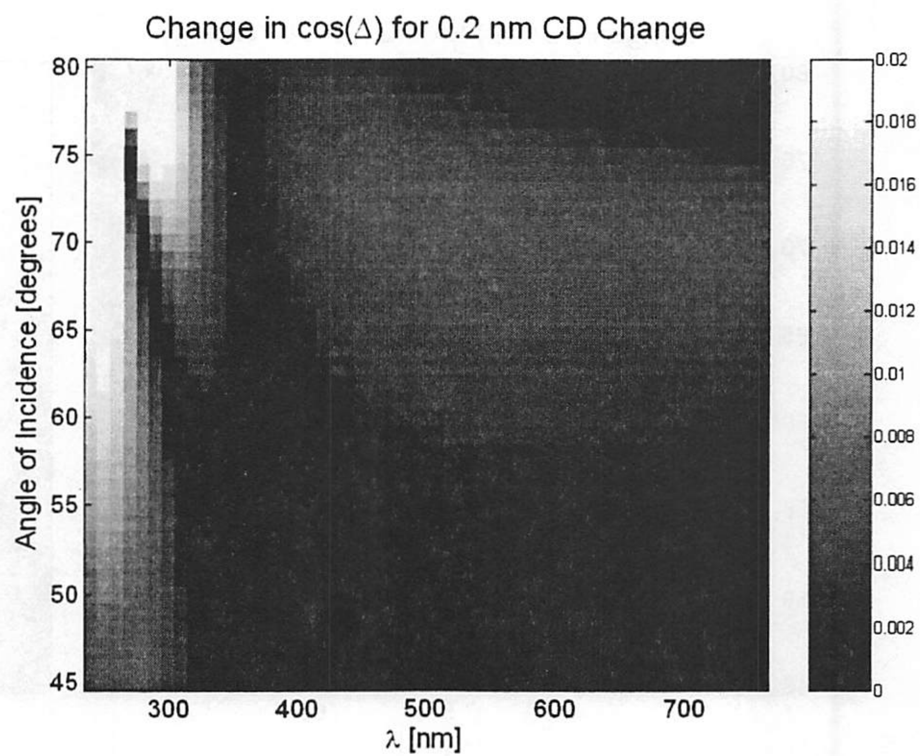

Figure 5.31: Change in $\cos(\Delta)$ for a 0.2 nm change in CD of a 13 nm line on 44 nm pitch as a function of wavelength and angle of incidence.

5.3 Conclusions

A simulation study was conducted to determine the suitability of three different types of scatterometry tools for CD metrology in future technology nodes. Grating parameter and metrology precision values were taken from the ITRS. The results show that while all three tool types (normal-incidence reflectometer, polarization-sensitive normal-incidence reflectometer, and spectroscopic ellipsometer) appear to have some sensitivity to CD variations on the order of metrology precision requirements, the width of the spectral region over which this sensitivity occurs decreases with reduced feature size. In addition, the sensitivity levels decrease in magnitude and move toward shorter wavelengths. Dense features show greater sensitivity than isolated features, and spectroscopic ellipsometery shows greater sensitivity than either polarized or unpolarized reflectometry.

Therefore, for future technology nodes, careful evaluation of the particular scatterometry application must be performed before selecting a hardware platform. For dense features where the CD variation levels and metrology precision requirements are less stringent, reflectometry techniques may be suitable. This is particularly attractive for integrated metrology applications because of the small footprint of reflectometers. However, for isolated features, where CD variation levels and metrology precision requirements are more demanding, spectroscopic ellipsometry may be required, especially at the 32 nm node and beyond.

Chapter 6

CD Error Budget Analysis for EUV Lithography

The preceding chapters have presented methods for characterizing key sources of critical dimension variation. In this chapter, the results of these experiments are brought together to form a preliminary CD error budget for the particular EUV lithography process under study. In addition, targets for improvement and requirements for production use of EUV lithography are discussed.

6.1 CD Sensitivity of Key Error Budget Components

There are two main types of error budget components: random and systematic. Random components include random dose and focus variation and metrology errors. Systematic components include across-field CD variation due to aberrations, flare, and illumination non-uniformity and across-wafer CD variation due to film thickness and post-exposure

bake temperature non-uniformity.

In general systematic components are very difficult to fit into a simple error budget analysis for two main reasons. First, the effect of these components on CD often interacts with other systematic or random components. An example of this is the effect of a given aberration on CD. The change in CD expected for a given aberration level is dependent upon focus for many aberrations. Therefore, it is impossible to

The particular EUV lithography system considered in this work exposes only a very small fraction of the total wafer area, so it does not make sense to consider across-wafer systematic variation. Therefore, variables such as PEB time and temperature may be taken as constant for the exposed area of a given wafer and treated as random variables. However, this is not the case in general, and across-wafer PEB temperature variations must be treated as systematic.

Random CD error budget components are shown in Table 6.1. The variation levels in some of these parameters is difficult to quantify. For example, in the case of PEB time variation, the level of variation is set by the consistency with which the operator of the plate is able to grab the wafer with wafer tweezers exactly as the bake time ends and move the wafer to the cooling plate. In these cases, the level of variation has been approximated.

The primary means of making CD measurements in this thesis was with an SEM. However, determining a single number for "metrology errors" is difficult. The preferred technique would be to measure the same feature many times and study the amount of variation present in the results. However, in the case of photoresist samples, this is complicated by the fact that the resist undergoes changes under exposure to the electron beam, such as

Table 6.1: Random components of the CD error budget for the MET system.

	CD Sensitivity	Parameter Variation	CD Variation
Dose	0.8 nm/%	1.5%	1.2 nm
Focus	Variable	approx. 100 nm	Variable
PEB time	0.3 nm/sec	approx. 1 sec	approx. 0.3 nm
PEB steady-state temp.	1.8 nm/°C	approx. 0.5 °C	approx. 0.9 nm
PEB ramp time	0.25 nm/sec	approx. 1 sec.	approx. 0.25 nm
Metrology errors	N/A	2 nm	N/A

Table 6.2: Projected values for random components of the CD error budget for a production-level EUV lithography tool. *Denotes value from 2004 International Roadmap for Semiconductors [40].

	CD Sensitivity	Parameter Variation	CD Variation
Dose	0.5 nm/%	1%	0.5 nm
Focus	Variable	approx. 75 nm	Variable
PEB time	0.3 nm/sec	approx. 0.5 sec	approx. 0.15 nm
PEB steady-state temp.	1 nm/°C*	approx. 0.2 °C	approx. 0.2nm
PEB ramp time	0.25 nm/sec	1 sec.	approx. 0.5 nm
Metrology errors	N/A	0.3 nm*	N/A

volume shrinkage and charging. Therefore, both the physical dimensions (line CD) and the measurement conditions (sample charging) are changing over time.

These same values were projected for future production EUV lithography tools in Table 6.2. Where noted, values were taken from the ITRS (2004 update) for the 32 nm node (MPU features). Other values were extrapolated from current state-of-the-art.

6.2 Interaction Effects on Process Window

The concept of a "process window" is a useful one in lithography applications. A process window is basically the range of input parameters (dose, focus, etc.) which will produce an output metric (e.g., CD) which meets the required specifications. The most

common process window refers to the range of dose and focus values which will produce a CD which falls within a given specification. Several factors may interact to cause a reduction in the overall size of the process window, meaning that less variation in the input parameters can be tolerated before the output goes out of spec. Examples include the effect of aberrations and flare in the projection optics of the lithography tool. Therefore, it is difficult to assign a single "CD sensitivity" number to these sources of variation. However, studying the cumulative effect of these sources of variation on the process window may be helpful.

In order to project this kind of process window analysis for the 32 nm node, wavefront data for a previous-generation EUV projection optic with a circular pupil was obtained [36]. This wavefront data was scaled to have an RMS variation of 0.25 nm, a reasonable value for the 32 nm node, and is shown in Figure 6.1. Note that the MET wavefront data was not chosen because it is an annular optic, a design unlikely to be used in a production tool. Aerial image simulations were then performed with this data to determine the effect of such aberrations on the process window. These aerial image simulations assumed parameters for MPU features from the ITRS (2004 Update) [40]. The nominal CD was 18 nm on a 64 nm pitch. The total allowable CD variation for these features is 1.2 nm (3σ). The process windows for both the aberrated and unaberrated cases are shown in Figure 6.2. In this particular case the aberrations have a relatively small effect on the process window. This is undoubtedly due to the very low levels of wavefront variance (0.25 nm RMS) assumed in the simulations.

Of course, the lithography process may not be allowed to consume the entire

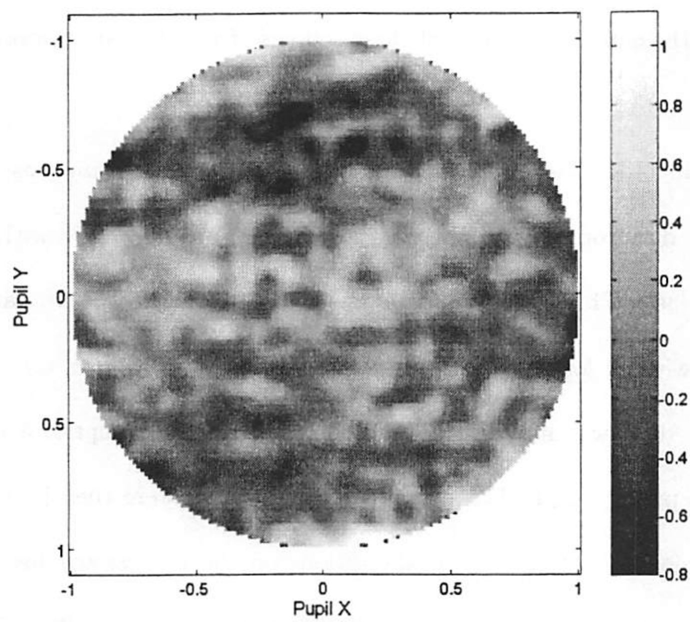

Figure 6.1: Wavefront data for an EUV projection optic with a circular pupil [36] scaled to have an RMS variation of 0.25 nm. Color axis is in units of nm.

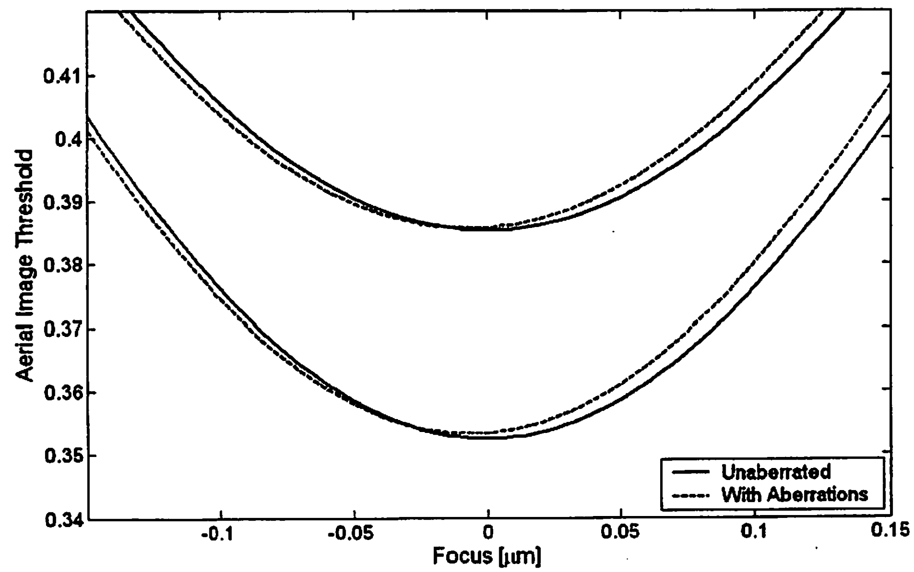

Figure 6.2: Effect of aberrations on the CD process window for 18 nm lines on a 64 nm pitch based on aerial image simulation. Process window is 18 ± 1.1 nm as defined by ITRS specification for MPU features at the 32 nm node (total 3σ CD variation of 1.2 nm).

error budget. The ITRS allocates 4/5 of the total CD variation to lithography for MPU features [40]. The process window for both the entire CD error budget and the error budget component allocated to lithography is shown in Figure 6.3. Note that this restriction excludes all other sources of variation outside of lithography, including etch and metrology. This is a somewhat significant decrease in the size of the process window.

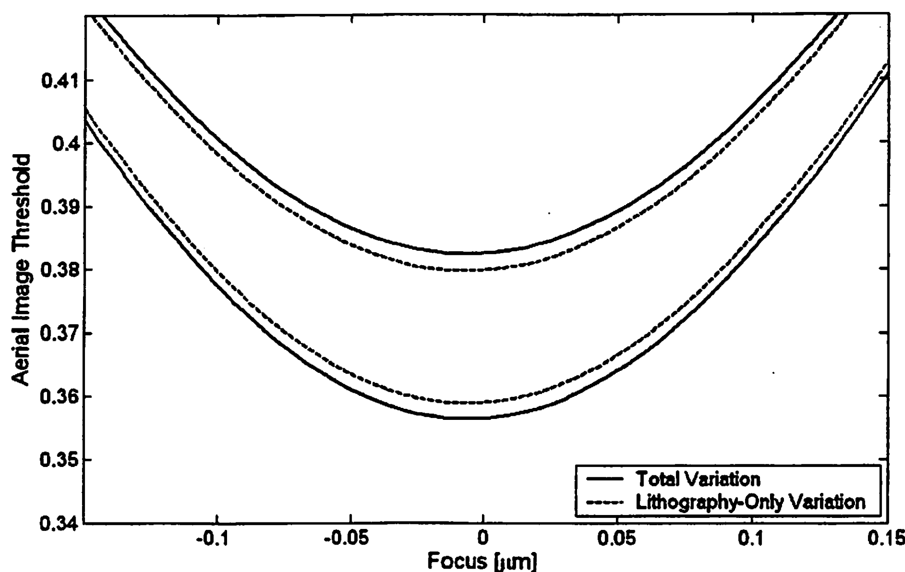

Figure 6.3: Comparison of CD process windows for 18 nm lines on a 64 nm pitch based on aerial image simulation including appropriately-scaled aberrations. Solid curve shows process window of 18 ± 1.1 nm as defined by ITRS specification for MPU features at the 32 nm node (total 3σ CD variation of 1.1 nm). Dashed curve shows process window restricted to variation from lithography only (assumed to be 4/5 total variation by ITRS [40]). This excludes variation from etch and metrology.

Finally, the process window for sources of variation outside of the exposure process is studied. Here the random sources of variation related to post-exposure bake shown in Table 6.2 are removed from the process window by subtracting their contribution to the total CD error budget from the CD specifications. This represents the portion of the error

budget "consumed" by the PEB process. The results are shown in Figure 6.4. In this case there is almost no remaining process window available for dose and focus variation. As it is unrealistic to expect such tight levels of control over these parameters, it is likely that improvements elsewhere will be required.

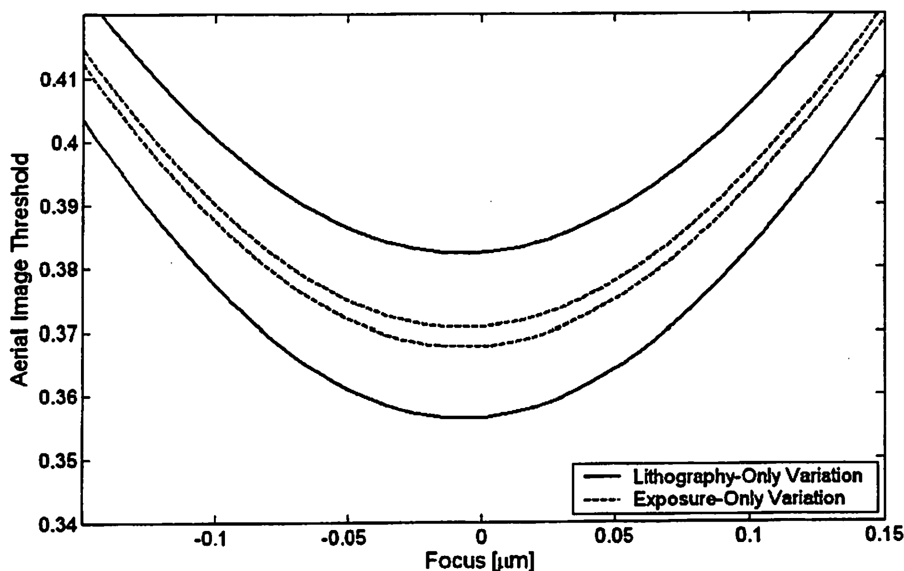

Figure 6.4: Comparison of CD process windows for 18 nm lines on a 64 nm pitch based on aerial image simulation including appropriately-scaled aberrations. Solid curve shows process window for all variation from lithography (4/5 total CD variation). Dashed curve shows process window restricted to exposure process only (variation due to PEB is removed according to values specified in Table 6.2). Very little process latitude remains.

6.3 Critical Issues for the Future of EUV Lithography

Although great progress has been made in EUV lithography research and development, there are some areas which still need to be addressed. The areas which most directly affect control of CD variation are related to optics, resists, and metrology.

With regard to optics, the amount of flare present in production EUVL systems will most likely need to be reduced below the level measured in the MET system. In addition, improvement in the level of key aberrations may be required to achieve suitable performance.

The photoresists studied in this work appear to have reasonable levels of CD sensitivity to PEB parameter variation. The sensitivity to steady-state PEB temperature will need to be slightly improved to meet the levels specified by the ITRS roadmap for the 32 nm technology node (1 nm/°C). This will be a difficult challenge to meet given the simultaneous objective of increased resist sensitivity in order to meet throughput requirements. Currently there appears to be no specification for CD sensitivity to PEB ramp time. As this is the portion of the PEB process during which the bake plate temperature non-uniformity is greatest, it appears that this is an additional process parameter which should be monitored and controlled. The most critical issue for resist development appears to be resolution. The large difference between the expected contrast transfer function (CTF) based on optical modeling and the CTF measured in resist (Section 3.3) indicates that the resist is still the limiting factor in determining the overall resolution of the MET system.

Scatterometry has been shown to have the potential to measure CD variation with the precision required by the ITRS roadmap for several future technology nodes. However, there are still challenges in making this technology viable for manufacturing use at these feature sizes. Detectors which can measure with the required precision and still meet speed requirements for throughput are essential. In addition, methods for correlating scatterometry measurements (which are typically based on grating structures placed in the

scribe line between chips) with the features within the chip itself will be required.

Chapter 7

Conclusions

7.1 Summary

The demand for integrated circuits in all manner of electronic devices is likely to continue to increase for the foreseeable future. In order to meet this demand for high performance, low power devices, critical feature sizes such as transistor gate lengths will continue to decrease. Extreme ultraviolet lithography is a potential enabling technology as these feature sizes decrease to 30 nm and beyond.

In this dissertation, several of the important process characteristics affecting the manufacturability of an EUV lithography process were examined. This includes the characterization of the projection optics with regard to flare and aberrations. Resist-based methods were used to measure the flare and certain low-order aberrations. In addition, the contrast-transfer function (CTF) was used as a method for evaluating the performance of a complete lithography process, taking into account both the limitations of the optics and photoresist.

The critical dimension sensitivity to variation in several key post-exposure bake parameters was also studied for EUV photoresists. This involved the use of temperature sensor wafers to accurately measure the temperature profile seen by the wafer. A simple resist development model based upon a resist point spread function (PSF) was used, and with the addition of a "DC" term, was found to provide good agreement with the measured CTF results.

Optical CD metrology based on scatterometry was studied as a potential metrology solution for future technology nodes. Three scatterometry hardware types were compared: reflectometers, polarized reflectometers, and spectroscopic ellipsometers. Although all three tool types are suitable for dense features (such as those found in DRAM architectures) in the near term, the superior sensitivity of spectroscopic ellipsometry may make it the only viable option in future technology nodes, and in the relatively near term for the case of isolated features.

Finally, the components of the critical dimension error budget measured in this dissertation were combined and discussed. In addition, the effect of certain key components on the process window were addressed. Future requirements for production use of EUV lithography systems were described.

7.2 Future Work

There is a great deal of work left to be done on EUV lithography in order to bring it to production use. Continued improvement in the optical quality, in terms of both aberrations and flare, will be required, and further refinement of resist-based methods

for characterizing these parameters will need to be developed. This could include the implementation and testing of the interferometric aberrometry method proposed in Section 3.5.

Further resist development is essential. Current EUV lithography resolution is limited by the resist rather than the optics. In addition, photoresists for EUV technology will need to meet extremely demanding specifications in terms of sensitivity, line edge roughness (LER), PEB temperature sensitivity, etch resistance, and resolution.

There is much work to be done in the realm of CD metrology. Although a simple sensitivitiy study here showed that optical metrology, particularly spectroscopic ellipsometry, may have the potential to be a viable option for several successive technology nodes, further work is required to ensure that the required detection limits will be met. In addition, the possibility exists that transistors in the sub-20 nm regime may be significantly different in structure from the planar architectures of today. Metrology capabilities to measure all of the relevant parameters of such devices will need to be developed. Also, metrology for two-dimensional aspects of features such as line-end shortening and line edge roughness needs improvement.

Of course, semiconductor manufacturers are not interested in the patterning of resist lines except as a means to an end, namely, the fabrication of functional electronic devices. As this work has focused entirely on the lithography process, there is certainly room to extend it to subsequent steps such as the etching process used to transfer the resist pattern into underlying film layers. This brings with it a host of challenges. Although EUV lithography technology holds promise as a next-generation lithography candidate, meeting

the challenges remaining while keeping costs under control will be critical.

References

[1] G. E. Moore, "Cramming more components onto integrated circuits," *Electronics* **38**, April 19 1965.

[2] J. H. Bruning, "Optical lithography: Thirty years and three orders of magnitude," in *Advances in Resist Technology and Processing XIV*, R. G. Tarascon-Auriol, ed., *Proc. SPIE* **3049**, pp. 14–27, 1997.

[3] G. E. Moore, "Lithography and the future of Moore's law," in *Optical/Laser Microlithography VIII*, T. A. Brunner, ed., *Proc. SPIE* **2440**, pp. 2–17, 1995.

[4] J. R. Sheats and B. W. Smith, eds., *Microlithography: Science and Technology*, Marcel Dekker, Inc., New York, 1998.

[5] P. Rai-Choudhury, ed., *Handbook of Microlithography, Micromachining, and Microfabrication*, SPIE Optical Engineering Press, Bellingham, WA, 1997.

[6] H. J. Levinson, *Principles of Lithography*, SPIE Press, Bellingham, WA, 2001.

[7] A. J. den Dekker and A. van den Bos, "Resolution: A survey," *J. Opt. Soc. Am. A* **14**, pp. 547–557, March 1997.

[8] B. W. Smith, "Optics for photolithography," in Sheats and Smith [4], pp. 171–270.

[9] A. K.-K. Wong, *Resolution Enhancement Techniques in Optical Lithography*, SPIE Press, Bellingham, WA, 1990.

[10] T. A. Brunner, N. Seong, W. D. Hinsberg, J. A. Hoffnagle, F. A. Houle, and M. I. Sanchez, "High NA lithographic imagery at Brewster's angle," in Yen [93], pp. 1–10.

[11] M. Born and E. Wolf, *Principles of Optics*, Cambridge University Press, Cambridge, UK, seventh ed., 1999.

[12] J. P. Cain, "Characterization of systematic spatial variation in photolithography," Master's thesis, University of California, Berkeley, Dec. 2002.

[13] J. E. Bjorkholm, "EUV lithography–the successor to optical lithography?," *Intel Technology Journal* , 3rd quarter 1998.

[14] T. E. Jewell, J. M. Rodgers, and K. P. Thompson, "Reflective systems design study for soft x-ray projection lithography," *J. Vac. Sci. Technol. B* **8**, pp. 1519–1523, Nov./Dec. 1990.

[15] D. Attwood, *Soft X-Rays and Extreme Ultraviolet Radiation*, Cambridge University Press, Cambridge, 1999.

[16] T. W. Barbee, Jr., S. Mrowka, and M. C. Hettrick, "Molybdenum-silicon multilayer mirrors for the extreme ultraviolet," *Applied Optics* **24**, pp. 883–886, Mar. 15 1985.

[17] Center for X-Ray Optics, Lawrence Berkeley National Lab. `http://www-cxro.lbl.gov/optical_constants/`.

[18] A. K. Ray-Chaudhuri, S. E. Gianoulakis, P. A. Spence, M. P. Kanouff, and C. D. Moen, "Impact of thermal and structural effects on EUV lithographic performance," in Vladimirsky [94], pp. 124–132.

[19] P. yang Yan, G. Zhang, P. Kofron, J. Chow, A. Stivers, E. Tejnil, G. Cardinale, and P. Kearney, "EUV mask patterning approaches," in Vladimirsky [95], pp. 309–313.

[20] P. Mangat, S. Hector, S. Rose, G. Cardinale, E. Tejnil, and A. Stivers, "EUV mask fabrication with Cr absorber," in Dobisz [96], pp. 76–82.

[21] S. P. Vernon, P. A. Kearney, W. M. Tong, S. Prisbrey, C. Larson, C. E. Moore, F. W. Weber, G. Cardinale, P.-Y. Yan, and S. D. Hector, "Masks for extreme ultraviolet lithography," in *BACUS Symposium on Photomask Technology and Management*, B. J. Grennon and F. E. Abboud, eds., *Proc. SPIE* **3546**, pp. 184–193, 1998.

[22] P. yang Yan, C. wei Lai, and G. Cardinale, "EUV mask contact layer defect printability and requirement," in Dobisz [96], pp. 508–514.

[23] S. D. Hector, "EUVL masks: Requirements and potential solutions," in Engelstad [97], pp. 134–149.

[24] T. Liang and A. Stivers, "Damage-free mask repair using electron beam induced chemical reactions," in Engelstad [97], pp. 375–384.

[25] S. Burkhart, C. Cerjan, P. Kearney, P. Mirkarimi, and C. Walton, "Low-defect reflective mask blanks for extreme ultraviolet lithography," in Vladimirsky [95], pp. 570–577.

[26] N. A. Beaudry and T. D. Milster, "Effects of mask roughness and condenser scattering in EUVL systems," in Vladimirsky [95], pp. 653–662.

[27] T. Pistor and A. R. Neureuther, "Calculating aerial images from EUV masks," in Vladimirsky [95], pp. 679–696.

[28] V. Banine and R. Moors, "Extreme ultraviolet sources for lithography applications," in Dobisz [98], pp. 203–214.

[29] G. D. Kubiak, L. J. Bernardez, and K. Krenz, "High-power extreme ultraviolet source based on gas jets," in Vladimirsky [94], pp. 81–89.

[30] G. D. Kubiak, L. J. Bernardez, K. Krenz, and W. C. Sweatt, "Scale-up of a cluster jet laser plasma source for extreme ultraviolet lithography," in Vladimirsky [95], pp. 669–678.

[31] L. Rymell, M. Berglund, B. A. M. Hansson, and H. M. Hertz, "X-ray and EUV laser-plasma sources based on cryogenic liquid-jet target," in Vladimirsky [95], pp. 421–424.

[32] W. T. Silfvast, M. Klosner, G. Shimkaveg, and H. Bender, "High-power plasma discharge source at 13.5 nm and 11.4 nm for EUV lithography," in Vladimirsky [95], pp. 272–275.

[33] N. R. Fornaciari, H. Bender, D. Buchenauer, J. Dimkoff, M. Kanouff, S. Karim, C. Romeo, G. Shimkaveg, W. T. Silfvast, and K. D. Stewart, "Power scale-up of the extreme ultraviolet electric capillary discharge souce," in Engelstad [97], pp. 110–121.

[34] R. Lebert, K. Bergmann, L. Juschkin, O. Rosier, and W. Neff, "Comparison of different source concepts for EUVL," in Dobisz [98], pp. 215–225.

[35] K. Ota, K. Murakami, H. Kondo, T. Oshino, K. Sugisaki, and H. Komatsuda, "Feasibility study of EUV scanners," in Dobisz [98], pp. 60–68.

[36] P. Naulleau, K. A. Goldberg, E. H. Anderson, P. Batson, P. Denham, K. Jackson, S. Rekawa, and J. Bokor, "Adding static printing capabilities to the euv phase-shiftin point diffraction interferometer," in Dobisz [98], pp. 639–645.

[37] P. Naulleau, K. A. Goldberg, E. H. Anderson, D. Attwood, P. Batson, J. Bokor, P. Denham, E. Gullikson, B. Harteneck, B. Hoef, K. Jackson, D. Olynick, S. Rekawa, F. Salmassi, K. Blaedel, H. Chapman, L. Hale, P. Mirkarimi, R. Soufli, E. Spiller, D. Sweeney, J. Taylor, C. Walton, D. O'Connell, D. Tichenor, C. W. Gwyn, P.-Y. Yan, and G. Zhang, "Sub-70 nm extreme ultraviolet lithography at the Advanced Light Source static microfield exposure station using the engineering test stand set-2 optic," *J. Vac. Sci. Technol. B* **20**, pp. 2829–2833, Nov./Dec. 2002.

[38] D. T. Attwood, P. Naulleau, K. A. Goldberg, E. Tejnil, C. Chang, R. Beguiristain, P. Batson, J. Bokor, E. M. Gullikson, M. Koike, H. Medecki, and J. H. Underwood, "Tunable coherent radiation in the soft x-ray and extreme ultraviolet spectral regions," *IEEE J. Quantum Elect.* **35**, pp. 709–720, May 1999.

[39] P. P. Naulleau, K. A. Goldberg, P. Batson, J. Bokor, P. Denham, and S. Rekawa, "Fourier-synthesis custom-coherence illuminator for extreme ultraviolet microfield lithography," *Applied Optics* **42**, pp. 820–826, February 2003.

[40] International Technology Roadmap for Semiconductors. `http://public.itrs.net`, 2003.

[41] J. W. Goodman, *Introduction to Fourier Optics*, McGraw Hill, Boston, MA, second ed., 1996.

[42] F. Zernike, "Diffraction theory of the knife-edge test and its improved form, the phase-contrast method," *Mon. Not. R. Astron. Soc.* **94**, pp. 377–384, 1934. Reprinted in *J. Microlith., Microfab., Microsys.* , **1**, pp. 87–94, July 2002.

[43] V. N. Mahajan, "Zernike circle polynomials and optical aberrations of systems with circular pupils," *Appl. Optics* **33**, pp. 8121–8124, Dec. 1994.

[44] J. C. Wyant and K. Creath, "Basic wavefront aberration theory for optical metrology," in *Applied Optics and Optical Engineering*, R. Shannon and J. Wyant, eds., **XI**, pp. 28–39, Academic Press, Inc., New York, 1992.

[45] V. N. Mahajan, "Zernike annular polynomials for imaging systems with annular pupils," *J. Opt. Soc. Am.* **71**, pp. 75–85, Jan. 1981.

[46] V. N. Mahajan, "Zernike annular polynomials for imaging systems with annular pupils," *J. Opt. Soc. Am. A* **1**, p. 685, June 1984.

[47] V. N. Mahajan, "Zernike annular polynomials and optical aberrations of systems with annular pupils," *Appl. Optics* **33**, pp. 8125–8127, Dec. 1994.

[48] C. Krautschik, M. Ito, I. Nishiyama, and S. Okazaki, "Impact of EUV light scatter on CD control as a result of mask density changes," in Engelstad [97], pp. 289–301.

[49] A. Bourov, L. C. Litt, and L. Zavyalova, "Impact of flare on CD variation for 248nm and 193nm lithography systems," in Progler [99], pp. 1388–1393.

[50] L. C. Litt, A. Bourov, B. LaFontaine, and E. Apelgren, "Evaluation and characterization of flare in ArF lithography," in Yen [93], pp. 1442–1452.

[51] S. H. Lee, P. Naulleau, C. Krautschik, M. Chandhok, H. N. Chapman, D. J. O'Connell, and M. Goldstein, "Lithographic flare measurements of EUV full-field projection optics," in Engelstad [100], pp. 103–111.

[52] M. Chandhok, S. H. Lee, C. Krautschik, B. J. Rice, E. Panning, M. Goldstein, and M. Shell, "Determination of the flare specification and methods to meet the CD control requirements for the 32 nm node using EUVL," in Mackay [101], pp. 86–95.

[53] J. C. Stover, *Optical Scattering Measurement and Analysis*, SPIE Optical Engineering Press, Bellingham, WA, second ed., 1995.

[54] K. Lai, C. hsi Wu, and C. Progler, "Scattered light: The increasing problem for 193nm exposure tools and beyond," in Progler [99].

[55] C. Krautschik, M. Chandhok, G. Zhang, S. Lee, M. Goldstein, E. Panning, R. Bristol, and V. Singh, "Implementing flare compensation for EUV masks through localized mask CD resizing," in Engelstad [100], pp. 58–68.

[56] E. Spiller, D. Stearns, and M. Krumrey, "Multilayer X-ray mirrors: Interfacial roughness, scattering, and image quality," *J. Appl. Phys.* **74**, pp. 107–118, 1 July 1993.

[57] D. G. Stearns, D. P. Gaines, D. W. Sweeney, and E. M. Gullikson, "Nonspecular X-ray

scattering in a multilayer-coated imaging system," *J. Appl. Phys.* **84**, pp. 1003–1028, 15 July 1998.

[58] E. M. Gullikson, S. Baker, J. E. Bjorkholm, J. Bokor, K. A. Goldberg, J. E. M. Goldsmith, C. Montcalm, P. Naulleau, E. Spiller, D. G. Stearns, J. S. Taylor, and J. H. Underwood, "EUV scattering and flare of 10x projection cameras," in Vladimirsky [95], pp. 717–723.

[59] E. M. Gullikson, "Scattering from normal incidence EUV optics," in Vladimirsky [94], pp. 72–80.

[60] P. Naulleau, K. A. Goldberg, E. M. Gullikson, and J. Bokor, "Interferometric at-wavelength flare characterization of extreme ultraviolet optical systems," *J. Vac. Sci. Technol. B* **17**, pp. 2987–2991, Nov./Dec. 1999.

[61] P. Naulleau, K. A. Goldberg, E. M. Gullikson, and J. Bokor, "At-wavelength, system-level flare characterization of extreme-ultraviolet optical systems," *Applied Optics* **39**, pp. 2941–2947, 10 June 2000.

[62] M. Chandhok, S. H. Lee, C. Krautschik, G. Zhang, B. J. Rice, M. Goldstein, E. Panning, R. Bristol, A. Stivers, and M. Shell, "Comparison of techniques to measure the point spread function due to scatter and flare in EUV lithography systems," in Mackay [101], pp. 854–860.

[63] G. E. Sommargren, D. W. Phillion, M. A. Johnson, N. Q. Nguyen, A. Barty, F. J. Snell, D. R. Dillon, and L. S. Bradsher, "100-picometer interferometry for EUVL," in Engelstad [97], pp. 316–328.

[64] H. Medecki, E. Tejnil, K. A. Goldberg, and J. Bokor, "Phase-shifting point diffraction interferometer," *Optics Letters* **21**, pp. 1526–1528, Oct. 1 1996.

[65] K. A. Goldberg, P. Naulleau, P. Denham, S. B. Rekawa, K. Jackson, E. H. Anderson, J. A. Liddle, and J. Bokor, "EUV interferometry of the 0.3 NA MET optic," in Engelstad [100], pp. 69–74.

[66] K. A. Goldberg, P. Naulleau, P. Denham, S. B. Rekawa, K. Jackson, J. A. Liddle, B. Harteneck, E. Gullikson, and E. H. Anderson, "Preparations for extreme ultraviolet interferometry of the 0.3 numerical aperture Micro Exposure Tool optic," *J. Vac. Sci. Technol. B* **21**, pp. 2706–2710, Nov./Dec. 2003.

[67] K. A. Goldberg, P. Naulleau, P. Denham, S. B. Rekawa, K. Jackson, J. A. Liddle, and E. H. Anderson, "Emerging lithographic technologies VIII," in Mackay [101], pp. 64–73.

[68] K. A. Goldberg, P. Naulleau, P. Denham, S. B. Rekawa, K. Jackson, E. H. Anderson, and J. A. Liddle, "At-wavelength alignment and testing of the 0.3 NA MET optic," *J. Vac. Sci. Technol. B* **22**, Nov./Dec. 2004.

[69] J. P. Kirk, "Scattered light in photolithographic lenses," in *Optical/Laser Microlithography VII*, T. A. Brunner, ed., *Proc. SPIE* **2197**, pp. 566–572, 1994.

[70] E. M. Gullikson. private communication, 2004.

[71] S. H. Lee, D. A. Tichenor, and P. Naulleau, "Lithographic aerial-image contrast measurement in the extreme ultraviolet Engineering Test Stand," *J. Vac. Sci. Technol. B* **20**, pp. 2849–2852, Nov./Dec. 2002.

[72] A. Grassman and H. Moritz, "Contrast transfer function measurements of deep ultraviolet steppers," *J. Vac. Sci. Technol. B* **10**, pp. 3008–3011, Nov./Dec. 1992.

[73] J. A. Hoffnagle, W. D. Hinsberg, M. I. Sanchez, and F. A. Houle, "Method of measuring the spatial resolution of a photoresist," *Optics Letters* **27**, pp. 1776–1778, 15 October 2002.

[74] PROLITH, KLA-Tencor Corporation. `http://www.kla-tencor.com`.

[75] G. M. Wallraff, D. R. Medeiros, M. Sanchez, K. Petrillo, W. Huang, C. Rettner, B. Davis, C. E. Larson, L. Sundberg, P. J. Brock, W. D. Hinsberg, F. A. Houle, J. A. Hoffnagle, D. Goldfarb, K. Temple, S. Wind, and J. Bucchignano, "Sub-50 nm half-pitch imaging with a low activation energy chemically amplifed photoresist," *J. Vac. Sci. Technol. B* **22**, pp. 3479–3484, Nov./Dec. 2004.

[76] M. V. Williamson, *Enhanced, Quantitiative Analysis of Resist Image Contrast Upon Line Edge Roughness (LER).* PhD thesis, University of California, Berkeley, 2003.

[77] SEM Metrology Interactive Toolbox (SuMMIT), EUV Technology, SuMMIT Software Division. `http://www.euvl.com/summit`.

[78] T. A. Brunner, "Impact of lens aberrations on optical lithography," *IBM Journal of Research and Development* **41**, pp. 57–67, Jan./Mar. 1997.

[79] A. Brunton, J. Cahsmore, P. Elbourn, G. Elliner, M. Gower, P. Grünewald, M. Harman, S. Hough, N. McEntee, S. Mundair, D. Rees, P. Richards, V. Truffert, I. Wallhead, and M. Whitfield, "High-resolution EUV microstepper tool for resist testing and technology evaluation," in Mackay [101], pp. 869–880.

[80] H. Ito, C. G. Wilson, and J. M. J. Fréchet, "New UV resists with negative or positive tone," in *Digest of Technical Papers of 1982 Symposium on VLSI Technology*, pp. 86–87.

[81] H. Ito and C. G. Wilson, "Chemical amplification in the design of dry developing resist materials," in *Technical Papers of SPE Regional Technical Conference on Photopolymers*, pp. 331–353, 1982.

[82] H. Ito, "Chemical amplification resists: History and development within IBM," *IBM Journal of Research and Development* **44**, pp. 119–130, Jan./March 2000.

[83] M. Freed, M. Krüger, C. J. Spanos, and K. Poolla, "Autonomous on-wafer sensors for process monitoring, diagnosis, and control," *IEEE Trans. Semiconduct. Manufact.* **14**, pp. 255–264, Aug. 2001.

[84] P. P. Naulleau, "Verification of point-spread-function-based modeling of an extreme-ultraviolet photoresist," *Applied Optics* **43**, pp. 788–792, February 2004.

[85] M. G. Moharam and T. K. Gaylord, "Coupled-wave analysis of reflection gratings," *Applied Optics* **20**, pp. 240–244, 15 January 1981.

[86] M. G. Moharam and T. K. Gaylord, "Rigorous coupled-wave analysis of planar-grating diffraction," *J. Opt. Soc. Am.* **71**, pp. 811–818, July 1981.

[87] M. G. Moharam and T. K. Gaylord, "Diffraction analysis of dielectric surface-relief gratings," *J. Opt. Soc. Am.* **72**, pp. 1385–1392, Oct. 1982.

[88] M. G. Moharam and T. K. Gaylord, "Comments on analyses of reflection gratings," *J. Opt. Soc. Am.* **73**, pp. 399–401, March 1983.

[89] M. G. Moharam and T. K. Gaylord, "Rigorous coupled-wave analysis of grating diffraction–E-mode polarization and losses," *J. Opt. Soc. Am.* **73**, pp. 451–455, April 1983.

[90] M. G. Moharam, E. B. Grann, D. A.Pommet, and T. K. Gaylord, "Formulation for stable and efficient implementation of the rigorous coupled-wave analysis of binary gratings," *J. Opt. Soc. Am. A* **12**, pp. 1068–1076, May 1995.

[91] M. G. Moharam, D. A. Pommet, E. B. Grann, and T. K. Gaylord, "Stable implementation of the rigorous coupled-wave analysis for surface-relief gratings: Enhanced transmittance matrix approach," *J. Opt. Soc. Am. A* **12**, pp. 1077–1086, May 1995.

[92] X. Niu, *An Integrated System of Optical Metrology for Deep Sub-Micron Lithography.* PhD thesis, University of California, Berkeley, 1999.

[93] A. Yen, ed., *Optical Microlithography XV*, *Proc. SPIE* **4691**, 2002.

[94] Y. Vladimirsky, ed., *Emerging Lithographic Technologies II*, *Proc. SPIE* **3331**, 1998.

[95] Y. Vladimirsky, ed., *Emerging Lithographic Technologies III*, *Proc. SPIE* **3676**, 1999.

[96] E. A. Dobisz, ed., *Emerging Lithographic Technologies IV*, *Proc. SPIE* **3997**, 2000.

[97] R. L. Engelstad, ed., *Emerging Lithographic Technologies VI*, *Proc. SPIE* **4688**, 2002.

[98] E. A. Dobisz, ed., *Emerging Lithographic Technologies V*, *Proc. SPIE* **4343**, 2001.

[99] C. J. Progler, ed., *Optical Microlithography XIV*, *Proc. SPIE* **4346**, 2001.

[100] R. L. Engelstad, ed., *Emerging Lithographic Technologies VII*, *Proc. SPIE* **5037**, 2003.

[101] R. S. Mackay, ed., *Emerging Lithographic Technologies VIII*, *Proc. SPIE* **5374**, 2004.

Appendix A

Tcl Source Code for Grating Simulation with *gtk*

```
#!/Users/jason/bin/gtksh

# Tcl/Tk source for gtk simulation of 1:1 grating
#
# Jason Cain
# jcain@eecs.berkeley.edu

# Open data file with n and k data and read it in
set fileID [open Si_short.nk r]
set Si_nk {}
while {[gets $fileID line] >= 0} {
  lappend Si_nk [list [format "%3.12f" [lindex $line 0]] [format \
   "%3.12f" [lindex $line 1]] [format "%3.12f" [lindex $line 2]] ]
}
close $fileID

set fileID [open met-1k_jc.nk r]
set met1k_nk {}
while {[gets $fileID line] >= 0} {
  lappend met1k_nk [list [format "%3.12f" [lindex $line 0]] [format \
  "%3.12f" [lindex $line 1]] [format "%3.12f" [lindex $line 2]] ]
}
close $fileID
```

```
# middle CD [nm]
set CD 65.0

# Resist line height [nm]
set h 100.0

# sidewall angle [degrees]
set SWA 65.0

# convert sidewall angle to radians
set SWA [expr $SWA * acos(-1.0)/180.0]

# Radius of footing [nm]
set rf 20.0

# Radius of top rounding [nm]
set rr 10.0

# Number of layers for resist profile
set nL 10

#grating period, [nm]
set D 130

# number of orders
set orders 7

# incidence angle
set theta 70.0

# set up grating
Grating1D grating

# number of layers to use
grating setL [expr $nL + 1]

# grating period
grating setD $D

# set up the output file
set outputFile [open grating_out.txt w]
set str "%Lambda\tR\tRs\tRp\tTan(Psi)\tCos(Delta)"
puts $outputFile $str
```

```
# Define some mathematical functions
proc csc {x} {
   return [expr 1.0/sin($x)]
}

proc sec {x} {
   return [expr 1.0/cos($x)]
}

proc cot {x} {
   return [expr 1.0/tan($x)]
}

proc abs {x} {
   if {$x < 0} {
      return [expr -$x]
   } else {
      return $x
   }
}

# Calculate x-value of profile edge at base
set xb [expr -(1.0/4.0)*[csc $SWA]*[csc $SWA]*($CD+($-2.0*$rf)* \
   sin(2.0*$SWA)+2.0*$rf*[sec $SWA]*tan($SWA)+cos(2.0*$SWA)* \
   (-$CD+2.0*$rf*[sec $SWA]*tan($SWA)))]

# Calculate x-value where footing begins
set xf [expr -(1.0/2.0)*cos($SWA)*cos($SWA)*(($h-2.0*$rf)*([cot $SWA] \
   +tan($SWA))+$CD*[sec $SWA]*[sec $SWA]+2.0*[cot $SWA]*[cot $SWA]*$rf* \
   [sec $SWA]*tan($SWA))]

# Calculate y-value where footing begins
set yf [expr -sqrt($rf*$rf-($xf-$xb)*($xf-$xb))+ $rf]

# Calculate x-value of end of top rounding
set xt [expr (1.0/4.0)*[csc $SWA]*[csc $SWA]*(-$CD+($-2.0*$rr)* \
   sin(2.0*$SWA)+2.0*$rr*[sec $SWA]*tan($SWA)+cos(2.0*$SWA)*($CD+2.0* \
   $rr* [sec $SWA]*tan($SWA)))]

# Calculate x-value where top rounding begins
set xr [expr (1.0/2.0)*cos($SWA)*cos($SWA)*(($h-2.0*$rr)*([cot $SWA]+ \
   tan($SWA))-$CD*[sec $SWA]*[sec $SWA]+2.0*[cot $SWA]*[cot $SWA]*$rr* \
   [sec $SWA]*tan($SWA))]
```

```
# Calculate y-value where top rounding begins
set yr [expr sqrt($rr*$rr-($xr-$xt)*($xr-$xt))+ $h-$rr]

# Main loop to calculate diffraction response spectrum

set cnt 0
for {set val 240} {$val <= 760} {set val [expr $val + 10 ]} {
   set str "Simulating lambda = $val..."
   puts $str

   set n0 [list $val 1.0 0.0]
   set n1 [lindex $met1k_nk $cnt]
   set n2 [lindex $Si_nk $cnt]

   # Add air layer
   grating addLayer 0 $D -1 n0

   # Add MET-1K layer
   for {set i 0} {$i < $nL} {incr i} {
      set y [expr $i*($h/$nL)]
      if {$y <= $yf} {
         set x [expr sqrt($rf*$rf - ($y-$rf)*($y-$rf))+$xb]
         grating addLayer [expr $i+1] [expr 2.0*[abs $x]] [expr $h/$nL] n1
         continue
      }
      if {$y >= $yr} {
         set x [expr -sqrt($rr*$rr - ($y-$h+$rr)*($y-$h+$rr))+$xt]
         grating addLayer [expr $i+1] [expr 2.0*[abs $x]] [expr $h/$nL] n1
         continue
      }
      if {$y >= [expr $h/2.0]} {
         set x [expr $CD/2.0 - ($y-$h/2.0)/tan($SWA)]
         grating addLayer [expr $i+1] [expr 2.0*[abs $x]] [expr $h/$nL] n1
      } else {
         set x [expr $CD/2.0 + ($y-$h/2.0)/tan($SWA)]
         grating addLayer [expr $i+1] [expr 2.0*[abs $x]] [expr $h/$nL] n1
      }
   }

   # Add silicon layer
   grating addLayer [expr $nL+1]  $D -1 n2

   # incident angle for ellipsometry
```

```
    grating setTheta $theta

    set rtm [grating RTM1 $orders]
    set rte [grating RTE $orders]

    set v1 [lindex $rtm 0]
    set v2 [lindex $rtm 1]
    set v3 [lindex $rtm 2]
    set v4 [lindex $rte 0]
    set v5 [lindex $rte 1]
    set v6 [lindex $rte 2]
    set v7 [expr $v1/$v4]
    set tanpsi [expr sqrt($v7)]
    set mag [expr sqrt(pow([expr $v2*$v5 + $v3*$v6],2) + \
       pow([expr $v3*$v5-$v2*$v6],2))/[expr pow($v5,2)+pow($v6,2)]]
    set cosdel [expr ($v2*$v5 + $v3*$v6)/ \
       sqrt(pow([expr $v2*$v5 + $v3*$v6],2)+pow([expr $v3*$v5-$v2*$v6],2))]

    # incident angle for ellipsometry
    grating setTheta 0.0

    set rtm [grating RTM1 $orders]
    set rte [grating RTE $orders]

    set Rp [lindex $rtm 0]
    set Rs [lindex $rte 0]
    set R [expr ($Rp + $Rs)/2.0]

    set str "$val\t$R\t$Rs\t$Rp\t$tanpsi\t$cosdel"
    puts $outputFile $str
    incr cnt
}

close $outputFile
```

Appendix B

List of Symbols

$\Delta x(r_{pupil})$	Lateral pattern shift in aerial image, see equation (3.24)	
Δ	Relative phase difference between TE and TM modes, see equation (5.1)	
$\Delta\phi$	Optical path difference, see equation (3.24)	[waves]
$\delta_{nn'}$	Kronecker delta function, see equation (3.5)	
ϵ	Radius of central obscuration in an annular pupil, see equation (3.9)	
λ	Wavelength of light source, see equation (2.1)	[nm]
Ψ	Ratio of magnitudes for TM and TE modes, see equation (5.1)	
ρ	Normalized radius within the pupil, see equation (3.1)	
σ	Degree of partial coherence, see equation (2.3)	
σ_s	Standard deviation of surface roughness, see equation (3.19)	
σ_{PSF}	Standard deviation of Gaussian resist PSF, see equation (4.2)	
θ	Polar angle within the pupil, see equation (3.1)	[radians]
θ_i	Angle of incidence, see equation (3.19)	
a_j	Aberration coefficient of jth Zernike polynomial, see equation (3.1)	
d_o	Diameter of objective optic entrance pupil, see equation (2.3)	[m]
d_s	Diameter of source image in the entrance pupil, see equation (2.3)	[m]
DOF	Depth of focus, see equation (2.2)	[μm]
E	Aerial image electric field, see equation (3.23)	

I Aerial image intensity, see equation (3.23)

j Zernike polynomial ordering index, see equation (3.1)

k_1 Lithography process parameter, see equation (2.1)

k_2 Depth of focus process parameter, see equation (2.2)

L_{min} Minimum half-pitch, see equation (2.1) [nm]

NA Numerical aperture of optical system, see equation (2.1)

NA_c Numerical aperture of condenser optic, see equation (2.3)

NA_o Numerical aperture of projection optic, see equation (2.3)

P_0 Specular reflected power, see equation (3.19)

P_i Incident power, see equation (3.19)

P_s Scattered power, see equation (3.19)

P_{mask} Pattern pitch at the mask, see equation (3.24) [nm]

$PSF_{resist}(x)$ One-dimensional resist point spread function, see equation (4.2)

Q_n^m Factor of radial polynomial of Zernike term, see equation (3.7)

R Reflection coefficient, see equation (3.19)

$R_n^m(\rho)$ Radial polynomial component of Zernike terms, see equation (3.5)

r_p Complex reflection coefficient for TM polarization, see equation (5.1)

r_s Complex reflection coefficient for TE polarization, see equation (5.1)

r_{pupil} Radius within the pupil of an optical system, see equation (3.24)

TIS Total integrated scatter, see equation (3.19)

$W(\rho, \theta)$ Wavefront function for circular pupil, see equation (3.1) [nm] or [λ]

$W(\rho, \theta; \epsilon)$ Wavefront function for annular pupil, see equation (3.9) [nm] or [λ]

Z_j j^{th} Zernike polynomial, see equation (3.1)

FWHM Full width at half maximum, see equation (4.3)